Title

Zonal Flows in Planetary Fluid Layers

Author

Aggarwal, Ashna

Publication Date

2022

UNIVERSITY OF CALIFORNIA

Los Angeles

Zonal Flows in Planetary Fluid Layers

A dissertation submitted in partial satisfaction
of the requirements for the degree
Doctor of Philosophy in Geophysics and Space Physics

by

Ashna Aggarwal

2022

ABSTRACT OF THE DISSERTATION

Zonal Flows in Planetary Fluid Layers

by

Ashna Aggarwal
Doctor of Philosophy in Geophysics and Space Physics
University of California, Los Angeles, 2022
Professor Jonathan M. Aurnou, Chair

Zonal flows are some of the most ubiquitous and pronounced fluid structures observed in the solar system. They are found in Earth's atmospheres and oceans, likely Earth's liquid outer core, and on the surfaces of the gas giant planets and dwarf stars. They are responsible for mechanisms such as the transfer of heat and momentum in atmospheres, which can lead to complex weather systems on Earth and other planets. Though they are essential to the dynamics of geophysical and astrophysical bodies, their formation, evolution, and breakdown is not well understood. However, it is known that zonal flows in planetary and stellar fluid systems are controlled by the complex interplay of convection, rotation, and magnetic forces. For my dissertation, I have carried out two projects that contribute to our understanding of how zonal flows, and thus geophysical and astrophysical bodies, are influenced by these forces.

For the first project, in collaboration with my advisor Jonathan Aurnou and professor Susanne Horn from Coventry University, I developed and used a novel computational code to model the mechanism responsible for the damping of the large-scale, azimuthally directed "jets" observed at Jupiter's surface which is not well understood. Electromagnetic forces are thought to play a role as the planet's electrical conductivity increases radially with depth. In order to isolate the jet damping process, we carry out a suite of direct numerical simulations of quasi-two-dimensional, horizontally periodic Rayleigh-Bénard convection (RBC) with stress-free boundary conditions in the presence of an external, vertical magnetic field. Without a magnetic field, jets, punctuated by intermittent convective bursts, develop at Rayleigh (Ra, ratio of buoyancy to diffusion) numbers beyond 10^5. Five primary flow regimes are found by varying $10^3 \leq Ra \leq 10^{10}$ and the Chandrasekhar number (Ch, ratio of Lorentz to viscosity) $0 \leq Ch \leq 10^6$: (i) steady convection rolls, (ii) steady magneto-columns, (iii) unsteady to turbulent magneto-plumes, (iv) horizontally drifting magneto-plumes, and (v) jets with intermittent turbulent convective bursts. We parse the parameter space using transition laws derived from the interaction parameter (N, ratio of Lorentz to inertia). The transition to the regime dominated by jets has the most immediate applications to the magnetic damping of Jovian jet flows, where the separation between jets and a magnetically constrained system occurs at a jet-based interaction parameter value of $N_J \approx 1$. We conclude by approximating the value of the Jovian interaction parameter as a function of depth, and find that the jets may brake at approximately $6,000$ km below the surface, which is deeper than recent estimates from NASA's Juno mission. This implies that mechanisms in addition to electromagnetic forces are likely required to fully truncate the jets.

For the second project, in collaboration with Jonathan Aurnou and previous UCLA student Taylor Lonner, I developed the theoretical framework for and analyzed the data from a novel experimental device, which was built and run by Taylor. Through this project, we seek to increase our understanding of how turbulent fluid motions in Earth's liquid iron core sustain the geodynamo. The underlying flow, in which zonal jets may also play a key role, is influenced by planetary rotation, buoyancy and magnetic forces, and the geometry of the spherical shell. Recent numerical studies, which aim to characterize the dominant length and velocity scales in spherical rotating convection models, are limited by the long integration times required to access laboratory-scale turbulence. Furthermore, core-style turbulent convection is difficult to simulate with spherical shell experiments due to friction from solid container boundaries, and limitations, to date, on container size.

In this project, we take advantage of strong laboratory turbulence by utilizing a cylindrical laboratory device that incorporates both the effects of boundary curvature, quantified by a topographic β-effect, and a predominantly cylindrically-radial centrifugal forcing, a proxy for gravity, to model low-latitude core convection. The experiment is characterized by a paraboloidal free surface and features a cylindrically-radial temperature gradient to drive convection. This novel set-up approximates the topographic β profiles in a sphere, thus providing a meaningful proxy for low-latitude core convection. Three cases of rotating convection at 35, 50, and 60 RPM were run, with UDV velocity profiles, novel surface thermography, and basal thermometry for diagnostics. The combination of the topographic β-effect and convectively driven turbulence leads to the formation of coherent, alternating prograde-retrograde jets in all three experiments. The analysis in this thesis shows that the width of the jets closely follows a length scale known as the Rhines scale. The Rhines scale is expected when the topographic β-effect halts the transfer of energy from small to large scales that can occur in turbulent, rapidly rotating systems. Several other interesting flow features are noted here, including topographic and thermal Rossby waves and jet migration that closely match theoretical predictions. This device, with a paraboloidal free surface and laterally driven convection, can provide length and velocity scale estimates for the turbulent dynamics in low-latitude regions of Earth's outer core, and further elucidate the processes responsible for the geomagnetic field.

The dissertation of Ashna Aggarwal is approved.

Susanne Horn

Jonathan Lloyd Mitchell

Marcelo Chamecki

Carolina Lithgow-Bertelloni

Jonathan M. Aurnou, Committee Chair

University of California, Los Angeles

2022

To Ben, my love.

and—

To my Mom, my role model.

TABLE OF CONTENTS

LIST OF FIGURES

LIST OF TABLES

ACKNOWLEDGMENTS

My deepest gratitude goes to my advisor, Dr. Jonathan Aurnou, who has truly shaped me into a better scientist. Jon's feedback and mentorship over the years has encouraged, challenged, and humbled me. I have learned a variety of skills from working with Jon; ranging from improved analytical prowess to the importance of clear figures to the ability to translate complex scientific concepts to a general audience. He, for example, allowed me to lead the development of the numerical code written for the first project in this dissertation, and carry out much of the analysis for the experimental data in the second project of this dissertation. These experiences greatly improved my ability to model and analyze complex dynamical systems. I am also thankful to be his teaching assistant for the course "Introduction to Computing for Geoscientists" in 2019 and 2020, which improved my teaching and Python abilities. Broadly, I am grateful for his constant support and enthusiasm for science.

I would also like to thank Dr. Susanne Horn, a member of my thesis committee. Without Susanne, the first project in this dissertation would not have been possible. Susanne guided me through many steps along the way, from helping me write and compile my first Fortan code to pointing me to the literature that ultimately served as the theoretical framework for the study. I would also like to express my gratitude for Susanne's friendship and camaraderie throughout my time at UCLA.

My sincerest gratitude goes to Dr. Carolina Lithgow-Bertelloni, a member of my thesis committee. For several of my years at UCLA, our groups shared weekly research meetings which we called "Crust to Core." Through these meetings, I greatly extended my knowledge of physics related to Earth Science. I am also thankful for the opportunity to be her teaching assistant for the course "Introduction to Computing for Geoscientists" in 2021, through which I learned additional, useful Python techniques. Finally, I am grateful for the advice she has shared about navigating the many twists and turns of graduate school.

I am thankful for Dr. Marcelo Chamecki, a member of my thesis committee. I took

Marecelo's class "Numerical Methods in Geophysical Fluid Dynamics" in 2018. I applied the techniques I learned in his course directly to the code developed for the first project in this dissertation.

I would like to thank Dr. Jonathan Lloyd Mitchell, a member of my thesis committee. I took Jonathan's class "Oceans and Atmospheres" in 2018. In his class, we performed many hands on demonstrations that enhanced my understanding of geophysical flows. For example, we performed an experiment in which a rotating tank of water was left open to the air. We found that change in height of the free surface varied parabolically with radius. This experiment improved my understanding of the second project in this dissertation.

I would like to acknowledge Taylor Lonner, who developed and performed the experiments for the second project in this dissertation. We also wrote the first version of the paper, modified for Chapter 3 in this dissertation, together. This project would not have been possible without Taylor.

Thank you to all students and visitors of SPINlab with whom I intersected: Alex Grannan, Emily Hawkins, Yufan Xu, Jewel Abbate, Cy David, Norris Khoo, AJ Chlarson, Tobias Vogt, Robert Long, Jonathan Mound, and Sietze Oostveen. They have provided many useful discussions and an equal amount of enjoyable lunches.

Graduate school can be a challenging endeavor at times. I am beyond thankful for my 2016 cohort for their friendship as we overcame these hurdles together. In particular, I would express my gratitude to thank Heather Kirkpatrick, Ashley Schoenfeld, and Krista Sawchuk. Thank you also to my friends from William and Mary who continue to enrich my life: Daniel Duane, for helping me navigate the final steps of graduate school, Gabriel Morey, for the long phone calls and shared passion for public policy, Sarah Maddox, for companionship as we both go through STEM PhD programs, and Melissa Dullum, for always making me laugh.

I am also thankful for the support of my friends in the Los Angeles endurance community.

They have all been so patient as I expressed my frustrations and woes about graduate school on a number of long runs. I would especially like to express my gratitude for Leslie Cohen, Kristee Sherry, Deike Peters, Tracy Powell, Marty Ryan, Natalie Larson, Laura Osman, Maggie Shearer, Anton Saleh, Danae Dracht, Alexi Pappas, and Bill Sumner. I am also thankful to them for continuing to inspire me in sport.

Thank you to all members of the UCLA Science Policy Group, who passionately use their scientific skillset to inform public policy. Their guidance and support has been critical to my development as I shift towards this space. I would also like to thank my high school student from Minds Matter Los Angeles, Anisa Khair who has expanded my world view and taught me the importance of patience and dedication.

Most importantly, I am beyond grateful to my family. I would not have been able to complete this dissertation without their encouragement and belief. My dog, Finn, continues to ground me with his goofy smile, big ears, and loving eyes. Long hikes and walks with Finn have been the key to my sanity. I am so lucky to have Finn to lean on during my toughest days. Even though he is "just a dog," I hope that by writing these words, he will understand how much he means to me. I am also incredibly grateful for my mom, Anu Aggarwal. My mom has been the greatest role model that I could wish for. She received her graduate degree in computer science many years ago, and showed me that I was more than capable of succeeding in a STEM career. In addition, she has not only provided support during my time at UCLA, but wisdom and clarity. I am so fortunate to have her as a parent.

Finally, words cannot describe how grateful I am for my husband, Ben. Ben and I moved out to Los Angeles nearly six years ago to pursue doctoral degrees in our respective fields. He has been, and continues to be, my partner every step of the way. Thank you for your love, patience, and support. Thank you for marrying me in a courthouse. Thank you for being an incredible scientist. Thank you for sharing this crazy, wonderful life with me. Thank you, thank you, thank you.

VITA

2016	B.S., Physics (with Honors), The College of William and Mary.
2016	Minor, Mathematics, The College of William and Mary.
2016-2022	Graduate Student Researcher, University of California, Los Angeles.
2016-2922	Teaching Assistant, University of California, Los Angeles.
2018	M.S., Geophysics and Space Physics, University of California, Los Angeles.
2022	Analysis Associate, Rocky Mountain Institute.

PUBLICATIONS

Planetary Core-Style Rotating Convective Flows in Paraboloidal Laboratory Experiments. T. Lonner, **A. Aggarwal**, J. M. Aurnou, Journal of Geophysical Research: Planets. *In Review.* (2022).

Magnetic damping of convectively driven jet flows. **A. Aggarwal**, J. M. Aurnou, S. Horn. Physical Review E. *In Review.* (2022).

Experimental pub crawl from Rayleigh-Bénard to magnetostrophic convection. A. Grannan, J. Cheng, **A. Aggarwal**, E. Hawkins, S. Horn, J. Sanchez-Alvarez, J. M. Aurnou. Journal of Fluid Mechanics (Rapids). **939**, R1, (2022).

Prediction of Solar Eruptions Using Filament Metadata. **A. Aggarwal**, N. Schanche, K. Reeves, D. Kempton, and R. Angryk. Astrophysical Journal. **236**, 15 (2018).

A Comparison of Classifiers for Solar Energetic Events. G. Barnes, N. Schanche, K. D. Leka, **A. Aggarwal**, and K. Reeves. Proceedings of the IAU Symposium. **S325**, 201-204 (2016).

CHAPTER 1

Introduction to Planetary Scale Fluid Dynamics

Geophysical and astrophysical fluid layers are ubiquitous in nature. Examples include Earth's atmospheres, oceans, and liquid metal outer core where the planet's magnetic field is ultimately generated and sustained. In addition, all planets in the Solar System are host to at least one large scale fluid layer. And, as satellite missions explore sub-planetary scale bodies such as Ganymede and Enceladus, they are finding fluids responsible for phenomena such as magnetic field generation and polar plumes (Kivelson et al., 1996; Flannery et al., 2006). Though each system is unique, there are common factors among them. The first is high inertia, characterized by chaotic motions over a broad range of length and time scales. The second is strong background rotation, which has a stabilizing effect on the flow. The combination of these two phenomena, turbulence and rotation, can lead to a broad array of flow morphologies including domain scale structures. These structures in turn play a crucial role in planetary scale fluid dynamics (ex., weather patterns and magnetic field generation).

Coherent zonal flows are large-scale structures directed in the azimuthal direction (also known as jets). They are pervasive in Earth and Jovian atmospheres (Schneider, 2006; Vasavada and Showman, 2005), and Earth's oceans with time-averaging (Maximenko et al., 2005). For the gas giants, Jupiter and Saturn, these hydrodynamic, azimuthally-directed zonal winds are amongst their most dominant surface features. Fig. 1.1(a) shows an image of the Jupiter's surface, overlaid with the zonal profile with latitude. These winds are strongest near the equator and alternate in direction with varying latitude. Recent measurements of Jupiter's gravity field from Juno may hold information of the zonal flow structure with depth. Inverting the gravity harmonics to make deductions about interior flow morphology remains a theoretical challenge (Kong et al., 2017), but this data has thus far has been used to infer that the zonal winds of Jupiter extend from the weather layer down at least 3,000 km deep into the hydrogen-helium molecular atmosphere (Kaspi et al., 2018). As electrical conductivity increases radially with depth, the fast-moving jet flow transitions to a slow moving dynamo flow, which generates the anomalous magnetic field structure seen in Fig. 1.1(b). It is the increasing importance of magnetohydrodynamic processes with depth that likely may the hydrodynamic zonal winds observed at the surface.

In Chapter 2, we characterize the fundamental process of magnetic damping on large-scale zonal flows (jets) using a reduced, two-dimensional numerical model of convection with an imposed magnetic field. We use this computational model, for which I was the lead developer, to further our understanding of magnetohydrodynamic (MHD) flows, including their ability to suppress gradients in the flow velocity parallel to the direction of the applied field. We also find the magnetic field strength relative to inertia required to ultimately damp jets driven by buoyancy in a two-dimensional system. By using this simplified model, approximate predictions for the radial location at which the truncation occurs in Jovian systems can be made, and compared to those truncation depths found by the recent Juno mission. We discuss the implications of our results on learning which processes ultimately brake the Jovian jets.

In Chapter 3, we investigate the generation of planetary magnetic fields, which are intrinsically tied to conducting fluid motions and reveal global-scale features on all planets with an active dynamo (Bloxham and Gubbins, 1985). For Earth, where the magnetic field data is of the highest resolution to date, a number of hypotheses have been proposed to explain the planet's domain-scale, dipolar magnetic field structure. This dipolar structure can be observed in Fig. 1.1(c), which shows Earth's radial magnetic field at the core-mantle boundary. The list includes the dominance of low wave number modes in core flows, or the transfer of energy from small to large scales that can occur in constrained, turbulent systems

(Aurnou et al., 2015). At present, both laboratory experiments and numerical simulations are unable to access the vast range of length and time scales required to characterize Earth's turbulent, dynamo-generating region. Numerical simulations of the geodynamo are predominately driven by axially-aligned convective columns, a laminar solution of hydrodynamic rotating convection. Fig. 1.1(d) shows a schematic of these convective columns. Any large-scale structures that do indeed develop from turbulent cascades are found exclusively in plane-layer models of rotating convection with periodic domains, which neglect the effects boundary curvature (i.e., change in axial fluid layer height with radius) Guervilly and Hughes (2017); Julien et al. (2018a).

Thus, in Chapter 3, we seek to explain Earth's magnetic field observations using a novel laboratory-numerical set up that includes both strong buoyancy forces to drive inertial flows, and strong boundary curvature. Analysis of the results of this laboratory device reveal coherent alternating prograde-retrograde jets, and we are able to show that their length scale is consistent with a key quantity known as the Rhines scale. Our data analysis also reveals several other interesting features, including topographic Rossby waves that likely excite the jets, and the radial migration of some jet structures. Finally, we lay the theoretical groundwork for future paraboloidal quasi-geostrophic computational models. Our results may indicate the existence of zonal flows in the outer core, which have the ability to convert components of poloidal fields into toroidal fields and can play an important part in the dynamo processes,

In the last Chapter, I summarize the work presented here and discuss the broad implications for planetary scale fluid systems. In particular, I discuss how this work furthers our understanding of the fundamental processes that influence the formation, evolution, and braking of planetary scale zonal flows, which in turn play a key role in geophysical and astrophysical fluid systems.

My contributions to each chapter of this thesis are: I wrote the code used for a majority of the numerical simulations in Chapter 2. For the remaining cases, I modified an open-source code and ran the simulations on my own. All of the analysis and a majority of the theoretical work for Chapter 2 are also my own. This chapter is modified from a paper which has undergone one round of revisions in *Physical Review E*, for which I am the first author. The experimental data used in Chapter 3 was solely collected by co- first author Taylor Lonner. I contributed to a majority of the figures and analysis, and led the theoretical and numerical portion of the study. This chapter is modified from a paper submitted to the *Journal of Geophysical Research: Planets* which I am co-first author.

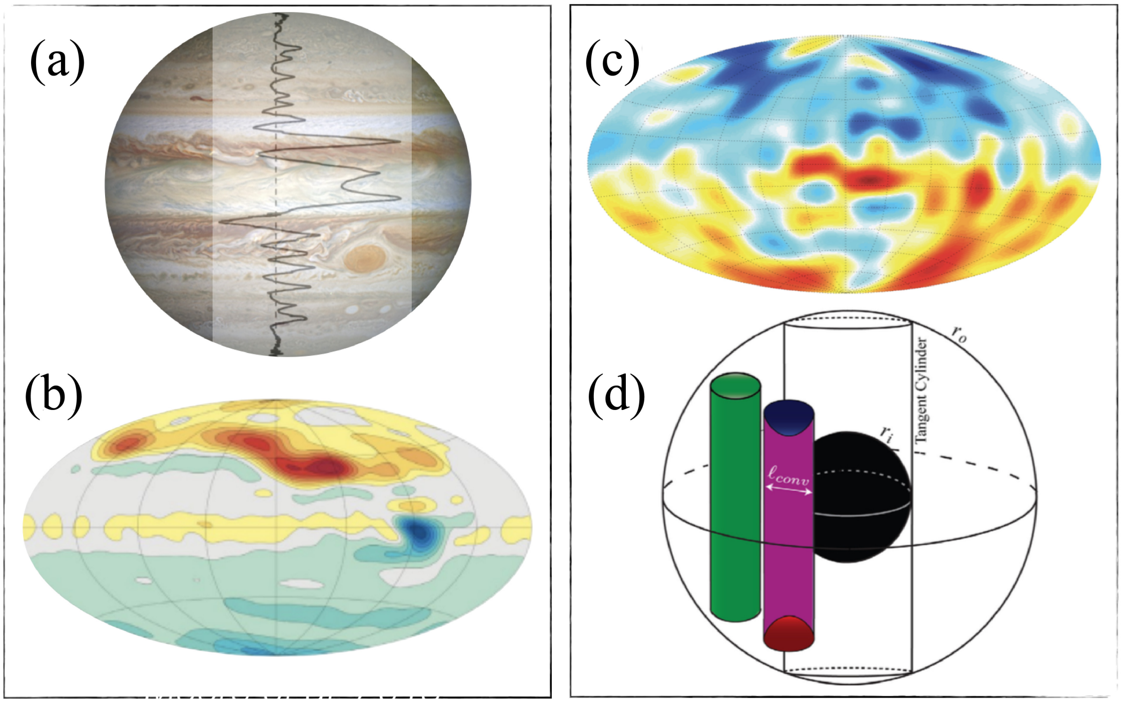

Figure 1.1: (a) Jupiter (image credit: NASA) and superimposed zonal flow profile varying with latitude Porco et al. (0003) (b) Jupiter's radial magnetic field, B_r, at $\approx$ 1 bar. Blue (red) signifies field lines radially inwards (outwards) ranging from about -5 to 5 microtesla (figure credit: Moore et al. (2018)). (c) Earth's radial magnetic field, B_r, at the core-mantle boundary (CMB). Blue (red) signifies field lines radially inwards (outwards) ranging from about -1000 to 1000 microtesla, (image credit: H. Cao). (d) Schematic of axially-aligned convective columns found in laminar solutions of rotating convection (figure credit: Aurnou et al. (2015)).

CHAPTER 2

Magnetic Braking of Convectively Driven Flows

2.1 Introduction

Turbulent flows in planetary and stellar interiors, often driven by convection, are controlled by the complex interplay of stratification, rotation, and magnetic forces. One canonical setup used to understand the fundamental processes behind such flows is Rayleigh-Bénard convection (RBC), in which a fluid is heated from below and cooled from above. RBC studies also often include additional forces such as rotation or an applied magnetic field to gain further insight into geophysical and astrophysical flows (Aurnou and Olson, 2001; King et al., 2009; Weiss and Proctor, 2014; Ecke and Niemela, 2014; Garaud et al., 2015; Guervilly and Hughes, 2017; Horn and Aurnou, 2018; Cheng et al., 2020).

Zonal winds, or azimuthally directed large-scale flows (also called "jets") are one type of flow structure often observed in planetary and stellar systems, such as at the surfaces of Jupiter and Saturn (Ingersoll, 1990; Atkinson et al., 1996; Porco et al., 0003; Vasavada and Showman, 2005). Fig. 2.1 shows an image of Jupiter's southern hemisphere from NASA in which one can observe the banded flow structure. Fig. 2.2(a) also shows in image of Jupiter, but with the zonal wind profile overlaid on the image in a solid black line, which demonstrates the existence of the alternating jets.

On Jupiter and Saturn the electrical conductivity increases as a function of spherical radius as the outer hydrodynamic molecular envelope transitions to a liquid metal (Gómez-Pérez et al., 2010; Heimpel and Gómez Pérez, 2011; French et al., 2012; Duarte et al., 2013; Cao

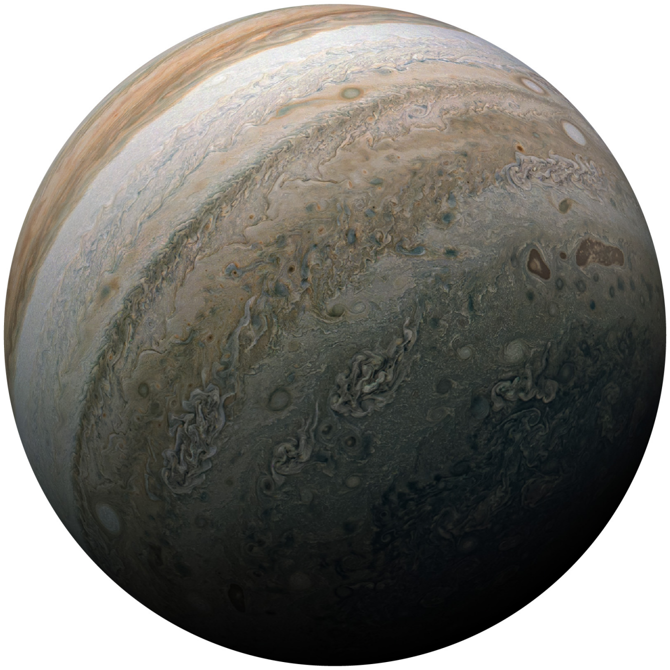

Figure 2.1: Figure adapted from NASA. Image of Jupiter's southern hemisphere taken on Feb. 17, 2020 in which the alternating bands of prograde and retrograde azimuthally directed flow ("jets") are visible.

and Stevenson, 2017). Fig. 2.2(b) gives the electrical conductivity profile as a function of planetary radius, where the sharp increase in electrical conductivity is highlighted in yellow. It is this increase in electrical conductivity, and thus electromagnetic effects, that may act as a resistive brake on the azimuthally-directed zonal flows through a mechanism known as "magnetic braking." Fig. 2.2(c) gives a schematic of the three layers of Jupiter that correspond to this electrical conductivity profile. The hydrodynamic jets (red/blue) are likely damped in the transition layer (yellow) outside of the liquid metal region (dark gray). Furthermore, the fundamental question of electromagnetic impact on large-scale flows is relevant to a variety of other systems, including the solar tachocline (Tobias et al., 2007, 2011; Constantinou and Parker, 2018) and plasmas in tokamaks (Wagner, 2007; Wesson, 2011).

Magnetic braking is a magnetohydrodynamic (MHD) phenomenon in which a strong magnetic field suppresses motions in a conducting fluid (Davidson, 2001). In the braking process, motion across magnetic field lines induces electric current, which gives rise to Joule dissipation. In turn, Joule dissipation subtracts from the kinetic energy present in the system, thus usually damping the flow speed, though the induction of magnetic field can complicate the damping effect (Pothérat and Klein, 2017). Zonal flow in the conducting regions of Jupiter and Saturn could also induce current, leading to Joule dissipation and a decrease in total energy available to the zonal winds (Christensen et al., 1999; Busse, 2002; Wicht, 2002; Schneider and Liu, 2009; Kirk and Stevenson, 1987). Thus, constraints on the zonal wind depth have been made (Liu et al., 2008), but are based on a specific and unconfirmed set of magnetic field and flow configurations (Glatzmaier, 2008).

Spherical shell hydrodynamic models of deep convection that reproduce many of the key jet characteristics have been carried out (Heimpel and Aurnou, 2007; Gastine et al., 2012). However, the geometry of each model is truncated at the bottom boundary with a free-slip condition. This serves as a proxy for MHD drag, but does not apply friction on the flow as the electromagnetic effects should. Idealized models that include MHD drag can help quantify the interplay between magnetic forces and jets, which can elucidate the jet-truncation mechanism on planets, such as Jupiter.

We leverage the work of (Goluskin et al., 2014), where it was shown that two-dimensional, horizontally periodic Rayleigh-Bénard convection (RBC) with free-slip boundary conditions can lead to the development of zonal flows, in which the horizontal motion is stronger than the vertical motion by several orders of magnitude. Similar two-dimensional simulations have been carried out by (Aubert et al., 2003; Calkins et al., 2012b; Gastine, 2019) in rotating annuli or by (Scott and Dritschel, 2012a) and (Wang et al., 2020) in a Cartesian domain, producing zonal flows similar to the ones found here. Three-dimensional, rapidly rotating convection simulations in periodic boxes resulting in alternating, unidirectional jets have also been conducted (Favier et al., 2014; Julien et al., 2018b), as well as rotating spherical shell

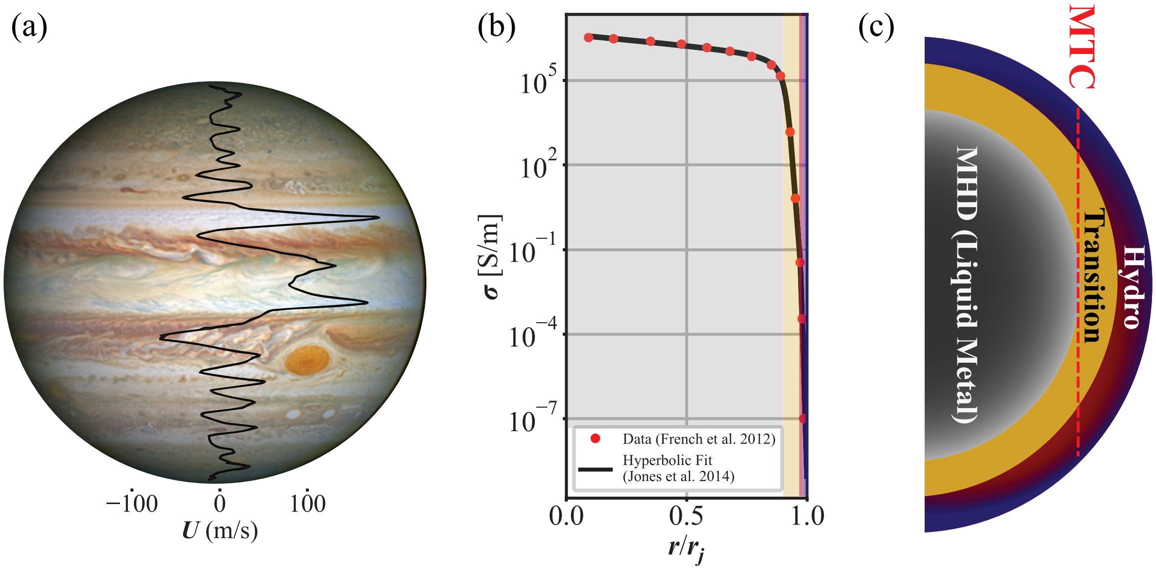

Figure 2.2: (a) The zonal wind profile of Jupiter with data from (Tollefson et al., 2017), superimposed on a full disk image of the planet taken by the Hubble Wide Field Camera. Figure adapted from (Kaspi et al., 2020). (b) Electrical conductivity, σ, for the interior of Jupiter in S/m, where $r_j = 6.9894 \times 10^7$m denotes the mean radius of Jupiter. The red points give the data from (French et al., 2012), and the black line shows the hyperbolic fit to the data with the function and fit coefficients following (Jones, 2014) and (Cao and Stevenson, 2017). The light red-blue shaded region corresponds to the hydrodynamic region in which $\sigma \approx 10^{-7}$ is negligible. The yellow shaded region, relevant to the model discussed in this paper, gives the transition region, where the electrical conductivity of the fluid increases sharply and MHD processes may influence the jets. The gray shaded region is then where $\sigma > 10^3$ and the fluid is fully metallic. (c) Schematic showing the three layers (hydrodynamic, transition, and metallic) mirroring the electrical conductivity profile in (b). The red dashed line denotes the radial location of the cylindrical "magnetic tangent cylinder (MTC)" (Heimpel and Gómez Pérez, 2011; Dietrich and Jones, 2018) which separates the inner magnetic shell from the outer hydrodynamic shell.

models with convective bursts (Busse, 1976; Heimpel and Aurnou, 2012).

Furthermore, rotating convection models have been studied extensively to not only elucidate the process behind planetary zonal flows (Busse, 1994; Christensen, 2001; Schneider and Liu, 2009; Showman et al., 2011), but also how planetary magnetic fields are generated and sustained (Simitev and Busse, 2005; Jones and Roberts, 2000; Aubert et al., 2008; Soderlund et al., 2013; Calkins et al., 2015). To isolate the MHD braking effects, we consider non-rotating RBC and apply a magnetic field perpendicular to the horizontally directed zonal flows. Fig. 2.3 shows the set up considered in this study for a case with zonal flows in the $\hat{\boldsymbol{x}}$-direction and the magnetic field in the $\hat{\boldsymbol{y}}$-direction. The purpose of this simplified Cartesian model is to investigate the fundamental magnetic damping mechanism in a system where jets are generated self consistently.

The rest of this chapter is organized as follows: Sec. 2.2 gives the governing equations for a 3D MHD rotating system such as Jupiter, and demonstrates how our quasi 2D systeml may be used to model this complex physical system. The governing equations and the numerical methods are given in Sec. 2.3. Sec. 2.4 gives a theoretical framework to separate the regimes based on the properties of the Lorentz force and the interaction parameter. In Sec. 2.5, we use flow properties such as length scale, momentum transport, and time-dependence to distinguish between the differing flow regimes, and in Sec. 2.5.2 we derive interaction transition laws based on length and velocity data to separate these regimes. We conclude in Sec. 2.6, and discuss the implications of our results for the depth of zonal winds on Jupiter. Sec. 2.7 gives the code development process, including discretization methods and steps taken to validate the solver. App. E gives the main integration routine developed in Fortran for the numerical simulations.

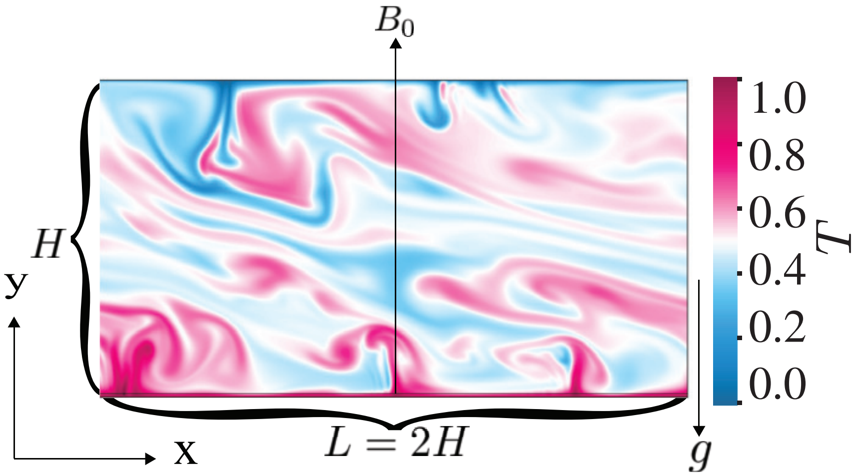

Figure 2.3: Instantaneous temperature field for a case with strong zonal jets ($Ra = 10^8, Ch = 10^2, Pr = 1, \Gamma = L/H = 2$, see Sec. 2.3.3 for parameter definitions). The domain is periodic in the $\hat{\boldsymbol{x}}$-direction, and has fixed temperature and stress-free vertical boundary conditions. Gravity points downwards in the negative $\hat{\boldsymbol{y}}$-direction, and a magnetic field is imposed in positive $\hat{\boldsymbol{y}}$-direction, such that $\boldsymbol{B} = B_0\hat{\boldsymbol{y}}$.

2.2 Reducing the Jovian Equations

The dynamics of Jupiter and Saturn are complex for a number of reasons, including the 3D spherical geometry, the compressible nature of the flow as density increases with radial depth, the electrical conductivity behaviour that also increases with radial depth, limited knowledge of the internal heat flow, and low viscosity values. These physical complexities present considerable challenges for numerical simulations, and simplifications are necessary when modeling the gas giants such as excessive viscosity values, axisymmetry, or the Boussinesq approximation (Christensen et al., 2020).

In our model we particularly leverage the leading order balance between rotation and pressure, which yields a flow approximately aligned with the rotation axis, allowing us to reduce the coordinate system from 3D to quasi-2D. Similar assumptions have been made across the literature when studying the Jovian planets, especially when considering the zonal flow profile with depth (Kaspi et al., 2018, 2020). In the following, we step through the governing equations for a 3D, rotating, MHD system and show how a leading order balance between rotation and pressure permits us to use a quasi-2D system to model Jovian jet dynamics.

Consider the rotating, MHD Navier-Stokes and continuity equations given by,

$$\rho\Big(\frac{\partial \boldsymbol{u}}{\partial t} + (\boldsymbol{u} \cdot \boldsymbol{\nabla})\boldsymbol{u}\Big) + 2\rho(\boldsymbol{\Omega} \times \boldsymbol{u}) = -\boldsymbol{\nabla} P + \boldsymbol{F_\nu} + \rho\boldsymbol{g} + (\boldsymbol{j} \times \boldsymbol{B}), \tag{2.1}$$

$$\frac{\partial \rho}{\partial t} = -\boldsymbol{\nabla} \cdot (\rho\boldsymbol{u}). \tag{2.2}$$

where $\boldsymbol{u}$ is the fluid velocity, P is the pressure, ρ is the fluid density, $\boldsymbol{\Omega} = \Omega\hat{\boldsymbol{z}}$ where Ω is the planetary rotation rate, and $\hat{\boldsymbol{z}}$ is in the direction of the planetary rotation axis and can be expressed in spherical coordinates as $\hat{\boldsymbol{z}} = cos(\theta) \cdot \hat{\boldsymbol{r}} - sin(\theta) \cdot \hat{\boldsymbol{\theta}}$. In addition, $\boldsymbol{j}$ is the electrical current density, $\boldsymbol{B}$ is the magnetic field, $\boldsymbol{g} = g\hat{\boldsymbol{r}}$ is gravitational acceleration, and κ is the thermal diffusivity. The centrifugal buoyancy term is neglected for simplicity.

Furthermore, $\boldsymbol{F_\nu}$ is the viscous force which includes the viscous stress tensor and can be written as,

$$F_{\nu,i} = \partial_j[\mu(\partial_j u_i + \partial_i u_j - \frac{2}{3}\delta_{ij}\boldsymbol{\nabla} \cdot \boldsymbol{u})] \tag{2.3}$$

where μ is the dynamic viscosity.

In gas giants, the density varies significantly in radius by several orders of magnitude, with the outer 10% in radius spanning about eight density scale heights (Stanley and Glatzmaier, 2010). Fig. 2.4(a) gives the approximate density variation with radial position for Jupiter, where the red points give the data from (French et al., 2012), and the blue lines shows the rational polynomial fit on the data with the function and fit coefficients following (Jones, 2014). Fig. 2.4(b) shows the density scale height $H_\rho = |\frac{\rho}{d\rho/dr}|$ with radial position. The scale height is the lowest near the surface where the most significant density variations occur.

Gastine and Wicht (2012) used convection models that include density stratification to show that jet characteristics to not change significantly when applying the Boussinesq approximation and assuming a constant background density. In addition, (Stanley and Glatzmaier, 2010) note that the Boussinesq approximation can be applied when the density scale height is much larger than the depth of the convective zone being considered. In our system, we use a quasi-2D Cartesian box to model a local slice of the Jovian atmosphere parallel to the equatorial plane relevant to the depths at which increased magnetic forces are thought to play a role in jet damping, or between 3000 to 1000km below the surface (approximately 0.95 to $0.985r_j$). The inset of Fig. 2.4 shows the variation in density over this approximate radial scale of 0.95 to $0.985r_j$. The density increases by about three-fold in this region. Future versions of this model should include density variations to accurately model the magnetic jet damping mechanism. However for simplicity, we begin with the most basic approximation, the Boussinesq approximation, and consider an average density ρ_0 around the local depth of our model effectively omitting fluid compressibility effects.

The Boussinesq approximation states that density variations will be neglected in all terms except for the buoyancy term. For the treatment of density variations in the buoyancy term, a Taylor expansion for the density around a reference temperature $T = T_0$ is used, which leads to,

$$\rho = \rho_0 + \frac{\partial \rho}{\partial T}\Big|_{T=T_0}(T - T_0) + \mathcal{O}(T - T_0)^2 \tag{2.4}$$

where α is the coefficient of isobaric thermal expansion, and is given by,

$$\alpha = -\frac{1}{\rho}\frac{\partial \rho}{\partial T}. \tag{2.5}$$

Substituting the definition of the thermal expansion coefficient α (2.6) into 2.4 and dropping higher order terms gives,

$$\rho = \rho_0(1 - \alpha(T - T_0)). \tag{2.6}$$

Next, we define the static $\boldsymbol{u} = 0$ background Navier-Stokes equation,

$$0 = -\boldsymbol{\nabla} P + \rho g \hat{\boldsymbol{r}} \tag{2.7}$$

and separate the pressure P into its background P_0 and dynamic p components, $P = P_0(r) +$

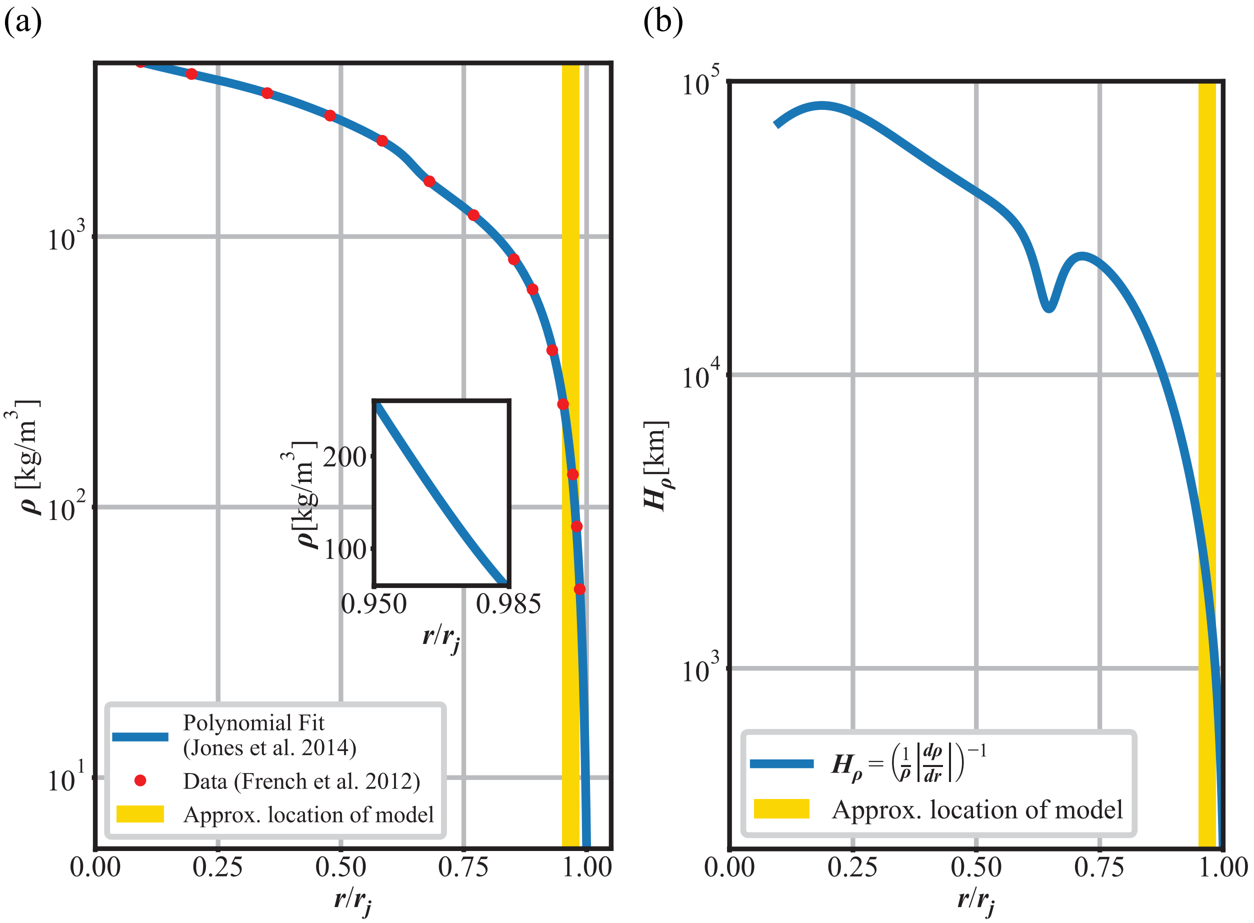

Figure 2.4: (a) Density for the interior of Jupiter in kg/m^3, where $r_j = 6.9894 \times 10^7$m denotes the mean radius of Jupiter. The red points give the data from (French et al., 2012), and the blue lines shows the rational polynomial fit on the data with the function and fit coefficients following (Jones, 2014). The thin yellow line shows the approximate location of the model in the region where increased magnetic forces could brake the jets, between 0.95 and $0.985r_j$. The inset shows the density variation over this narrow region. (b) Associated density scale height $H_\rho = |\frac{\rho}{d\rho/dr}|$, given in km, for the interior of Jupiter.

$p(\theta,\phi,t)$. Hydrostatic balance then yields,

$$\frac{dP_0}{dr} = -\boldsymbol{\nabla}\Phi \tag{2.8}$$

where $\Phi = \rho g r$ is the gravitational potential. Then, assuming a constant dynamic viscosity η and incompressible fluid, the rotating, MHD Navier-Stokes equation can be expressed as,

$$\rho_0\Big(\frac{\partial \boldsymbol{u}}{\partial t}+(\boldsymbol{u}\cdot\boldsymbol{\nabla})\boldsymbol{u}\Big)+2\rho_0(\boldsymbol{\Omega}\times\boldsymbol{u}) = (-\boldsymbol{\nabla}P_0-\boldsymbol{\nabla}p)+\rho_0 g\hat{\boldsymbol{r}}+\rho_0\alpha(T-T_0)g\hat{\boldsymbol{r}}+\nu\ \rho_0\boldsymbol{\nabla}^2\boldsymbol{u}+(\boldsymbol{j}\times\boldsymbol{B}), \tag{2.9}$$

where ν is the kinematic viscosity. We can use hydrostatic balance to simplify 2.9 and divide by ρ_0 leading to

$$\frac{\partial \boldsymbol{u}}{\partial t}+(\boldsymbol{u}\cdot\boldsymbol{\nabla})\boldsymbol{u}+2(\boldsymbol{\Omega}\times\boldsymbol{u}) = -\frac{1}{\rho_0}\boldsymbol{\nabla}p+\alpha(T-T_0)g\hat{\boldsymbol{r}}+\nu\boldsymbol{\nabla}^2\boldsymbol{u}+\frac{1}{\rho_0}(\boldsymbol{j}\times\boldsymbol{B}). \tag{2.10}$$

In the outer molecular envelope to metallic regions of the Jovian planets, a leading order balance between the Coriolis force and pressure gradients exists, which is known as geostrophic balance. We can justify this statement by nondimensionalizing. Eq. 2.10 and calculating the approximate strength of each term. To nondimensionalize Eq. 2.10, we choose a characteristic length scale $\mathcal{L}$, velocity scale U, time scale $\frac{\mathcal{L}}{U}$, planetary rotation rate Ω, magnetic field strength B_0, and pressure U^2, yielding,

$$\frac{\partial \boldsymbol{u}}{\partial t}+(\boldsymbol{u}\cdot\boldsymbol{\nabla})\boldsymbol{u}+\frac{1}{Ro}(\boldsymbol{\Omega}\times\boldsymbol{u}) = -\frac{1}{\rho_0}\boldsymbol{\nabla}p+\frac{Ra}{Re\ Pe}T\hat{\boldsymbol{r}}+\frac{1}{Re}\boldsymbol{\nabla}^2\boldsymbol{u}+\frac{Ch}{Re}(\boldsymbol{j}\times\boldsymbol{B}), \tag{2.11}$$

where, defining the Reynolds number (ratio of inertia to viscous diffusion, Re),

$$Re = \frac{U\mathcal{L}}{\nu}, \tag{2.12}$$

the Peclet number (ratio of inertia to thermal diffusion, Pe),

$$Pe = \frac{U\mathcal{L}}{\kappa}, \tag{2.13}$$

the Rossby number (ratio of inertia to Coriolis, Ro),

$$Ro = \frac{U}{2\Omega\mathcal{L}}, \tag{2.14}$$

and the Chandrasekhar number (ratio of Lorentz to viscous diffusion, Ch),

$$Ch = \frac{\sigma B_0^2 \mathcal{L}}{\rho_0 \nu}. \tag{2.15}$$

Estimating Re for the jets with a typical jet velocity of $U = 50$ m/s, a large-scale jet width of $\mathcal{L} = 10^4$km, and a kinematic viscosity of $\nu = 10^{-6}$m^2/s, yields $Re \approx 10^{14}$. Thus, the viscous term in 2.11 can be neglected. For the buoyancy term, (Heimpel and Aurnou, 2007) approximate $Ra \approx 10^{25}$ and $Pr = 0.10$, yielding a thermal diffusivity of $\kappa = 10^{-5}$m^2/s, resulting in $Pe \approx 10^{13}$. The estimates then give a number $\approx 10^{-2}$ in front of the buoyancy term, allowing us to not consider it as leading order. The value of the Lorentz term can be roughly approximated at the top of the semi-conducting region, at about $r = 0.95R_j$, where R_j is Jupiter's radius. Using an electrical conductivity value of $\sigma = 10^{-3}$S/m (French et al., 2012), a magnetic field strength of $B_0 = 2$mT (Moore et al., 2018), a jet width $\mathcal{L} = 10^4$km, a density of 10^3kg/m^3, and a kinetmatic viscosity of $\nu = 10^{-6}$m^2/s, gives $Ch \approx 10^8$. The approximate Ch is several orders of magnitude less than Re, allowing us to neglect the Lorentz term for the current discussion. However, we note that its role in the magnetic braking process will grow with depth, as the electrical conductivity and magnetic field values increase, and the inertia of the zonal winds decrease.

Similarly, the Ro for the jets can be approximated by using a typical jet velocity of $U = 50$ m/s, a jet width $\mathcal{L} = 10^4$km, and Jupiter's rotation rate $\Omega = 1.74 \times 10^{-4}$ 1/s, giving $Ro \approx 0.01$. Thus, the high-latitude jets are characterized by low Rossby numbers, leaving the advection terms in Eq. 2.11 negligible. A leading order balance between the Coriolis force and pressure gradients remains, which is known as geostrophic balance. The governing momentum equation for a fluid in geostrophic balance is then,

$$2(\boldsymbol{\Omega} \times \boldsymbol{u}) = -\frac{1}{\rho_0}\boldsymbol{\nabla} p \tag{2.16}$$

Taking the curl of 2.16 we find,

$$(\boldsymbol{\Omega} \cdot \boldsymbol{\nabla})\boldsymbol{u} = 0 \tag{2.17}$$

which is known as the Taylor-Proudman theorem. Thus, the high-latitude jets for which Coriolis nearly balances pressure gradients, or quasi-geostrophic (QG), then may extend into the molecular interior with little variation in zonal flow velocity, which is perpendicular to the rotation axis, in the axial $\hat{\boldsymbol{z}}$-direction. In addition, after invoking Taylor-Proudman theorem, we now use the cylindrical $\hat{\boldsymbol{s}}$-direction rather than spherical radial direction. Therefore, the zonal flow will predominantly contain shears in the cylindrical radial direction. Though variations in the background density can create changes in u_z along the axis of rotation, we choose to model a slice of the Jovian atmosphere parallel to the equatorial plane using a 2D Cartesian domain, allowing us to consider the background density constant over a local radial depth (see yellow box, Fig. 2.4). Thus, we simplify the geometry of the system immensely by mapping the cylindrical $\hat{\boldsymbol{s}}$-direction to a Cartesian $\hat{\boldsymbol{y}}$-direction, and the cylindrical $\hat{\boldsymbol{\theta}}$-direction to a Cartesian $\hat{\boldsymbol{x}}$-direction. In order to isolate the jet damping mechanism, the Lorentz force is included in the $\hat{\boldsymbol{y}}$-direction to brake the $\hat{\boldsymbol{x}}$-directed jets. The Lorentz force is parallel to the temperature gradient in our system, which is used to drive the flows.

2.3 Governing Equations and Numerical Methods

In this section, we present the framework for understanding MHD flows under the presence of a strong, uniform magnetic field, before introducing the governing equations specific to the set up used here. Configurations with a strong mean magnetic field have been the focus of a number of studies (Nakagawa, 1955; Sommeria and Moreau, 1982; Cioni et al., 2000; Pothérat et al., 2000; Aurnou and Olson, 2001; Chakraborty, 2008; Yan et al., 2019; Vogt et al., 2021; Zikanov et al., 2021; Xu et al., 2022). A simplification often made is to apply the quasistatic approximation (QSA), which states that the induced magnetic field, $\boldsymbol{b}$, is negligible, and $\partial \boldsymbol{b}/\partial t \approx 0$ (Roberts, 1967; Davidson, 2001; Knaepen et al., 2004; Knaepen and Moreau, 2008). QSA is typically invoked when the magnetic Reynolds number

$$Rm = \frac{U\mathcal{L}}{\eta}, \tag{2.18}$$

is significantly lower than 1, where U is a characteristic velocity scale, $\mathcal{L}$ is a characteristic length scale, and η the magnetic diffusivity. To demonstrate the effects of QSA, we can turn to the magnetic induction equation

$$\frac{\partial \boldsymbol{B}}{\partial t} + (\boldsymbol{u} \cdot \boldsymbol{\nabla})\boldsymbol{B} = \boldsymbol{B} \cdot \boldsymbol{\nabla} \boldsymbol{u} + \eta \nabla^2 \boldsymbol{B}, \tag{2.19}$$

which is coupled to the Navier-Stokes equation

$$\frac{\partial \boldsymbol{u}}{\partial t} + (\boldsymbol{u} \cdot \boldsymbol{\nabla})\boldsymbol{u} = -\frac{1}{\rho}\boldsymbol{\nabla} p + \rho \boldsymbol{g} + \nu \boldsymbol{\nabla}^2 \boldsymbol{u} + \frac{1}{\rho}(\boldsymbol{j} \times \boldsymbol{B}), \tag{2.20}$$

where $\boldsymbol{B}$ is the magnetic field, $\boldsymbol{u}$ is the fluid velocity, ρ is the density, $\boldsymbol{g}$ is the gravitational acceleration vector, ν is the viscosity, and $\boldsymbol{j}$ is the current density. The magnetic field can be written in terms of the applied and induced components

$$\boldsymbol{B} = \boldsymbol{B_0} + \boldsymbol{b}, \tag{2.21}$$

where $\boldsymbol{B_0}$ is the applied field and $\boldsymbol{b}$ is the induced field. Eq. 2.19 can be reduced by requiring that the applied field is uniform and stationary and that $Rm \ll 1$. Adopting the characteristic scales $\boldsymbol{b} \sim b$, $\boldsymbol{u} \sim U$, and $\boldsymbol{\nabla} \sim 1/\mathcal{L}$, and taking the ratio of the nonlinear terms to the diffusion term in Eq. 2.19 gives

$$\frac{(Ub/\mathcal{L})}{(\eta b/\mathcal{L}^2)} = \frac{U\mathcal{L}}{\eta} = Rm. \tag{2.22}$$

Because we assume $Rm \ll 1$, Eq. 2.19 becomes

$$\frac{\partial \boldsymbol{b}}{\partial t} = \boldsymbol{B_0} \cdot \boldsymbol{\nabla} \boldsymbol{u} + \eta \nabla^2 \boldsymbol{b}. \tag{2.23}$$

Eq. 2.23 simplifies, since QSA states the induced field adapts instantaneously to the applied field or $\partial \boldsymbol{b}/\partial t = 0$, which gives

$$-\boldsymbol{B_0} \cdot \boldsymbol{\nabla} \boldsymbol{u} = \eta \nabla^2 \boldsymbol{b}. \tag{2.24}$$

Next, we show that the treatment of the Lorentz force in Eq. 2.20

$$\boldsymbol{F_L} = \boldsymbol{j} \times \boldsymbol{B}, \tag{2.25}$$

can also be simplified through QSA, before turning to the governing equations unique to the setup considered in this study.

2.3.1 Equivalence of Quasistatic Potential and Induction Formulations

Simplifying the Lorentz force under QSA has been treated in previous studies two different ways: using Ohm's Law to find the current density, which is known as the potential formulation, or by using the relationship

$$\mu \boldsymbol{j} = (\boldsymbol{\nabla} \times \boldsymbol{B}) \tag{2.26}$$

where μ is the magnetic permeability, which is known as the induction formulation (Zikanov et al., 2021). We demonstrate here that both frameworks are equivalent, which allows us to utilize the potential formulation to calculate the Lorentz force in our model. In addition, we employ the induction formulation to demonstrate the tendency for the Lorentz force to dampen velocity gradients parallel to the magnetic field. This general MHD formalism applies to both 3D and 2D set ups with a uniform vertical magnetic field now defined by

$$\boldsymbol{B} = B_0 \hat{\boldsymbol{y}} + \boldsymbol{b}. \tag{2.27}$$

2.3.1.1 Potential Formulation

The Lorentz force is given by Eq. 2.25. We can use Faraday's Law to write the electric field $\boldsymbol{E}$ in terms of the magnetic vector potential $\boldsymbol{A}$,

$$\boldsymbol{\nabla} \times \boldsymbol{E} = -\frac{\partial}{\partial t}\boldsymbol{B} = \frac{\partial}{\partial t}(\boldsymbol{\nabla} \times \boldsymbol{A}) = 0, \tag{2.28}$$

which gives an equation for the electric field

$$\boldsymbol{E} = -\nabla \phi - \frac{\partial}{\partial t}\boldsymbol{A}. \tag{2.29}$$

Under QSA, $\partial \boldsymbol{A}/\partial t = 0$. Thus, the electric field can be expressed purely using a scalar potential, ϕ

$$\boldsymbol{E} = -\nabla \phi. \tag{2.30}$$

Using Ohm's Law for the current density yields

$$\boldsymbol{j} = \sigma(\boldsymbol{E} + \boldsymbol{u} \times \boldsymbol{B}) = \sigma(-\nabla \phi + B_0 \boldsymbol{u} \times \hat{\boldsymbol{y}}), \tag{2.31}$$

where σ is the electrical conductivity. Taking the curl of Eq. 2.31 gives

$$\boldsymbol{\nabla} \times \boldsymbol{j} = \sigma B_0 \frac{\partial \boldsymbol{u}}{\partial y}. \tag{2.32}$$

The Lorentz force can also be expressed through the following vector identity:

$$\boldsymbol{\nabla} \times \boldsymbol{\nabla} \times \boldsymbol{F_L} = \boldsymbol{\nabla}(\boldsymbol{\nabla} \cdot \boldsymbol{F_L}) - \boldsymbol{\nabla}^2 \boldsymbol{F_L}. \tag{2.33}$$

Substitution of Eq. 2.32 into the curl of the curl of Eq. 2.25 yields,

$$\boldsymbol{\nabla} \times \boldsymbol{\nabla} \times \boldsymbol{F_L} = \sigma B_0^2 \Big(\frac{\partial^2 \boldsymbol{u}}{\partial y^2}\Big). \tag{2.34}$$

The gradient of the divergence of Eq. 2.25 gives,

$$\boldsymbol{\nabla}(\boldsymbol{\nabla} \cdot \boldsymbol{F_L}) = \boldsymbol{\nabla}(\sigma B_0^2 \frac{\partial u_y}{\partial y}). \tag{2.35}$$

Eq. 2.34 and Eq. 2.35 allow us to rewrite Eq. 2.33 as

$$\boldsymbol{\nabla}^2 \boldsymbol{F_L} = \boldsymbol{\nabla}\Big(\sigma B_0^2 \frac{\partial u_y}{\partial y}\Big) - \sigma B_0^2 \Big(\frac{\partial^2 \boldsymbol{u}}{\partial y^2}\Big). \tag{2.36}$$

2.3.1.2 Induction Formulation

Instead of Ohm's law to define the current density, we use the induction formulation, given by Eq. 2.26

$$\boldsymbol{j} = \frac{1}{\mu}(\boldsymbol{\nabla} \times \boldsymbol{B}). \tag{2.37}$$

The Lorentz force density, Eq. 2.25, becomes,

$$\boldsymbol{F_L} = \frac{1}{\mu}(\boldsymbol{\nabla} \times \boldsymbol{B} \times \boldsymbol{B}) = -\boldsymbol{\nabla}\Big(\frac{1}{2\mu}\boldsymbol{B}^2\Big) + \frac{1}{\mu}(\boldsymbol{B} \cdot \boldsymbol{\nabla})\boldsymbol{B}. \tag{2.38}$$

Eq. 2.38 can be simplified by substituting $\boldsymbol{B} = B_0 \hat{\boldsymbol{y}} + \boldsymbol{b}$,

$$\frac{1}{\mu}(\boldsymbol{B} \cdot \boldsymbol{\nabla})\boldsymbol{B} = \frac{1}{\mu}\Big(B_0 \frac{\partial \boldsymbol{b}}{\partial y}\Big), \tag{2.39}$$

where terms $\mathcal{O}(\boldsymbol{b}^2)$ have been neglected. The remaining leading order terms of Eq. 2.38 can be written as,

$$-\boldsymbol{\nabla}\Big(\frac{1}{2\mu}\boldsymbol{B}^2\Big) = -\boldsymbol{\nabla}\Big(\frac{1}{\mu}B_0 b_y\Big). \tag{2.40}$$

The Lorentz force expressed using Eq. 2.38, Eq. 2.39, and Eq. 2.40 is

$$\boldsymbol{F_L} = -\boldsymbol{\nabla}\Big(\frac{1}{\mu}B_0 b_y\Big) + \frac{1}{\mu}\Big(B_0\frac{\partial \boldsymbol{b}}{\partial y}\Big). \tag{2.41}$$

The first term on the right hand side of Eq. 2.41 is irrotational, and represents a magnetic pressure (Roberts, 1967). The second term is the rotational component of the Lorentz force. The magnetic induction equation under QSA with a uniform vertical magnetic field reduces to

$$B_0\frac{\partial \boldsymbol{u}}{\partial y} = -\eta\nabla^2\boldsymbol{b}, \tag{2.42}$$

and can be used to simplify Eq. 2.41. Solving Eq. 2.42 for the induced field, $\boldsymbol{b}$, gives

$$\boldsymbol{b} = -\frac{B_0}{\eta}\Delta^{-1}\frac{\partial \boldsymbol{u}}{\partial y}, \tag{2.43}$$

where Δ^{-1} is the inverse Laplacian operator. The Lorentz force simplifies to

$$\boldsymbol{F_L} = \boldsymbol{\nabla}\Big(\frac{B_0^2}{\mu\eta}\Delta^{-1}\frac{\partial u_y}{\partial y}\Big) - \frac{B_0^2}{\mu\eta}\Delta^{-1}\frac{\partial^2 \boldsymbol{u}}{\partial y^2}. \tag{2.44}$$

Taking the Laplacian of both sides, we find

$$\boldsymbol{\nabla}^2\boldsymbol{F_L} = \boldsymbol{\nabla}\Big(\sigma B_0^2\frac{\partial u_y}{\partial y}\Big) - \sigma B_0^2\Big(\frac{\partial^2 \boldsymbol{u}}{\partial y^2}\Big), \tag{2.45}$$

where $\sigma = 1/(\mu\eta)$. This is identical to Eq. 2.36, which shows that the potential formulation and the induction formulation for the current density yield the same Lorentz force. Beyond demonstrating the equivalence of two formulations commonly used in the literature, we can observe an important characteristic of the Lorentz force under QSA. Namely, following Eq. 2.44, the Lorentz force tends to dampen velocity gradients parallel to the magnetic field (Schumann, 1976; Sommeria and Moreau, 1982; Knaepen and Moreau, 2008; Pothérat and Klein, 2014; Zikanov et al., 2021), and that this holds for both potential and induction formulations.

2.3.2 Quasi-2D RBC Governing Equations

Next, we turn to the equations considered in this study in which the potential formulation is used to simplify the Lorentz force term. They are the quasi-2D Cartesian Navier-Stokes equations for Rayleigh-Bénard convection (RBC) under the Oberbeck-Boussinesq approximation. We include a quasistatic magnetic field parallel to the direction of buoyancy. The horizontally periodic domain has stress-free velocity boundary conditions and fixed temperature boundary conditions. The dimensional governing equations for the velocity $\boldsymbol{u}(x, y, t)$ and temperature $T(x, y, t)$ fields are:

$$\boldsymbol{\nabla} \cdot \boldsymbol{u} = 0, \tag{2.46}$$

$$\boldsymbol{\nabla} \cdot \boldsymbol{B} = 0, \tag{2.47}$$

$$\frac{\partial \boldsymbol{u}}{\partial t} + (\boldsymbol{u} \cdot \boldsymbol{\nabla})\boldsymbol{u} = -\frac{1}{\rho_0}\boldsymbol{\nabla} p + \alpha g(T - T_0)\hat{\boldsymbol{y}} + \nu \boldsymbol{\nabla}^2 \boldsymbol{u} + \frac{1}{\rho_0}(\boldsymbol{j} \times \boldsymbol{B}), \tag{2.48}$$

$$\frac{\partial T}{\partial t} + (\boldsymbol{u} \cdot \boldsymbol{\nabla})T = \kappa \nabla^2 T, \tag{2.49}$$

where p is the pressure, ρ_0 is the constant mass density, α is the coefficient of thermal expansion, g is gravitational acceleration, T_0 is the reference temperature, ν is the viscosity, and κ is the thermal diffusivity.

In the quasi-2D configuration, forces are permitted in the third, $\hat{\boldsymbol{z}}$-direction, though $\boldsymbol{u}$ and T remain independent of z. Furthermore, we apply the additional condition, $u_z = 0$. This allows us to calculate the cross-product of the Lorentz term in *Eq.*2.48. The Lorentz force density, $\boldsymbol{f_L}$, is given by

$$\boldsymbol{f_L} = \frac{\boldsymbol{F_L}}{\rho_0} = \frac{1}{\rho_0}(\boldsymbol{j} \times \boldsymbol{B}). \tag{2.50}$$

We can again decompose the field into applied and induced components, $\boldsymbol{B} = B_0\hat{\boldsymbol{y}} + \boldsymbol{b}$. Following the potential formulation given by Eq. 2.28-Eq. 2.30 yields a Poisson equation

$$\boldsymbol{\nabla}^2 \phi = \boldsymbol{\nabla} \cdot (\boldsymbol{u} \times \boldsymbol{B}). \tag{2.51}$$

For this quasi-2D setup, the right hand side can be simplified,

$$\boldsymbol{\nabla} \cdot (\boldsymbol{u} \times B_0\hat{\boldsymbol{y}}) = \frac{\partial}{\partial z} u_x B_0 = 0, \tag{2.52}$$

to obtain a Laplace equation for the electrostatic potential

$$\boldsymbol{\nabla}^2 \phi = 0. \tag{2.53}$$

Using perfectly insulating ($\frac{\partial}{\partial n}\phi = 0$), perfectly conducting ($\phi = 0$), or any combination of these two boundary conditions for the electric field at the wall, gives

$$\boldsymbol{\nabla}\phi = 0. \tag{2.54}$$

Using Eq. 2.31 for the current density, and applying the quasistatic approximation, we find

$$\boldsymbol{f_L} = \frac{\sigma}{\rho_0}((\boldsymbol{u} \times \boldsymbol{B}) \times \boldsymbol{B}) = \frac{\sigma}{\rho_0}(u_x B_0 \hat{\boldsymbol{z}} \times B_0 \hat{\boldsymbol{y}}) = -\frac{\sigma B_0^2}{\rho_0} u_x \hat{\boldsymbol{x}}. \tag{2.55}$$

Eq. 2.46 - Eq. 2.49, are integrated in the vorticity-stream function formulation. The vorticity, $\boldsymbol{\omega}$, is defined as the curl of the velocity field, where

$$\boldsymbol{\omega} = \boldsymbol{\nabla} \times \boldsymbol{u}. \tag{2.56}$$

Because $u_z = 0$ and $\partial_z = 0$, the vorticity vector is

$$\boldsymbol{\omega} = \left(\frac{\partial u_x}{\partial y} - \frac{\partial u_y}{\partial x}\right)\hat{\boldsymbol{z}} = \omega_z \hat{\boldsymbol{z}}. \tag{2.57}$$

The stream function ψ can be used to reconstruct the velocity, where

$$u_x = -\frac{\partial}{\partial y}\psi, \; u_y = \frac{\partial}{\partial x}\psi. \tag{2.58}$$

The vorticity is related to the streamfunction with

$$\boldsymbol{\nabla}^2\psi = -\omega_z. \tag{2.59}$$

The vorticity evolution equation is found by taking the curl of Eq. 2.48. Since all the terms in the vorticity equation are in the z-direction, the scalar vorticity equation for the $\hat{\boldsymbol{z}}$-component is

$$\frac{\partial \omega}{\partial t} + (\boldsymbol{u} \cdot \boldsymbol{\nabla})\omega = \alpha g \frac{\partial T}{\partial x} + \nu \nabla^2 \omega + \frac{\sigma B_0^2}{\rho_0}\frac{\partial^2 \psi}{\partial y^2}, \tag{2.60}$$

where we have set $\omega \equiv \omega_z$.

2.3.3 Numerical Method

The approach used to numerically solve the governing equations is given here. First, to nondimensionalize the system, the length is scaled by the height of the domain, H, time by the free-fall time scale, $\tau_{ff} = H/\sqrt{\alpha g \Delta T}$, temperature by the temperature difference from the hot bottom to the cold top boundary in the static state, ΔT, and magnetic field by B_0. Under these scales, the nondimensional velocity, known as the free-fall velocity, is given by

$$u_{ff} = \sqrt{\alpha g \Delta T H}. \tag{2.61}$$

The quasi-2D nondimensional equations for quasistatic magnetoconvection in the vorticity-stream function formulation are

$$\frac{\partial \omega}{\partial t} + (\boldsymbol{u} \cdot \boldsymbol{\nabla})\omega = \frac{\partial T}{\partial x} + \sqrt{\frac{Pr}{Ra}}\nabla^2 \omega + \sqrt{\frac{Ch^2 Pr}{Ra}}\frac{\partial^2 \psi}{\partial y^2}, \tag{2.62}$$

$$\frac{\partial T}{\partial t} + (\boldsymbol{u} \cdot \boldsymbol{\nabla})T = \frac{1}{\sqrt{Ra\ Pr}}\nabla^2 T, \tag{2.63}$$

along with 2.59 and 2.58, which are solved using direct numerical simulations (DNS). The Rayleigh number (Ra, ratio of buoyancy to diffusion) is given by

$$Ra = \frac{\alpha g \Delta T H^3}{\nu \kappa}, \tag{2.64}$$

the Prandtl number (Pr, ratio of viscous to thermal diffusion) by,

$$Pr = \frac{\nu}{\kappa}, \tag{2.65}$$

and Chandrasekhar number (Ch, ratio of Lorentz to viscosity) by

$$Ch = \frac{\sigma B_0^2 H^2}{\rho_0 \nu}. \tag{2.66}$$

The aspect ratio of the domain is defined by $\Gamma = L/H$ where L is the length and H is the height. We fix $Pr = 1$ and $\Gamma = 2$ for this study, and vary $10^3 \leq Ra \leq 10^{10}$ and $0 \leq Ch \leq 10^6$.

Our main output parameters are the Nusselt number, Nu, which defines the heat transfer across the layer, and the Reynolds number, Re, which defines the momentum transport. The equations for each are

$$Nu = 1 + \frac{H\langle u_y T\rangle_{x,y}}{\kappa \Delta T}, \tag{2.67}$$

where $\langle\rangle_{x,y}$ refers to the area average, and

$$Re_x = \frac{\langle |u_x|\rangle_{x,y} H}{\nu}, \ Re_y = \frac{\langle |u_y|\rangle_{x,y} H}{\nu}. \tag{2.68}$$

A more general Reynolds number is defined by

$$Re = \frac{UH}{\nu}, \tag{2.69}$$

where U is a characteristic velocity scale. Eq. 2.69 will be used when testing scaling laws for this system.

To perform a majority of the DNS, we have developed an MPI parallelized, pseudo-spectral solver that numerically integrates the governing equations 2.62-2.63 at each time step with the following process: it calculates the linear terms of 2.62 and 2.63, transforms the solution to physical space to calculate the nonlinear terms, updates the temperature field and vorticity field, solves the Poisson equation for the streamfunction based on the vorticity field, and finally updates the velocity field. The code utilizes m Fourier modes in the periodic x direction, and solves the resulting equations using a second-order accurate finite difference scheme in y (Glatzmaier, 2014).

The grid-spacing is non-uniform with Chebyshev mapping for finer resolution at the top and bottom boundaries defined by

$$y_k = \frac{1}{2}\left(1 - cos\left(\frac{k\pi}{n_y}\right)\right) \text{ for } k = 1, ...n_y \tag{2.70}$$

where y_k is vertical location at each grid point k and n_y is the total number of vertical grid points (Glatzmaier, 2014). The nonlinear terms are calculated using a spectral-transform method, and the solutiond is advanced in time using a second-order Adams-Bashforth time integration scheme.

For the most numerically challenging cases with turbulent intermittent convective bursts ($Ra \geq 10^9$), the simulations are carried out using the DNS code DEDALUS (Burns et al., 2020). Dedalus is a flexible, open-source pseudo-spectral code that employs MPI parallelization and multidimensional block distributions when decomposing the spectral domains in parallel. The domains are can be represented by the direct product of spectral bases, which can be separable or coupled. The multidimensional parallelization scheme has the advantage of scaling better on a larger number of cores than the code developed for this study. Both codes are benchmarked to (Goluskin et al., 2014), as shown in Appendix A.1.

2.3.4 Marginal Stability Analysis

To understand nonlinear magnetoconvection, we first develop predictions for the linear behaviors. Marginal stability analysis (Glatzmaier, 2014; Chandrasekhar, 1961) can be used to find Ra_{mar}, the marginally unstable Rayleigh number as a function of aspect ratio and horizontal Fourier mode number, m,

$$Ra_{mar}(m, Ch, \Gamma) = \frac{(\Gamma^2 + m^2)(Ch\, \Gamma^4 \pi^2 + (\Gamma^2 + m^2)m^4)}{\Gamma^4 m^2}. \tag{2.71}$$

In doing so, we have assumed that structures that extend from bottom to top of the box are the most unstable such that the vertical mode number is equal to 1. The critical horizontal mode number, m_c, found by setting the derivative of Eq. 2.71 with respect to m to zero, is given by

$$m_c = \Gamma \sqrt{\frac{\chi^{4/3} + \pi^{4/3} - (\pi\chi)^{2/3}}{2(\pi\chi)^{2/3}}}. \tag{2.72}$$

where

$$\chi = \sqrt{Ch} + \sqrt{Ch + \pi^2}. \tag{2.73}$$

It is then possible to substitute Eq. 2.72 into Eq. 2.71 to find the critical Rayleigh number, $Ra_c(Ch, \Gamma)$. If Ch is too large at a given Ra such that $Ra < Ra_c$, convection is suppressed, and at $Ra = Ra_c$ magnetoconvection motions begin. Furthermore, in the limit $Ch \to \infty$

$$m_c \to \Gamma\left(\frac{Ch}{2\pi^2}\right)^{1/6}, \tag{2.74}$$

and

$$Ra_c \to \pi^2 Ch, \tag{2.75}$$

in agreement with (Chandrasekhar, 1961; Proctor and Weiss, 1982; Matthews, 1999; Glatzmaier, 2014; Yan et al., 2019). Finally, the critical nondimenisonal horizontal wavelength λ_c can be found through the critical horizontal wavenumber

$$k_c = \frac{2\pi m_c}{\Gamma}. \tag{2.76}$$

Using k_c, the critical horizontal wavelength λ_c is inversely related to m_c by

$$\lambda_c = \frac{2\pi}{k_c} = \frac{\Gamma}{m_c}, \tag{2.77}$$

which physically represents the horizontal wavelength of the convective structures. The critical length scale of the convective structures, or half the wavelength, is given by

$$l_c = \frac{\Gamma}{2m_c}. \tag{2.78}$$

In the limit of $Ch \to \infty$, l_c^∞ is given by

$$l_c^\infty = \left(\frac{1}{2}\right)\left(\frac{Ch}{2\pi^2}\right)^{-1/6}. \tag{2.79}$$

Fig. 2.5 shows l_c, the critical horizontal length scale following Eq. 2.78 and its asymptotic behavior as $Ch \to \infty$. Length scales found in this study will be compared to these values.

2.4 The Interaction Parameter

The magnetic field modifies convection by changing the dominant perpendicular length scale, and suppressing flow perpendicular to the applied field. The underlying theory relies on

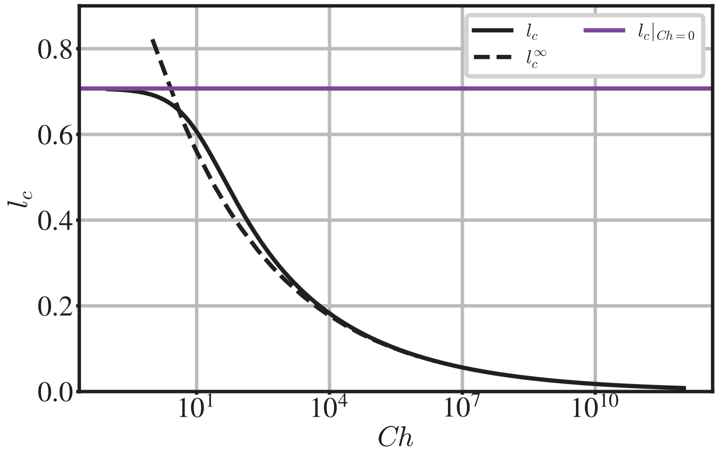

Figure 2.5: The critical horizontal length scale l_c as predicted by linear theory. The solid black line gives the length scale following Eq. 2.78, and the solid purple line gives the result of Eq. 2.78 for $Ch = 0$, the hydrodynamic case. The black dashed line shows the asymptotic behavior given by Eq. 2.79.

one of the most notable characteristics of magnetohydrodynamics: the ability for flows to generate electrical currents. The currents lead to Joule dissipation, which in addition to viscous dissipation, contributes to the total energy loss in the system (Knaepen and Moreau, 2008; Shishkina et al., 2017).

Joule dissipation plays a key role in the magnetic braking process and has been discussed at depth in previous studies (Sommeria and Moreau, 1982; Knaepen and Moreau, 2008; Pothérat and Klein, 2014; Zikanov et al., 2021). In order to demonstrate how the Lorentz force results in Joule dissipation, we first separate the Lorentz force into rotational and irrotational components. In systems where gradients parallel to the direction of the magnetic field are small, the irrotational component of Eq. 2.44 can be neglected, which only leaves the rotational component of the Lorentz force,

$$\boldsymbol{f_{L,R}} = -\frac{\sigma B_0^2}{\rho_0}\Delta^{-1}\frac{\partial^2 \boldsymbol{u}}{\partial y^2}. \tag{2.80}$$

The vorticity equation Eq. 3.53 can be rewritten to include the curl of Eq. 2.80,

$$\frac{\partial \omega}{\partial t} + (\boldsymbol{u} \cdot \boldsymbol{\nabla})\omega = \alpha g \frac{\partial T}{\partial x} + \nu \nabla^2 \omega - \frac{\sigma B_0^2}{\rho_0} \Delta^{-1} \frac{\partial^2 \omega}{\partial y^2}. \tag{2.81}$$

Assuming that the viscous and Lorentz terms of Eq. 2.81 are in balance with the unsteady term, we have

$$\frac{\partial \omega}{\partial t} = \nu \nabla^2 \omega - \frac{\sigma B_0^2}{\rho_0} \Delta^{-1} \frac{\partial^2 \omega}{\partial y^2}. \tag{2.82}$$

Local viscous and Joule dissipation timescales can be estimated using Eq. 2.82. To do this, we can scale the following quantities,

$$\frac{\partial^2}{\partial y^2} \sim \frac{1}{l_\parallel^2}, \ \frac{\partial^2}{\partial x^2} \sim \frac{1}{l_\perp^2}, \tag{2.83}$$

where the subscripts $\parallel, \perp$ denote quantities parallel/perpendicular to the direction of the applied magnetic field respectively. The vorticity ω will then decay on one of two timescales. The viscous timescale is $\tau_\nu = l_\parallel^2/\nu$ according to the first term on the right hand side of Eq. 2.82. The Joule dissipation timescale, τ_j is given by the second term on the right side of Eq. 2.82. Thus, for a given eddy of size $\Delta^{-1} \sim l_\perp$, the Lorentz term can be thought of as a diffusion term similar to viscosity (Sommeria and Moreau, 1982). The Joule dissipation timescale can be written as

$$\tau_j = \frac{\rho_0}{\sigma B_0^2} \left(\frac{l_\parallel}{l_\perp} \right)^2, \tag{2.84}$$

where the dominant term from Δ^{-1} reduces to $l_\perp^2$ under the assumption that gradients parallel to the magnetic field have been suppressed. Taking the ratio of Eq. 2.84 to an eddy turnover time, $\tau_U = l_\perp/U$ leads to a local interaction parameter

$$N_l = \frac{\tau_U}{\tau_{j,l}} = \frac{\sigma B_0^2 l_\perp}{\rho_0 U} \left(\frac{l_\perp}{l_\parallel} \right)^2. \tag{2.85}$$

Eq. 2.85 has been shown to capture the Lorentz force relative to inertia in experimental studies of MHD channel flows (Sreenivasan and Alboussière, 2002; Pothérat and Klein, 2014). Rewriting Eq. 2.85 in terms of Ch, Re, which will be utilized in Sec. 2.5.2, gives

$$N_l = \frac{Ch}{Re} \left(\frac{l_\perp}{H} \right)^3. \tag{2.86}$$

Eq. 2.84 reduces to

$$\tau_j = \frac{\rho_0}{\sigma B_0^2}, \tag{2.87}$$

in cases where flow gradients parallel to the magnetic field are not suppressed and $l_\perp \sim l_\parallel$. Comparing this simplified Joule dissipation time to an eddy turnover time leads to the large-scale interaction parameter

$$N = \frac{\tau_U}{\tau_j} = \frac{\sigma B_0^2 l_\perp}{\rho_0 U}. \tag{2.88}$$

Note that writing Eq. 2.88 in terms of nondimensional parameters, Ch and Re, gives

$$N = \frac{Ch}{Re}\left(\frac{l_\perp}{H}\right). \tag{2.89}$$

Eqns. 2.86 and 2.89 give two representations of the interaction parameter that can be used to treat the end-member flows expected in this system. Eq. 2.86 is used for those controlled by the applied magnetic field, B_0, and Eq. 2.89 is used for those with large-scale jets and strong shear in the direction of the magnetic field.

Fig. 2.6 further demonstrates the importance of the Joule dissipation time scale. In the diagram, a vertical, uniform magnetic field $\boldsymbol{B} = B_0\hat{\boldsymbol{y}}$ is perpendicular to the flow $\boldsymbol{u} = u_0\hat{\boldsymbol{x}}$. The Lorentz force generated through such an interaction is given by

$$\boldsymbol{f_L} = \frac{\sigma}{\rho}((\boldsymbol{u} \times \boldsymbol{B}) \times \boldsymbol{B}). \tag{2.90}$$

Simplifying Eq. 2.90 leads to

$$\boldsymbol{f_L} = \frac{\sigma u_0 B_0^2}{\rho}((\hat{\boldsymbol{x}} \times \hat{\boldsymbol{y}}) \times \hat{\boldsymbol{y}}). \tag{2.91}$$

Carrying out the cross products gives

$$\boldsymbol{f_L} = \frac{\sigma u_0 B_0^2}{\rho}\hat{\boldsymbol{x}}. \tag{2.92}$$

where u_0 is the magnitude of the fluid velocity in the $\hat{\boldsymbol{x}}$-direction. We see that the Lorentz force generated from the motion of a conducting fluid perpendicular to the magnetic field

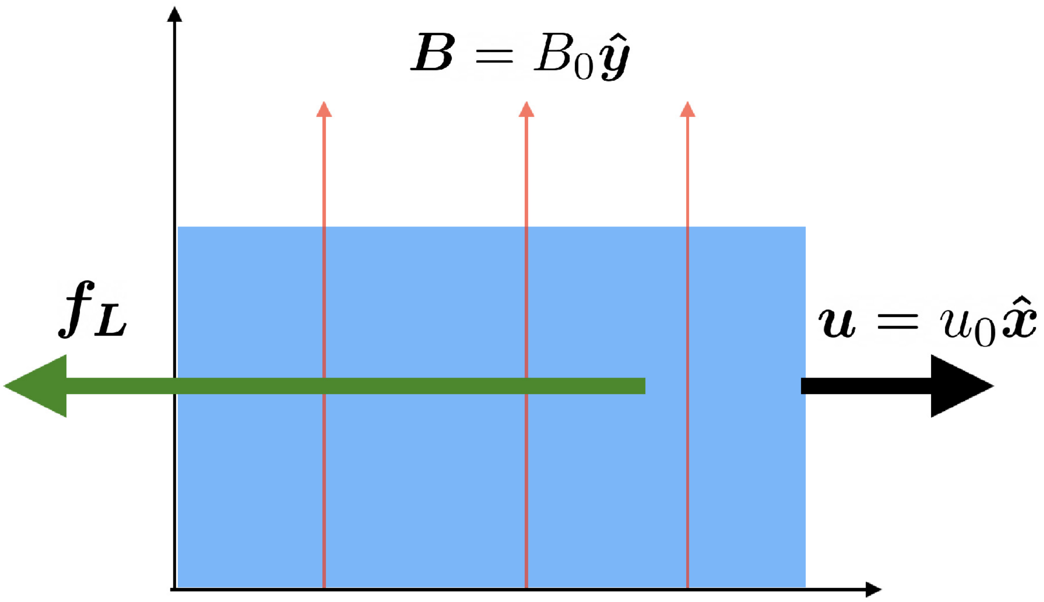

Figure 2.6: Simplified schematic to demonstrate how a vertical, uniform magnetic field $\boldsymbol{B} = B_0\hat{\boldsymbol{y}}$ (red arrows) could resist a flow perpendicular to it, $\boldsymbol{u} = u_0\hat{\boldsymbol{x}}$ (black arrow) through the Lorentz force generated in the $-\hat{\boldsymbol{x}}$-hat direction (green line). The fluid layer (blue) is assumed to be conducting.

direction will *damp* the initial fluid velocity. In addition, we can recast Eq. 2.92 in terms of the Joule damping time, $\tau_j = \rho/\sigma B_0^2$ (Knaepen and Moreau, 2008), and we find that

$$\boldsymbol{f_L} = -\frac{u_0}{\tau_j}\hat{\boldsymbol{x}}. \tag{2.93}$$

If B_0 is large and τ_j is small, $\boldsymbol{f_L}$ will grow quickly to resist u_0 at a timescale governed by τ_j.

2.5 Regime characteristics and interaction parameter dependence

The regimes in this study are distinguished quantitatively by their length scale, momentum transport, and time-dependence. The regimes are

1. Steady Convection Rolls,

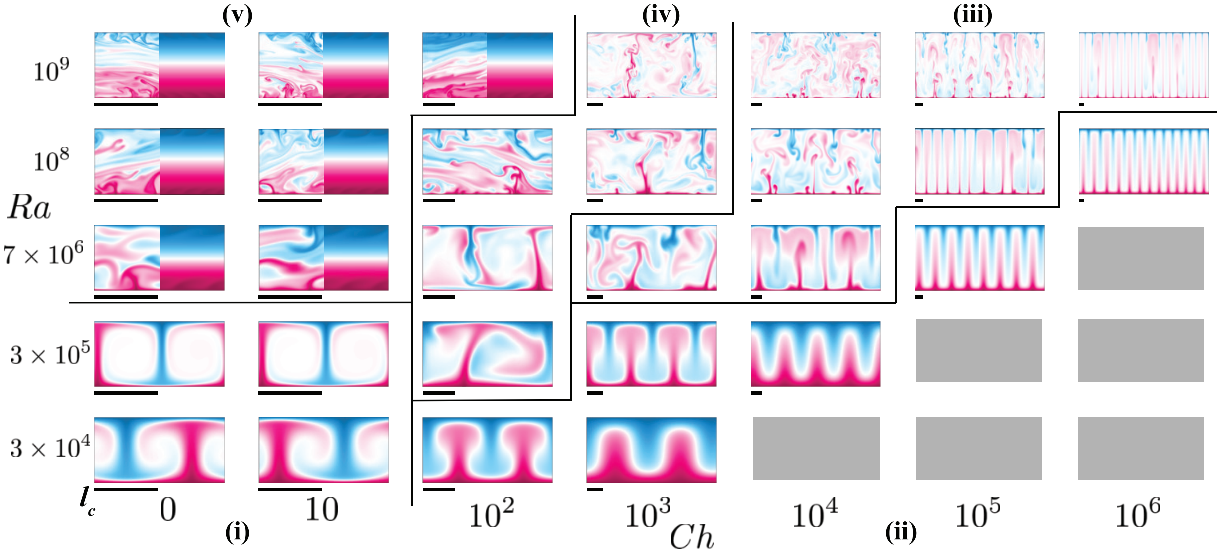

Figure 2.7: Instantaneous temperature fields for $10^4 \leq Ra \leq 10^9$ and $10 \leq Ch \leq 10^6$. The grey boxes are sub-critical, while the black lines correspond to regime boundaries. For some cases in the Burst-Jet regime (v), the left half of the domain shows a snapshot in the convective burst phase (image truncated at $x = \Gamma/2$), and the right half of the domain shows a snapshot in the jet phase (image truncated at $x = \Gamma/2$). The thick black line under each snapshot gives l_c as predicted by 2.78 with m_c to the nearest integer.

2. Steady Magneto-Columns,

3. Unsteady to Turbulent Magneto-Plumes (“Magneto-Plumes”)

4. Horizontally Drifting Magneto-Plumes (“Drifting Plumes”)

5. Jets with Intermittent Turbulent Convective Bursts (“Burst-Jet”)

Each of the five regimes has distinct morphological behaviors similar to those found in previous studies of magnetoconvection (Yan et al., 2019; Zürner, 2020) and rotating convection (Nieves et al., 2014; Stellmach et al., 2014; Horn and Aurnou, 2018; Kunnen, 2021; Madonia et al., 2021).

Fig. 2.7 presents instantaneous temperature fields for an array of cases between $3 \times 10^4 \leq$

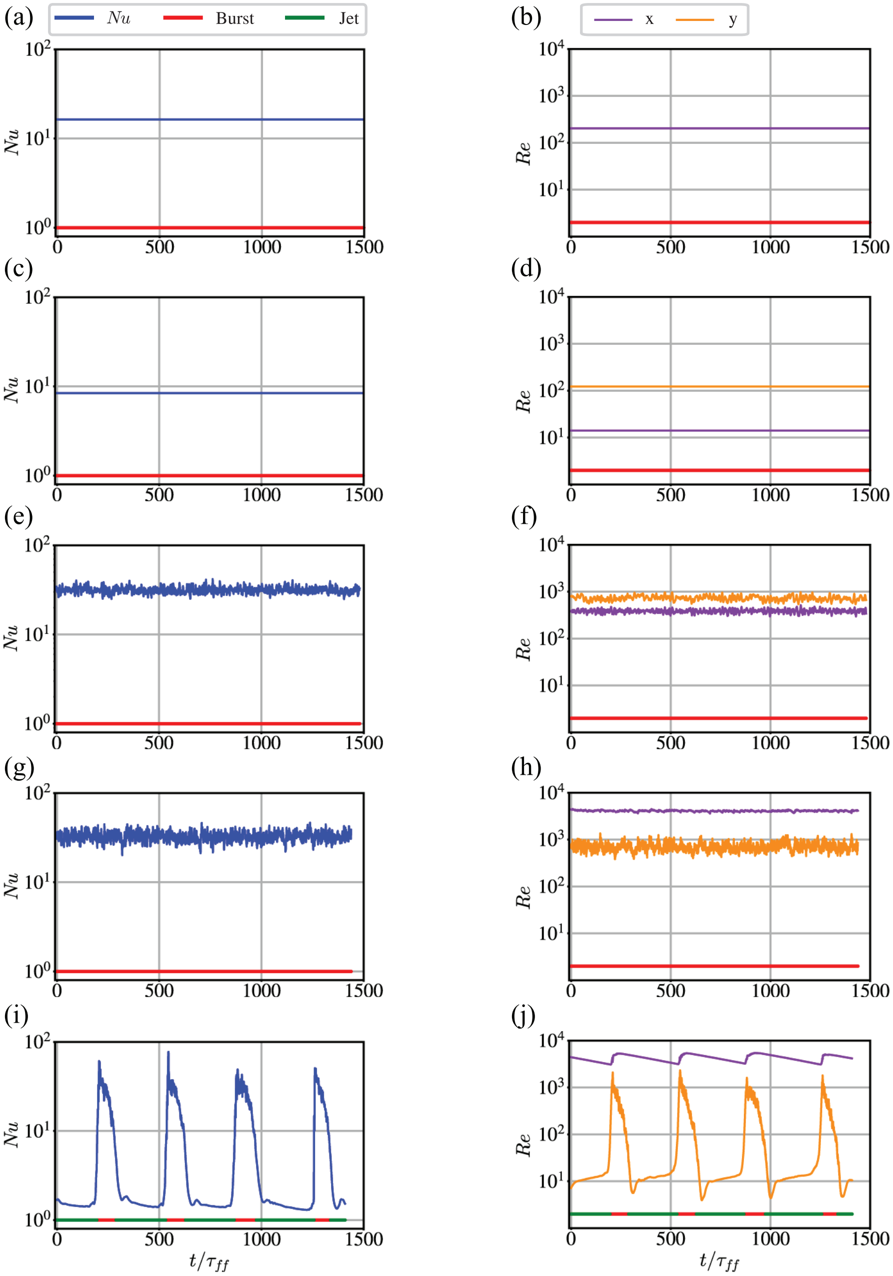

Figure 2.8: The left column shows the times series of Nu, and the right column $\langle|Re_x|\rangle_{x,y}$, (purple) $\langle|Re_y|\rangle_{x,y}$ (orange). Each row corresponds to $Ra = 10^8, Ch = 10$ (Burst-Jet Regime), $Ra = 10^8, Ch = 10^2$ (Drifting Plumes Regime), and $Ra = 10^8, Ch = 10^4$ (Magneto-Plume Regime) shown in (a,b), (c,d), (e,f) respectively. In the left column, the green and red markers correspond to points separated into the burst or jet phase based on 2.94. The remaining two regimes, Steady Convection Roll and Steady-Magneto Columns do not vary time, and are not shown in this figure.

$Ra \leq 10^9$ and $0 \leq Ch \leq 10^6$. Fig. 2.7(i) shows cases in the Steady Convection Roll regime (i), which have one steady convection roll. The perpendicular length scale of the roll is given by $l_\perp = 1$, and in this regime the strength of the magnetic field relative to buoyancy is small enough such that the weakly nonlinear dynamics characteristic of steady RBC are not drastically modified (Grossmann and Lohse, 2000; Zürner et al., 2016). Fig. 2.7(ii) shows those in Steady Magneto-Columns regime (ii). These cases are characterized by a series of narrow, steady convective columnar structures. The width of these columns closely follows linear theory, which will be shown further in Sec. 2.5.1. This regime includes cases that are steady and where $l_\perp < 1$.

Fig. 2.7(iii) encompasses the Magneto-Plume regime (iii). In this regime, the buoyancy forcing is strong enough that nonlinearities develop. The convective plumes transfer heat efficiently and have a classical mushroom-like shape (Hansen et al., 1990; Manga and Weeraratne, 1999; Horn et al., 2013; Cagney et al., 2015). The Lorentz force stabilizes the flow, which is approximately aligned with the vertical magnetic field. Fig. 2.9(a) gives an additional instantaneous temperature field for a case with mushroom-like convective plumes at $Ra = 10^{10}, Ch = 10^5$. The mushroom-like plumes are outlined in the black boxes. Fig. 2.9(b) gives a shadowgraph image adapted from UCLA student Arthur Lo and professor Carolina Lithgow-Bertelloni who carried out convection experiments using corn syrup as working fluid. The white arrows points to similar mushroom-like convective plumes.

Fig. 2.7(iv) shows cases in the Drifting plume regime (iv). In these cases, asymmetries exist in the flow field such that convective plumes drift horizontally, though the jets are not strong enough to completely disperse them. Finally, Fig. 2.7(v) gives cases in the Burst-Jet regime (v), which are characterized by two distinct phases. Over the evolution of a case, a period of high heat transport where convective plumes cross the fluid layer ("burst") are interrupted by quiet phases of weak heat transport, where strong zonal flows ("jets") disperse thermal plumes and inhibit convection (Terry, 2000). The left/right side of the snapshots corresponds to the burst/jet phases respectively.

Figure 2.9: (a) Instantaneous temperature field for a case with mushroom-like convective plumes ($Ra = 10^{10}, Ch = 10^{5}, Pr = 1, \Gamma = L/H = 2$). Examples of the mushroom-like convective plumes are shown in the black boxes. (b) Shadowgraph image courtesy of UCLA student Arthur Lo and professor Carolina Lithgow-Bertelloni, who carried out experiments of convection using corn syrup as a working fluid.

Fig. 2.8 shows a time series of the Nusselt number Nu (left column) and a time series of the vertical and horizontal Reynolds numbers, $Re_y; Re_x$ (right column). It is used to quantitatively distinguish the regimes from one another. Fig. 2.8(a) shows Nusselt for a case in the Steady Convection Roll regime at $Ra = 3 \times 10^5, Ch = 10$ where Nu remains constant at 16.30. Fig. 2.8(b) shows the Reynolds numbers for the same case, where the horizontal and vertical Reynolds numbers are nearly equivalent. Fig. 2.8(c) gives Nusselt for a case in the Steady Magneto-Columns regime at $Ra = 7 \times 10^6, Ch = 10^5$ where Nu remains constant at 8.42. Fig. 2.8(d) allows us to observe a distinguishing characteristic about this regime; the vertical Reynolds number exceeds the horizontal Reynolds number, because flows that are perpendicular to the applied vertical magnetic field damps are damped.

Fig. 2.8(e,f) show the Nusselt number and Reynolds numbers for a case in the Magneto-Plumes regime at $Ra = 10^8, Ch = 10^4$, where small temporal oscillations in each quantity are observed. Furthermore, it is clear from Fig. 2.8(f) that the vertical Reynolds number exceeds the horizontal Reynolds number. Cases are placed in these regime if they are unsteady or turbulent, and if $\langle Re_x \rangle_t \leq \langle Re_y \rangle_t$. The unsteadiness of the flow is quantified by the variance of the vertical velocity in time, or $var(Re_y)$.

Fig. 2.8(g,h) show the Nusselt number and Reynolds numbers for a case in the Drifting Plumes regime at $Ra = 10^8, Ch = 10^2$. Oscillations in the parameters are slightly larger than those in the Magneto-Plumes regime. Fig. 2.8(h) can be used to more explicitly separate the two. In contrast to the previous regime, the horizontal Reynolds number now exceeds the vertical Reynolds number. Therefore, one characteristic of this regime is that it is unsteady or turbulent, and $\langle Re_x \rangle_t > \langle Re_y \rangle_t$.

Fig. 2.8(i,j) show the Nusselt number and Reynolds numbers for a case in the Burst-Jet regime at $Ra = 10^8, Ch = 10$, where strong temporal periodicity is observed in each parameter. We choose to separate the burst and jet phases based on a threshold value

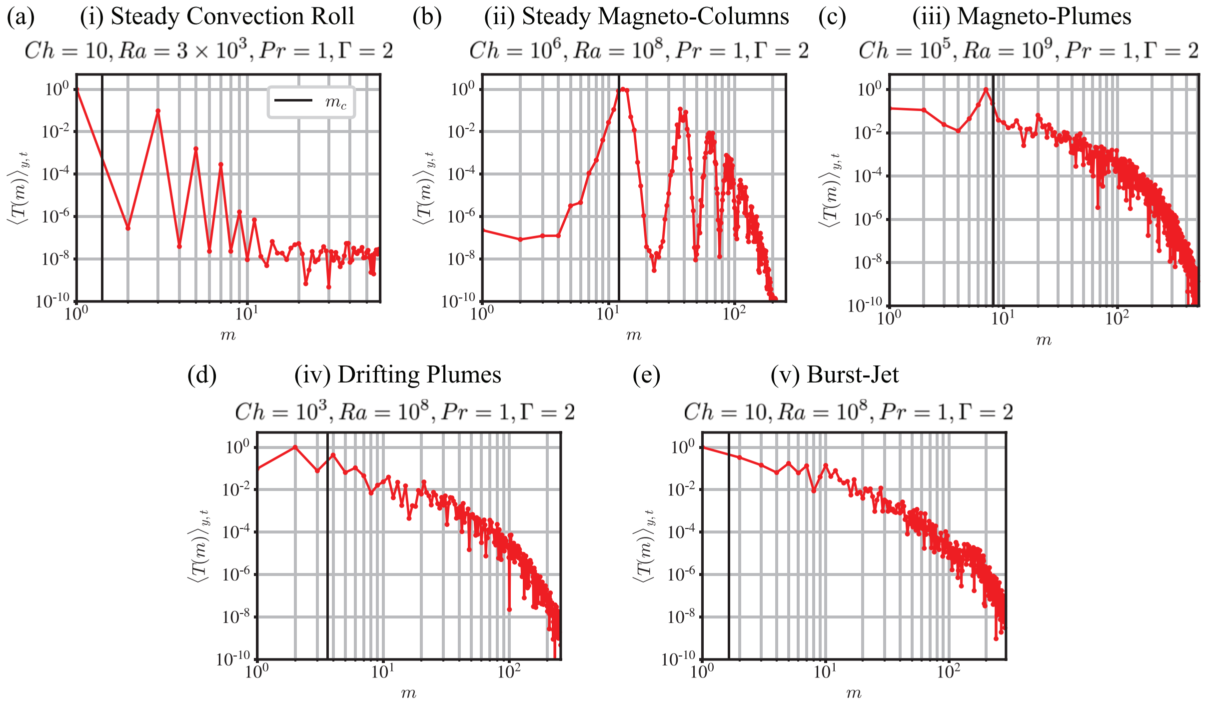
(a) (i) Steady Convection Roll $Ch = 10, Ra = 3 \times 10^3, Pr = 1, \Gamma = 2$

(b) (ii) Steady Magneto-Columns $Ch = 10^6, Ra = 10^8, Pr = 1, \Gamma = 2$

(c) (iii) Magneto-Plumes $Ch = 10^5, Ra = 10^9, Pr = 1, \Gamma = 2$

(d) (iv) Drifting Plumes $Ch = 10^3, Ra = 10^8, Pr = 1, \Gamma = 2$

(e) (v) Burst-Jet $Ch = 10, Ra = 10^8, Pr = 1, \Gamma = 2$

Figure 2.10: Examples of spectra ($T(m)$) from each regime that compare the mode numbers to the spectra peak, m_{peak} to the critical horizontal mode number, m_c. (a) Steady Convection Roll, (b) Steady Magneto-Columns, (c) Magneto-Plumes, (d) Drifting Plumes, and (e) Burst-Jet. The measured perpendicular length scale $l_\perp$ is then given by $l_\perp = \Gamma/2m_{peak}$ following 2.78.

of the instantaneous Nusselt number compared to its mean. If

$$\frac{Nu(t)}{\langle Nu \rangle_t} < \frac{1}{2}, \tag{2.94}$$

the data point is placed in the jet phase; otherwise, it is placed in the burst phase. The time spent in each phase is averaged for each case, yielding values for $t_{jet}/\tau_{ff} = \tau_{jet}$ and $t_{burst}/\tau_{ff} = \tau_{burst}$, respectively. Values of $\tau_{jet} > 0$ are unique to the Burst-Jet regime. Therefore, cases are placed in these regime if they are unsteady or turbulent, $\langle Re_x \rangle_t > \langle Re_y \rangle_t$, and $\tau_{jet} > 0$. If $\tau_{jet} = 0$, it is placed in the prior Drifting Plumes regime. Fig. 2.13(a) gives Nu versus Ra for different values of Ch and the various regimes. We observe that in the Steady Convection Rolls regime, Nu increases directly with Ra for a given value of Ch.

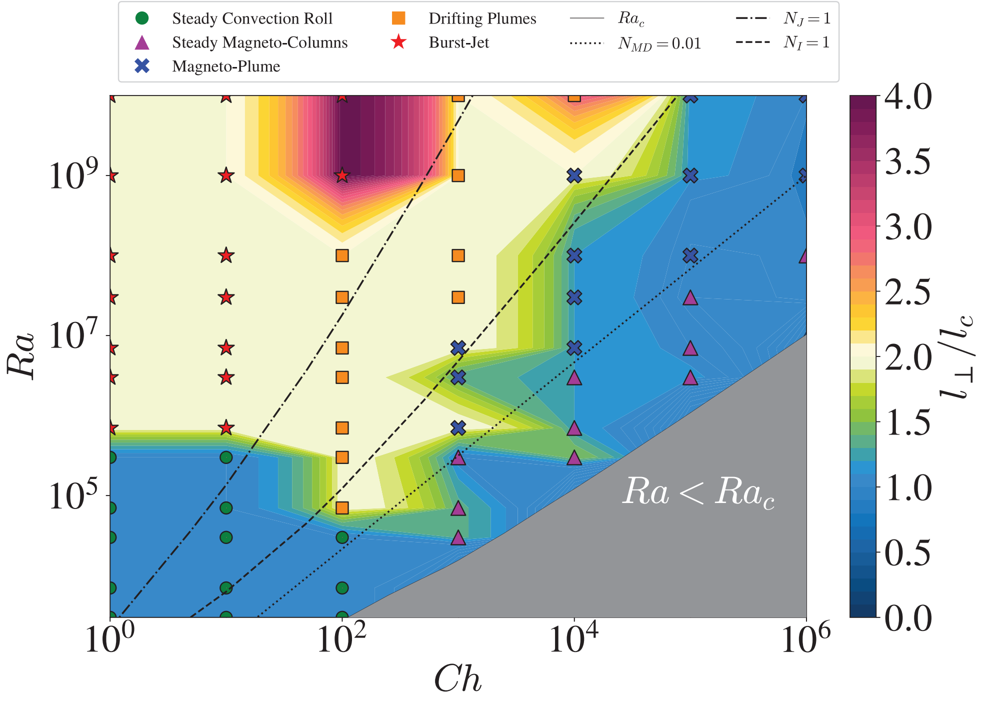

Figure 2.11: Measured perpendicular length scale, $l_\perp$ normalized by the critical length scale predicted by magnetoconvection linear theory, l_c, against all values of Ra, Ch. The horizontal length scale is measured by inverting the peak wavenumber of the vertically and temporally averaged temperature fields.

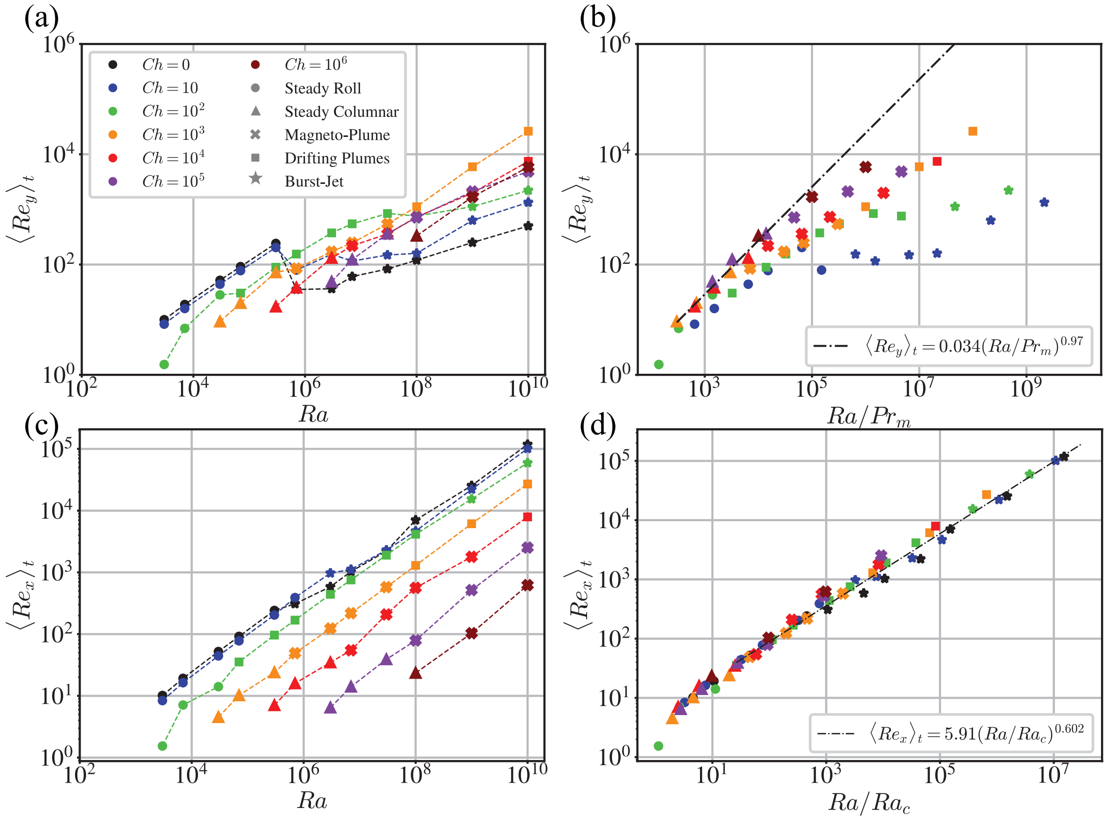

Figure 2.12: Horizontal and vertical flow speeds. (a) Time averaged horizontal Reynolds number, $\langle Re_x \rangle_t$ versus the Rayleigh number. (b) $\langle Re_x \rangle_t$ versus Ra/Ra_c, where the black dashed line gives the power-law fit of the data. (c) Time averaged vertical Reynolds number, $\langle Re_y \rangle_t$ versus the Rayleigh number. (d) $\langle Re_y \rangle_t$ versus Ra/Pr_j, where the black dashed line gives the power-law fit of the data, and Pr_j is defined in Sec. 2.5.1.

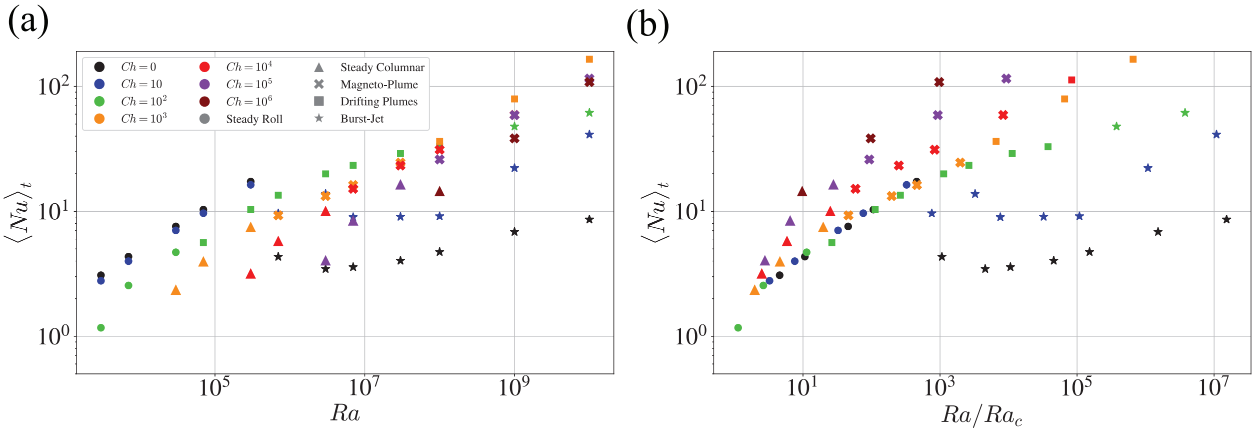

Figure 2.13: Heat transfer compared to buoyancy. (a) Time averaged Nusselt number, $\langle Nu \rangle_t$ versus the Rayleigh number, Ra The colors denote the value of Ch and the markers give the regime classification. (b) $\langle Nu \rangle_t$ versus Ra/Ra_c where Ra_c is the critical Rayleigh number.

And as Ch is raised, the relative strength of Nu decreases as the strength of the magnetic field inhibits convection. A similar trend is observed for the the Steady Magneto-Columnar regime. In the Magneto-Plumes regime, the increase in Nu begins to become shallower with increasing Ra. In the Drifting Plumes regime, the slope of Nu against Ra becomes so shallow that for certain cases, Nu is weaker at lower Ch values. This is because the stronger horizontal flows begin to inhibit convection. Finally in the Burst-Jet regime, there can be a decline in Nu with increasing Ra as the zonal flows completely suppress convection in the jet phase.

These same trends are observed in Fig. 2.13(b), which gives Nu versus Ra/Ra_c. Here, the cases in the Steady Convection Roll regime are nearly collapsed. Different trends are only seen in higher values of Ch. Additionally, the dip in Nu with Ra/Ra_c in the Burst-Jet regime is even more apparent. This behaviour seems to occur near $Ra/Ra_c \approx 1000$.

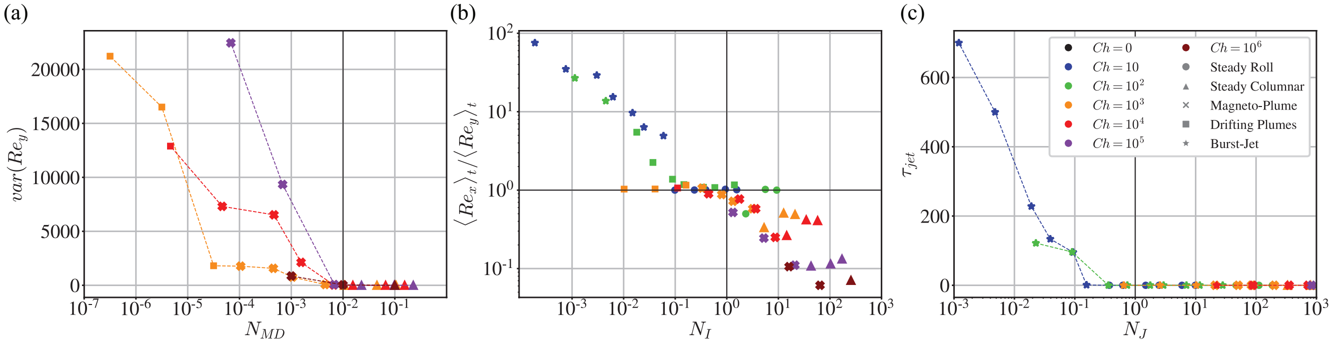

Figure 2.14: Shows how the scaling laws derived in Sec. 2.4 collapse the quantities used to separate the regimes. (a) The variance of Re_y, which characterizes unsteadiness, against the scaling law derived for the transition from the Magneto-Columnar to the Magneto-Plume regime, N_{MC}. Only cases in these two regimes are shown for clarity. (b) The ratio of the horizontal and vertical velocities $\langle Re_x \rangle_t$ and $\langle Re_y \rangle_t$, used to distinguish between the Magneto-Plumes and Drifting Plumes regime, against the scaling law derived for N_{MP}. (c) The measured value of τ_{jet}, where values greater than 0 are reserved for the Burst-Jet regime, against the scaling law derived for N_j.

2.5.1 Measured length and velocity scales

It is necessary to measure perpendicular length scales, $l_\perp$, and velocity scales in order to find where in (Ra, Ch) parameter space regime transitions occur using interaction parameter arguments. Fig. 2.10 shows the time average of horizontal spectra where the temperature field has been vertically averaged ($\langle T(m) \rangle_{y,t}$), and demonstrates how $l_\perp$ is measured. An example from each regime is shown. The mode number that corresponds to the spectra peak, m_{peak} is used to calculate $l_\perp = \Gamma/(2m_{peak})$.

Fig. 2.10(a) gives the spectra for a case in the Steady Convection Roll regime where $m_{peak} = 1$ corresponding to $l_\perp = 1$. Fig. 2.10(b) gives an example of a case in the Steady Magneto-Columns regime where $Ch = 10^6, Ra = 10^8$. The vertical black line denotes the horizontal mode number predicted by linear theory, m_c. The spectral peak, m_{peak} occurs close to m_c, which shows that the width of the columns is given by $l_\perp \sim Ch^{-1/6}H$. A similar behavior is found for the Magneto-Plume regime as given in Fig. 2.10(c) at $Ch = 10^5, Ra = 10^9$. The spectral peak, m_{peak} occurs near m_c, again demonstrating that the width of the plumes closely follows $l_\perp \sim Ch^{-1/6}H$.

Fig. 2.10(d) gives the spectra for a case in the Drifting Plumes regime at $Ch = 10^3, Ra = 10^8$. A change in the perpendicular length scale behaviour is observed. There is an increase in m_{peak} relative to m_c. As Ra is increased for a given Ch, the plumes begin to merge and their horizontal width increases. Finally Fig. 2.10(e) shows the spectra for a case in the Burst-Jet regime at $Ch = 10, Ra = 10^8$, where m_{peak} is 1 demonstrating that the flow is dominated by the lowest mode numbers.

Fig. 2.11 shows the measured $l_\perp$ normalized by l_c predicted by theory (using m_c to the nearest integer) in colored contour lines versus (Ra, Ch). The symbols correspond to each case's regime. This figure allows us to carry out a more systematic discussion of $l_\perp$. Cases in the Magneto-Columnar regime have $l_\perp/l_c \approx 1$, which is shown by the blue contour lines. The same holds for the Magneto-Plume regime, where the width of the plumes is also well predicted by linear theory. Based on Fig. 2.11, the following behaviour holds: $l_\perp / l_c \approx 1$, allowing $l_\perp \sim Ch^{-1/6} H$ for the Magneto-Columnar and Magneto-Plume regimes. Fig. 2.11 also shows that $l_\perp / l_c$ begins to increase beyond 1 as plumes merge and increase in horizontal scale in the Drifting Plumes regime Cases in the Magneto-Columnar regime (demarcated by triangles) have $l_\perp / l_c \approx 1$ shown in blue. The same holds for the Magneto-Plume regime (demarcated by crosses), where the width of the spatially localized magnetoconvection plumes can also be predicted by linear theory. Based on Fig. 2.11, the following behaviour holds: $l_\perp / l_c \approx 1$, allowing $l_\perp \sim Ch^{-1/6} H$ for the Magneto-Columnar and Magneto-Plume regimes. In the Drifting Plumes regime, $l_\perp / l_c$ begins to increase beyond 1 as plumes merge and increase in horizontal scale.

Fig. 2.12 shows measurements of the velocity, quantified by the time-averaged vertical and horizontal Reynolds number ($\langle Re_y \rangle_t$ and $\langle Re_x \rangle_t$ respectively) as a function of Ra, Ra_c for different values of Ch, denoted by various colors. The symbols correspond to each case's regime. Fig. 2.12(a) shows the vertical velocity as a function of Ra. In the Steady Convection Roll, Steady Magneto-Columns, and Magneto-Plumes regimes, $\langle Re_y \rangle_t$ grows with increasing Ra. However, for the Drifting Plumes and Burst-Jet regimes, the growth of $\langle Re_y \rangle_t$ with Ra slows, and for some cases there is a depression in $\langle Re_y \rangle_t$ with increasing Ra. This is due to the manifestation of strong zonal flows, which limit convective velocities in the vertical direction.

Fig. 2.12(b) shows $\langle Re_x \rangle_t$ versus Ra, and a different trend is found. Each value of Ch has a slightly lower value of $\langle Re_x \rangle_t$ at a given Ra as increasing magnetic field suppresses flows perpendicular to the field. However, at a fixed value of Ch, $\langle Re_x \rangle_t$ grows monotonically with Ra.

In order to find a scaling law for the velocity in the Steady Magneto-Columns regime, we follow (Yan et al., 2019) and propose that the Joule dissipation acts as an "effective" viscosity. The Joule dissipation, when formulated as a viscous term that damps the flow

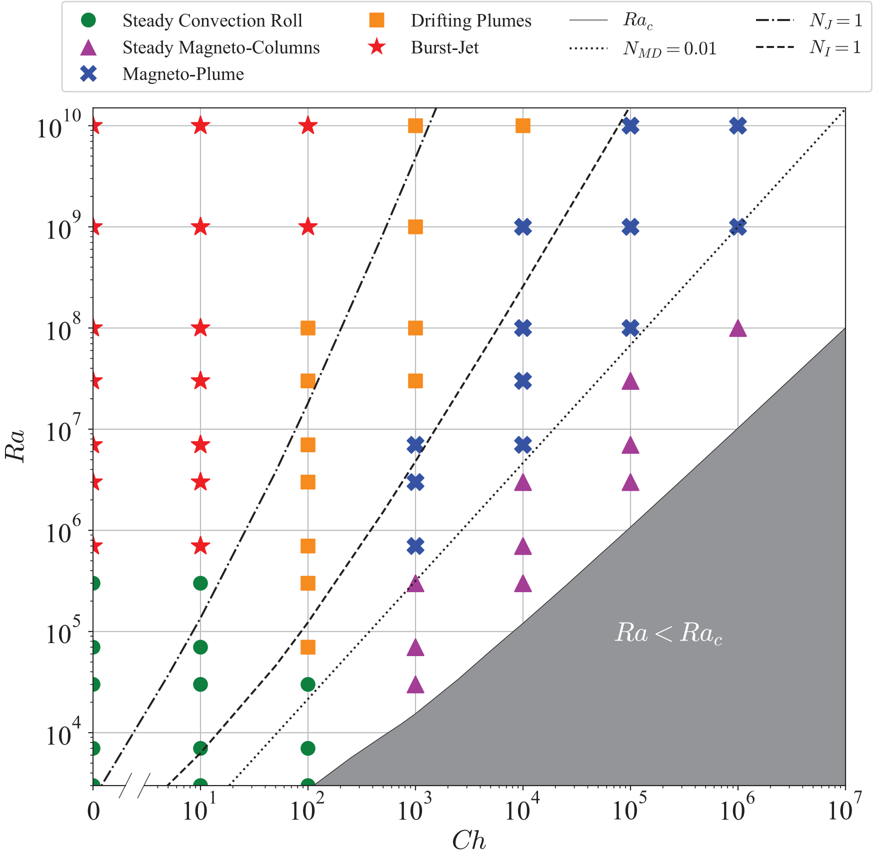

Figure 2.15: The Rayleigh and Chandrasekhar number ranges over which we have found Steady Convection Rolls (green circles), Steady Magneto-Columns (purple triangles), Unsteady to Turbulent Magneto-Plumes (blue crosses), Drifting Magneto-Plumes (orange squares), or Jets with Intermittent Turbulent Convective Bursts (red stars). The solid black line indicates the critical Rayleigh number, and the dotted, dashed, and dash-dot lines give the interaction parameter transitions between the regimes, discussed further in Sec. 2.4.

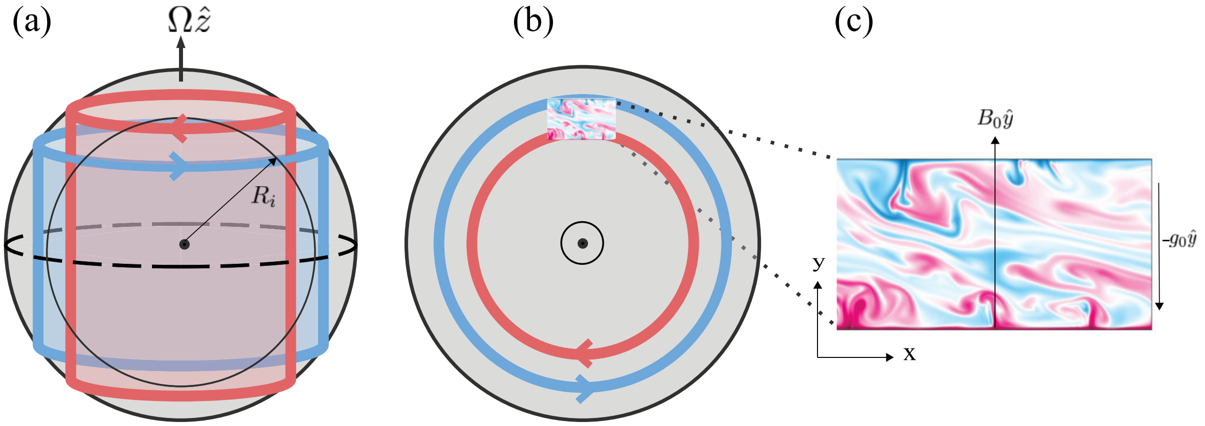

Figure 2.16: (a) Sketch of two, isolated Jovian jets (blue and red). The inner boundary, R_i, depicts the radial truncation depth of the axial jets. (b) Top view of the same two, isolated Jovian jets. (c) Our 2D Cartesian model. A snapshot of temperature is used to visualize the flow field, where blue and red represent cold and hot fluid respectively, is shown. At first-order, the model represents a slice of the planet's atmosphere parallel to the equatorial plane.

speed, leads to a "Joule-Prandtl" number (Pr_j),

$$Pr_j = \frac{\tau_\kappa}{\tau_{j,l}}, \tag{2.95}$$

where $\tau_\kappa = H^2/\kappa$ and $\tau_{j,l}$ is given by Eq. 2.84, where again the parallel length scale has been scaled by H. Substituting these definitions for Pr_j gives,

$$Pr_j = \frac{\sigma B_0^2 H^2}{\rho\kappa}\left(\frac{l_\perp}{H}\right)^2, \tag{2.96}$$

Eq. 2.96 can be simplified using $l_\perp \sim Ch^{-1/6}H$, which holds for the Steady Magneto-Columns regime. This leads to,

$$Pr_j = Ch^{2/3}Pr. \tag{2.97}$$

Using Pr_j as the "effective" Prandtl number for this system yields a velocity scaling law relevant to a flow constrained by the imposed field is given by

$$Re \sim Ra/Pr_j. \tag{2.98}$$

This is similar to a scaling law found by balancing the viscosity and buoyancy terms of Eq. 2.48, which yields $Re \sim Ra/Pr$. In this case, the Joule dissipation, through the Lorentz force, acts like a viscosity damping the flow.

Fig. 2.12(c) gives $\langle Re_y \rangle_t$ versus Ra/Pr_j. We find a good collapse of the cases in the Magneto-Columnar regime (denoted by triangles) using Ra/Pr_j. This agrees with (Yan et al., 2019), who by balancing the Lorentz force with buoyancy, also found $Re \sim Ra/Pr_j$ for convection constrained by an imposed vertical magnetic field. This scaling, $Re \sim Ra/Pr_j$, gives us a behaviour that can be used in conjunction with the perpendicular length scale data for the Steady Magneto-Columns and Magneto-Plume regimes to construct an interaction parameter-based transition between these two regimes.

Fig. 2.12(d) gives $\langle Re_x \rangle_t$ against Ra/Ra_c. The ratio Ra/Ra_c can be thought of as the relative strength of buoyancy given a certain value of Ch. The following collapses the data well (for $Pr = 1$),

$$\langle Re_x \rangle_t = 5.39 \pm 1.17 (Ra/Ra_c)^{0.61 \pm 0.01}. \tag{2.99}$$

This fit matches closely with (Wang et al., 2020), who carried out a study in a set up similar to the one here, namely 2D RBC with free-slip boundary conditions, and found $Re \sim Ra^{0.60}$ for jet-dominated flows (with fixed $Pr = 10$). This scaling law for the velocity will be used for the Drifting Plumes and Burst-Jet regimes, where the horizontal velocity exceeds the vertical velocity.

Table 2.1: Summary of the five regimes and their characteristics. Each column gives the regime name, the ratio of horizontal to vertical velocities, the variance of the vertical velocity, the value of τ_j (the average time spent in the jet phase), and the scaling laws used for the perpendicular length scale and velocity $(l_\perp, Re)$ when building interaction parameter transition lines between the regimes as discussed in Sec. 2.5.2.

Regime Name	Horizontal to Vertical Velocity Ratio	$var(Re_y)$	τ_j	$l_\perp \sim$	$Re \sim$
Steady Convection Roll	$\langle Re_x\rangle_t \approx \langle Re_y\rangle_t$	0	0	1	
Steady Magneto-Columns	$\langle Re_x\rangle_t \leq \langle Re_y\rangle_t$	0	0	$Ch^{-1/6}$	Ra/Pr_j
Magneto-Plumes	$\langle Re_x\rangle_t \leq \langle Re_y\rangle_t$	Greater than 0	0	$Ch^{-1/6}$	
Drifting Plumes	$\langle Re_x\rangle_t > \langle Re_y\rangle_t$	Greater than 0	0		$(Ra/Ra_c)^{0.61}$
Burst-Jet	$\langle Re_x\rangle_t > \langle Re_y\rangle_t$	Greater than 0	Greater than 0	Γ	$(Ra/Ra_c)^{0.61}$

In the following section, we use the trends found in our data along with the interaction parameter definitions given in Sec. 2.4 to construct three interaction parameter-based transition lines which can be used to predict where one regime transitions to the next in (Ra, Ch) space.

2.5.2 Transition Laws Based on Interaction Parameter Formulations

The two end-member interaction parameter formulations, 2.88 for jet-dominated flows and 2.85 flows where gradients parallel to the applied field have been surpressed, can be utilized to predict where in parameter space regime transitions may occur. Both versions of the interaction parameter depend on the flow's dominant perpendicular length scale and leading order velocity scale, which were measured and discussed in Sec. 2.5.1. The resulting transition laws are given here.

2.5.2.1 Predicted transition lines

We use the trends found in our data along with the interaction parameter definitions given in Sec. 2.4 to construct three interaction parameter-based transition lines which can be used to predict where one regime transitions to the next in (Ra, Ch) space. Table 2.1 gives a summary of the five regimes, their main characteristics, and the length and velocity scalings that will be utilized here.

The first transition line separates the Steady Magneto-Columns regime from the Magneto-Plumes regime, which are both "magnetically dominated" flows in which gradients parallel to the applied field are limited. In both regimes, the data revealed $l_\perp \sim Ch^{-1/6}H$. To find where the Magneto-Plumes regime transitions to the Steady Magneto-Columns regime, we note that only in the latter, inertial effects are neglected to yield the velocity scale $Re \sim Ra/Pr_j$. The Magneto-Plumes regime then transitions to the Steady Magneto-Columns regime along an interaction parameter line given by Eq. 2.85 using $Re \sim Ra/Pr_j$, in addition to

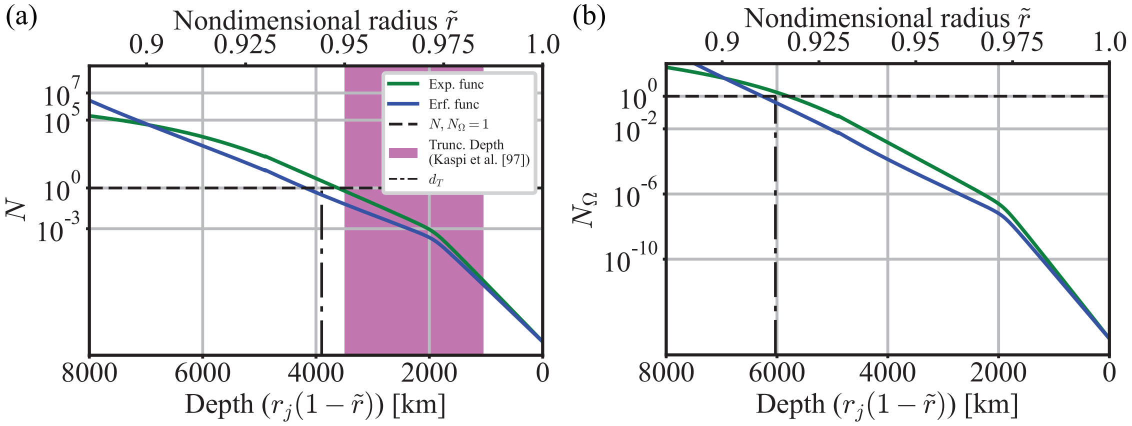

Figure 2.17: (a) Value of the Jovian Elsasser number Λ with nondimensional radius given by 2.118. (b) Value of the interaction parameter based on the Elsasser number, $N_{Jov,\Lambda}$ given by **??**. The black dashed line indicates where $N_{Jov,\Lambda} = 1$. The purple box indicates the range of truncation depths from the Juno mission (Kaspi et al., 2020) (c) Estimated zonal flow decay with nondimensional radius for two functions. Green is based on (Kaspi et al., 2020), with $u_{zonal}(r) = Ae^{r/r_j\ H_0}$ and A a constant to fix the cloud level zonal-flow magnitude to 125 m/s. Blue is an error function which yields a cloud level zonal-flow magnitude of 125 m/s and decays sharply between 1.0 and 0.90 r/r_j. (d) Estimated value of Jupiter's interaction parameter, N_{Jov} using the zonal flow given in (c), with green and blue corresponding to the exponential and error functions respectively. The black dashed line indicates where $N_{Jov} = 1$. The purple box indicates the range of truncation depths from the Juno mission (Kaspi et al., 2020).

$l_\perp \sim Ch^{-1/6}H$. This substitution yields

$$N_{MD} = \frac{Ch}{Re}\left(\frac{l_\perp}{H}\right)^3 \sim \frac{Ch^{7/6}Pr}{Ra}. \tag{2.100}$$

The second transition is between the two "intermediate" regimes (Magneto-Plumes and Drifting Plumes) rather than the end-member flows (Steady Magneto-Columns and Burst-Jet). In the Magneto-Plumes regime, the structures have a perpendicular length scale that, as previously stated follows $l_\perp \sim Ch^{-1/6}H$. The distinguishing characteristic between the these two regimes is that the horizontal velocity dominates the vertical velocity in the Drifting Plumes regime, as defined in Sec. 2.5. Therefore, the crossover to the Drifting Plumes regime from the Magneto-Plumes regime will occur once the velocity follows $Re \sim (Ra/Ra_c)^{0.61}$ as found in Sec. 2.5.1. Using Eq. 2.85

$$N_I = \frac{Ch}{Re}\left(\frac{l_\perp}{H}\right)^3 \sim \frac{Ch^{1/2}Pr}{(Ra/Ra_c)^{0.61}}. \tag{2.101}$$

The final transition is between the Drifting Plumes regime and Burst-Jet regime, which is characterized by strong, domain-filling zonal flows, or jets (J). In such flows, $l_\perp/H \sim \Gamma$, though the velocity scale continues to follow $Re \sim (Ra/Ra_c)^{0.61}$. For this transition line, Eq. 2.88 is used, since the system is not constrained by the magnetic field and strong vertical shears exist in the flow. The transition to the jet regime is

$$N_J = \frac{Ch}{Re}\left(\frac{l_\perp}{H}\right) \sim \frac{Ch\ Pr\ \Gamma}{(Ra/Ra_c)^{0.61}}. \tag{2.102}$$

Fig. 2.14(a) gives N_{MD} against $var(Re_y)$ for cases only in these two regimes, where values greater than zero are used to separate the Steady Magneto-Columns to the Magneto-Plume regime. This transition occurs at $N_{MD} \approx 0.01$. Fig. 2.14(b) shows N_I against $\langle Re_x\rangle_t/\langle Re_y\rangle_t$, the ratio that separates the two intermediate regimes (the Magneto-Plume and the Drifting Plumes) from one another with a transition occurring at $N_I \approx 1$. Fig. 2.14(c) shows N_J against τ_{jet}, where values greater than zero are used to parse the Drifting Plumes to the Burst-Jet regime. There is a reasonable collapse of the data at $N_J \approx 0.1 - 1$.

Fig. 2.15 outlines the values of (Ra, Ch) over which we have run simulations. The colors and symbols correspond to regime classifications and the three lines, (dotted, dashed, dash-dot) give approximate regime transitions, based on Eq. 2.100, Eq. 2.101, and Eq. 2.102. These transition lines provide adequate estimates for where regime transitions occur.

2.6 Geophysical Implications

The quasi-steady azimuthal component of the vorticity equation in cylindrical coordinates $(\hat{\boldsymbol{s}}, \hat{\boldsymbol{z}}, \hat{\boldsymbol{\phi}})$ controlling the dynamics in the bulk of Jupiter's outer molecular envelope is (Jones, 2000; Sreenivasan and Jones, 2005; Aurnou et al., 2003)

$$\left([\boldsymbol{u} \cdot \boldsymbol{\nabla} \boldsymbol{\omega}]_{\phi} + 2\Omega \frac{\partial u_{\phi}}{\partial z}\right) \simeq \alpha g \frac{\partial T}{\partial s}, \tag{2.103}$$

where we have simplistically adopted the Boussinesq approximation to treat the density (Stanley and Glatzmaier, 2010; Gastine and Wicht, 2012). Eq. 2.103, neglecting the first term on the left hand side, is known as thermal wind balance (Showman et al., 2006; Zhang et al., 2015; Kong et al., 2018). The left hand side of Eq. 2.103 are the inertial terms in the system, where the first represents advection and the second represents vortex stretching. We can take the ratio of these terms to one another, which gives

$$\frac{[\boldsymbol{u} \cdot \boldsymbol{\nabla} \boldsymbol{\omega}]_{\phi}}{2\Omega \frac{\partial u_{\phi}}{\partial z}} \sim \frac{U}{2\Omega \mathcal{L}} = Ro, \tag{2.104}$$

where Ro is known as the Rossby number, $\mathcal{L}$ is a characteristic length scale, U is a characteristic velocity scale, and Ω is the planetary rotation rate. We can estimate Ro for Jupiter's molecular envelope jets using a typical jet velocity of $U = 50$ m/s, a large scale jet width of $\mathcal{L} = 10^4$ km, and planetary rotation rate of $\Omega = 1.74 \times 10^{-4}$ 1/s, which gives (Heimpel et al., 2005)

$$Ro = \frac{U}{2\Omega \mathcal{L}} \sim 0.01 \ll 1. \tag{2.105}$$

Furthermore, strong convective turbulence could homogenize the large-scale temperature anomalies such that $\partial T/\partial s$ is small. For the low Rossby jets, this implies that the velocity field may vary weakly along the axial coordinate such that $\partial u_\phi/\partial z$ in Eq. 2.103 is also small (Liu et al., 2013).

Jupiter's electrical conductivity increases with radius, possibly leading to a larger Lorentz force at the base of the jets compared to the molecular envelope. Then, the hydrodynamic thermal wind balance is replaced by the thermomagnetic wind balance (Christensen et al., 2020)

$$\Big([\boldsymbol{u}\cdot\boldsymbol{\nabla}\boldsymbol{\omega}]_\phi + 2\Omega\frac{\partial u_\phi}{\partial z}\Big) \simeq \alpha g\frac{\partial T}{\partial s} + \frac{1}{\rho_0}\Big[\boldsymbol{\nabla}\times\Big(\boldsymbol{J}\times\boldsymbol{B}\Big)\Big]_\phi. \tag{2.106}$$

In the limit of strong thermal mixing, this simplifies to

$$\Big([\boldsymbol{u}\cdot\boldsymbol{\nabla}\boldsymbol{\omega}]_\phi + 2\Omega\frac{\partial u_\phi}{\partial z}\Big) \approx \frac{1}{\rho_0}\Big[\boldsymbol{\nabla}\times\Big(\boldsymbol{J}\times\boldsymbol{B}\Big)\Big]_\phi. \tag{2.107}$$

Further, by assuming $Rm \leq 1$ at the base of the jets (Heimpel and Gómez Pérez, 2011), we can use $\boldsymbol{J} = \sigma(\boldsymbol{u}\times\boldsymbol{B})$ to recast this expression as

$$\Big([\boldsymbol{u}\cdot\boldsymbol{\nabla}\boldsymbol{\omega}]_\phi + 2\Omega\frac{\partial u_\phi}{\partial z}\Big) \simeq \frac{1}{\rho_0}\Big[\boldsymbol{\nabla}\times\Big(\sigma\boldsymbol{u}\times\boldsymbol{B}\times\boldsymbol{B}\Big)\Big]_\phi. \tag{2.108}$$

The right hand side of Eq. 2.108 can be expanded, leading to

$$\frac{1}{\rho_0}\Big[\boldsymbol{\nabla}\times\Big(\sigma\boldsymbol{u}\times\boldsymbol{B}\times\boldsymbol{B}\Big)\Big]_\phi = \frac{1}{\rho_0}\Big[\boldsymbol{\nabla}\times\Big(\Big(\sigma\boldsymbol{u}\cdot\boldsymbol{B}\Big)\boldsymbol{B} - (\boldsymbol{B}\cdot\boldsymbol{B})\Big(\sigma\boldsymbol{u}\Big)\Big)\Big]_\phi. \tag{2.109}$$

Eq. 2.109 can be simplified by allowing $\boldsymbol{u} = \boldsymbol{u}_\perp + \boldsymbol{u}_\parallel$, where $\perp, \parallel$ denote directions relative to the magnetic field $\boldsymbol{B}$. Then Eq. 2.108 becomes

$$\begin{aligned}\Big([\boldsymbol{u}\cdot\boldsymbol{\nabla}\boldsymbol{\omega}]_\phi + 2\Omega\frac{\partial u_\phi}{\partial z}\Big) \simeq \frac{-|B|^2|}{\rho_0}\Big[\sigma(\boldsymbol{\nabla}\times\boldsymbol{u}_\perp) + {} \\ (\nabla\sigma)\times\boldsymbol{u}_\perp\Big]_\phi.\end{aligned} \tag{2.110}$$

We reduce Eq. 2.110 further by allowing $\boldsymbol{u}_\perp = u_s\hat{\boldsymbol{s}} + u_\phi\hat{\boldsymbol{\phi}} + u_z\hat{\boldsymbol{z}}$. This gives

$$\Big([\boldsymbol{u}\cdot\boldsymbol{\nabla}\boldsymbol{\omega}]_\phi + 2\Omega\frac{\partial u_\phi}{\partial z}\Big) \simeq -|B|^2\Big[\frac{\sigma}{\rho}\Big(\frac{\partial u_s}{\partial z} - \frac{\partial u_z}{\partial s}\Big) + \frac{1}{\rho}\Big(\frac{\partial\sigma}{\partial z}u_s - u_z\frac{\partial\sigma}{\partial s}\Big)\Big]. \tag{2.111}$$

Noting that velocity field varies weakly along the axial coordinate for low Rossby flows, and σ only varies in radius gives

$$\Big([\boldsymbol{u}\cdot\boldsymbol{\nabla}\boldsymbol{\omega}]_\phi + 2\Omega\frac{\partial u_\phi}{\partial z}\Big) \simeq \frac{-|B|^2|}{\rho_0}\Big[\sigma\Big(\frac{\partial u_z}{\partial s}\Big) + \Big(u_z\frac{\partial\sigma}{\partial s}\Big)\Big]. \tag{2.112}$$

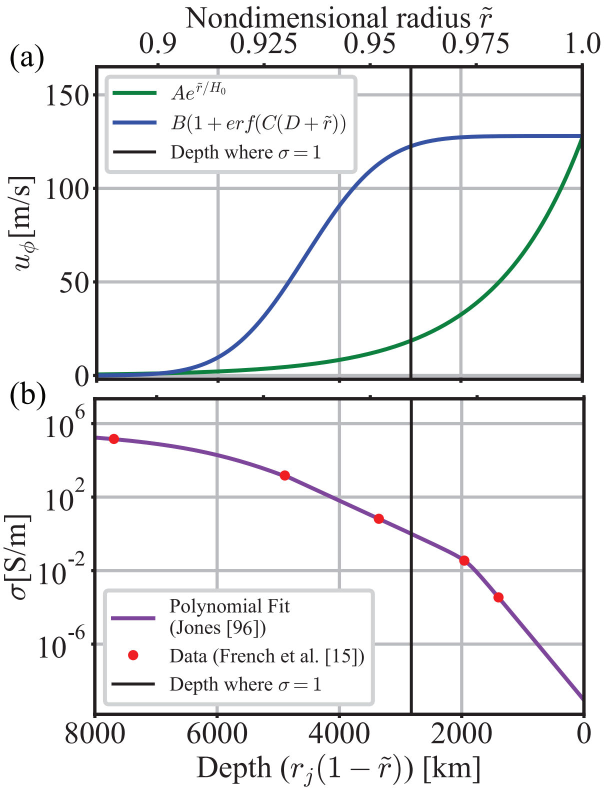

Figure 2.18: (a) Estimated zonal flow decay with nondimensional radius (top axis) or depth from the surface (bottom axis) for two functions. Green is based on (Kaspi et al., 2020), with $u_\phi(\tilde{r}) = Ae^{\tilde{r}/H_0}$ and A a constant to fix the cloud level zonal-flow magnitude to 125 m/s. Blue is an error function which yields a cloud level zonal-flow magnitude of 125 m/s and decays sharply once $\sigma = 1$ demarcated by a black line. (b) Electrical conductivity with nondimensional radius (top axis) or depth from the surface (bottom axis). The red points show data from (French et al., 2012) and the purple line shows the polynomial fit to these points carried out by (Jones, 2014). The black line gives the depth at which $\sigma = 1$.

We can scale both terms on the right hand side of Eq. 2.112, and from left to right they are

$$\frac{B_0^2 \sigma u_z}{\rho_0 \mathcal{L}_{jet}} ; \frac{B_0^2 \sigma u_z}{\rho_0 \mathcal{L}_{\sigma}} \tag{2.113}$$

where B_0 is a characteristic magnetic field strength in the semiconducting region, u_z is a characteristic meridional velocity scale, $\mathcal{L}_{jet}$ is a characteristic jet scale, and

$$\mathcal{L}_{\sigma} = \frac{1}{\sigma} \left| \frac{\partial \sigma}{\partial s} \right|^{-1} \tag{2.114}$$

is an electrical conductivity scale height. This can be calculated using the results of (French et al., 2012) and (Jones, 2014). The terms in Eq. 2.113 only differ by the length scales in their denominators. Comparing the characteristic values $\mathcal{L}_{\sigma} \approx 350$ km and $\mathcal{L}_{jet} \approx 10,000$ km we find

$$\mathcal{L}_{\sigma} \ll \mathcal{L}_{jet}. \tag{2.115}$$

The second term on the right hand side of Eq. 2.112, controlled by the planet's radially increasing electrical conductivity, is the largest term, and we are left with

$$\left([\boldsymbol{u} \cdot \boldsymbol{\nabla} \boldsymbol{\omega}]_{\phi} + 2\Omega \frac{\partial u_{\phi}}{\partial z} \right) \simeq \frac{|B|^2}{\rho_0} \left(u_z \frac{\partial \sigma}{\partial s} \right). \tag{2.116}$$

We can balance the two inertial terms with the Lorentz term in Eq. 2.116 to construct two interaction parameter functions. For the first, we take the ratio of the Lorentz to the advection term in Eq. 2.108 and note that $\omega_{\phi} \sim u_z / \mathcal{L}_{jet}$ to arrive at an interaction parameter

$$N = \frac{B_0^2 \sigma(\tilde{r}) \mathcal{L}_{jet}^2}{u_{\phi}(\tilde{r}) \rho_0 \, \mathcal{L}_{\sigma}}, \tag{2.117}$$

where $\tilde{r} = r/r_j$ is radial position normalized by Jupiter radius $r_j = 69,894$ km, ρ_0 is the mean density averaged over $0.90 < \tilde{r} < 1.0$, and $\sigma(\tilde{r})$ is the electrical conductivity as a function of nondimensional radial position.

For the second interaction parameter, we take the ratio of the Lorentz to the Coriolis term in Eq. 2.116, which gives a Coriolis based interaction parameter (also known as the

Elsasser number, Λ) (Soderlund et al., 2012; King and Aurnou, 2015; Calkins et al., 2015; Aurnou and King, 2017; Orvedahl et al., 2021)

$$N_\Omega = \Lambda = \frac{B_0^2 \sigma(\tilde{r})}{2\rho_0 \ \Omega} \Big(\frac{u_z}{u_\phi}\Big) \Big(\frac{\mathcal{L}_{jet}}{\mathcal{L}_\sigma}\Big). \tag{2.118}$$

Though our simple model differs greatly from the fully 3D, anelastic, spherical Jovian system, based on Eq. 2.103 the low Rossby jets may extend into the molecular interior with little variation in the direction of the axis of rotation. Fig. 2.16(a, b, c) shows a schematic of one pair of alternating prograde-retrograde jets, a top view of the same system, and a snapshot from our model to demonstrate the location in the low Rossby Jovian atmosphere that our model may represent. Thus, we choose to extrapolate the transitions found in our 2D model, and naively assume that magnetodamping may slow the jets when the Lorentz force is greater than inertia, or the depth at which N and N_Ω exceed 1.

In order to calculate N and N_Ω, we calculate values for $\sigma(\tilde{r}), \rho(\tilde{r}), \mathcal{L}_\sigma$. A radial profile of electrical conductivity σ is found by employing the results of (French et al., 2012) and (Jones, 2014). In particular, (French et al., 2012) carried out ab initio simulations to determine the basic thermodynamic and transport properties of hydrogen–helium–water mixtures for the extreme conditions along Jupiter's adiabat. (Jones, 2014) then fit these data points using a hyperbolic fitting formula defined by

$$\tilde{\eta} = exp(a + \sqrt{a^2 + b}) \tag{2.119}$$

where $\tilde{\eta} = 1/4\pi \times 10^{-7}\sigma$ and a and b are coefficients that depend on nondimensional radial position $\tilde{r}$. The values of a and b are further given by

$$a = \frac{1}{2}[(g_1 + g_3)\tilde{r} - g_2 - g_4], \tag{2.120}$$

and

$$b = (g_1\tilde{r} - g_2)(g_3\tilde{r} - g_4) - g_5, \tag{2.121}$$

where g_1, g_2, g_3, g_4, g_5 are constants tabulated in (Jones, 2014) (Table 2). We use these constants to calculate Eq. 2.120 - 2.121, which we then substitute into Eq. 2.119 to find the magnetic diffusivity as a function of radial position. Finally, we use $\tilde{\eta} = 1/4\pi \times 10^{-7}\sigma$ to calculate $\sigma(\tilde{r})$.

A similar process is carried out to find a radial profile of ρ. Again, we rely on the results of ab initio results of (French et al., 2012) which were fit by (Jones, 2014) using a polynomial fitting formula. The logarithm of the polynomial fitting formula is defined by

$$log(\rho) = \frac{r_1}{4}\tilde{r}^4 + \frac{r_2}{3}\tilde{r}^3 + \frac{r_3}{2}\tilde{r}^2 + r_4\tilde{r} + \\ f_2\ log(e_1 - \tilde{r}) + \frac{f_2 - f_1}{2}\Big((\tilde{r} - e_2)^2 + e_3^3\Big) + f_3\ arctan\Big(\frac{\tilde{r} - e_2}{e_2}\Big) + r_5. \quad (2.122)$$

where the constant of integration is determined by the requirement $r_5 = 4.42 \times 10^3$ kg m^{-3} at the core boundary. Furthermore, the coefficients f_2 and f_3 are calculated using

$$f_2 = f_1 \frac{(d_1 - e_1)^2 + d_2^2}{(e_1 - e_2)^2 + e_3^2}, \quad (2.123)$$

$$f_3 = \frac{2f_1 d_1 + e_1(f_2 - f_1) - e_2(f_2 + f_1)}{e_3}, \quad (2.124)$$

where $f_1, d_1, d_2 e_1, e_2, e_3$ are constants tabulated in (Jones, 2014) (Table 2). We calculate Eq. 2.122 by first calculating f_2 and f_3. Then we take the exponential of $log(\rho)$ fo find $\rho(\tilde{r})$.

To find B_0 in the semi-conducting region, we employ potential field theory which allows us to map the surface magnetic field into planet's interior until the dynamo generating region. We first construct a full map of the magnetic field using the most recent set of Schmidt coefficients as measured by Juno and tabulated in (Connerney et al., 2018). The planetary magnetic field, $B(r, \theta, \phi)$ can be derived from the gradient of a scalar potential function, V, where

$$V = r_j \sum_{n1}^{n_{max}} \left(\frac{r_j}{d}\right)^{n+1} (P_n^m cos(\theta)[g_n^m cos(m\phi) + h_n^m sin(m\phi)]) \quad (2.125)$$

where d is the radial depth, θ is the colatitude, ϕ is the longitude, $P_n^m cos(\theta)$ are the Schmidt quasi-normalized Associated Legendre functions of degree n (up to n_{max}) and order m. Here, g_n^m and h_n^m are the Schmidt coefficients. Fig. 2.19 gives a contour plot of Jupiter's magnetic field magnitude in Gauss and radial location $r = 0.98r_j$. We estimate B_0 then by taking the

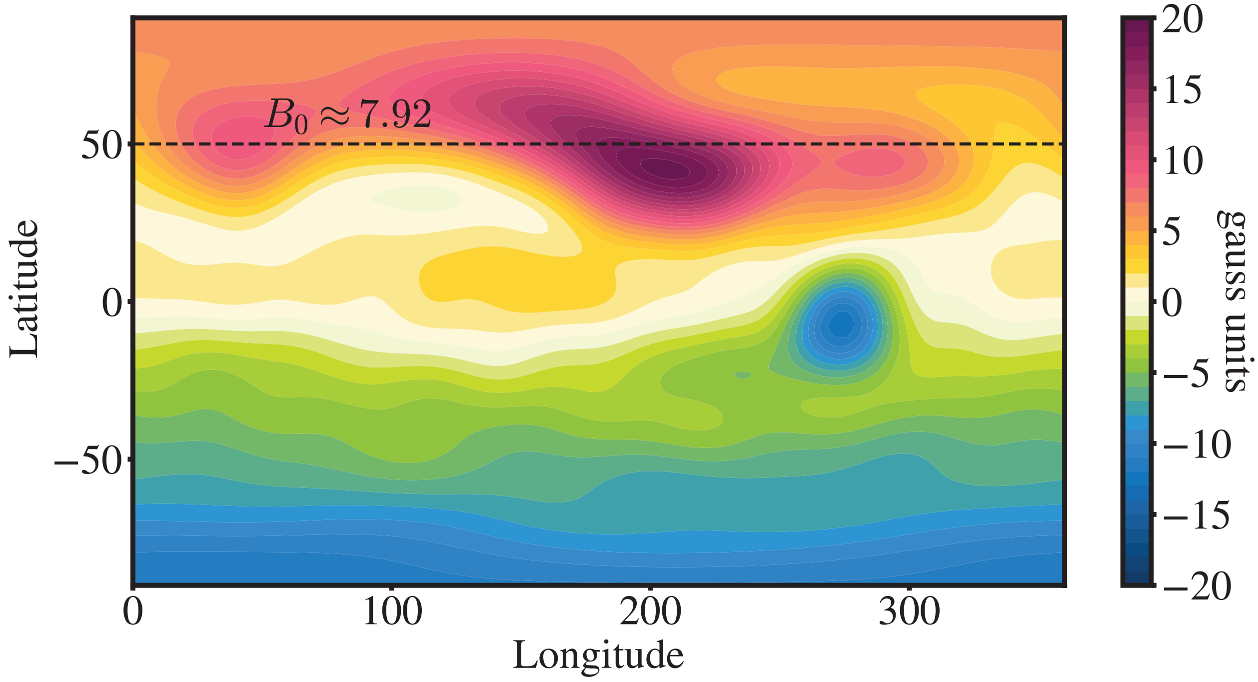

Figure 2.19: Contours of the Jovian magnetic field (Gauss) at 0.98 r_j using the vector magnetic field observations from the Juno spacecraft during its fine nine orbits (Connerney et al., 2018). The horizontal dashed line denotes a latitude of 50 degrees, over which the average B_0 is found to estimate the value of Jupiter's interaction parameter as a function of depth and radial location.

average of the field at 50 degrees latitude, which yields a value of ≈ 7.92 Gauss. Finally, the meridional velocity scale $u_z \approx 1$ m/s is found using Cassini spacecraft observation data (Galperin et al., 2014; Maffei et al., 2019).

We use two different functions for the zonal velocity, $u_\phi(\tilde{r})$. For the first, we employ the simple exponential decay model from (Kaspi et al., 2020)

$$u_\phi(\tilde{r}) = Ae^{\tilde{r}/H_0}, \tag{2.126}$$

where A is a constant fixed to yield a sensible cloud-level zonal flow of 125 m/s (Vasavada and Showman, 2005), and $H_0 = H/r_j$ is the e-folding depth. According to (Kaspi et al., 2020), the e-folding depth that yields a best fit to the Juno odd gravity harmonic data is $H = 1471$ km. The green curve in Fig. 2.18(a) gives this constructed zonal flow profile in the semi-conducting region from $\tilde{r}$ ranging from about 0.90 ($8,000$ km in depth) to 1.0.

However, the exact shape of the zonal flow decay remains ambiguous. We construct an additional zonal flow profile where $u_{zonal}(\tilde{r})$ only decays after the planet's electrical conductivity exceeds 1 S/m. The profile meets the criteria that in the highly conducting region of Jupiter with electrical conductivity greater than 1000 S/m, the zonal flow is likely on the order of 1 cm/s or less (Yu et al., 2010; Ridley and Holme, 2016; Cao and Stevenson, 2017) and is defined by

$$u_\phi(\tilde{r}) = B\ (1 + erf(C(D + \tilde{r}))) \tag{2.127}$$

where $B = 64.0, C = 49.1, D = -0.946$ yield a cloud-level zonal flow on the order of 125 m/s. The blue curve in Fig. 2.18(a) shows this profile. Fig. 2.18(b) shows Jupiter's estimated electrical conductivity with radius, and we mark the depth at which $\sigma = 1$ with a solid black line.

Fig. 2.17(a) gives N against nondimensional radius (top axis) and depth from the surface (bottom axis) using these approximations. A value of $N = 1$ (black dashed line) corresponds to a depth at which the jet truncation process may commence at about $d_T = 3600; 4200$ km for the exponential and error velocity functions respectively (black dash dot line, the average between the two is shown).

Fig. 2.17(b) gives N_Ω against nondimensional radius (top axis) and depth from the surface (bottom axis). A value of $N_\Omega = 1$ (black dashed line) is not reached until a depth of about $d_T = 6000; 6300$ km for the exponential and error functions respectively. Recent studies based on Juno measurements of the odd gravity harmonics have constrained the zonal flow depth to about 3000 km (Kaspi et al., 2018, 2020).

Extrapolating our 2D results suggests that Lorentz force likely cannot soley brake the jets on Jupiter, and additional mechanisms are needed to fully truncate them (Liu et al., 2008; Heimpel and Aurnou, 2012; Cao and Stevenson, 2017). For instance (Christensen et al., 2020) carried out axisymmetric shell models that included both electromagnetic drag and a stably stratified layer extending upward into the region of low electrical conductivity, which may exist on the Gas Giants (Showman et al., 2006; Schöttler and Redmer, 2018; Gastine and Wicht, 2021). They found that without this stable layer, the Lorentz force could not truncate the jets. Thus, extrapolation of our 2D modeling results suggests that the exact braking process of Jovian jets should include mechanisms beyond electromagnetic damping.

2.7 Code Development

To perform the DNS, we use the pseudo-spectral solver developed primarily by myself as a portion of my thesis. This code, written in Fortan, numerically integrates the governing equations at each time step with the following process (Glatzmaier, 2014):

1. Finds the time derivatives of of vorticity and temperature based on 2.62 and 2.63
2. Updates the temperature field and vorticity field in time
3. Solves the Poisson equation for the streamfunction based on the vorticity field
4. Uses the updated temperature, vorticity, and velocity fields to calculate output quantities

5. Writes data out

6. Sets the new time step and repeats process.

Appendix E gives the Fortran code for the main loop of this solver and specifics the steps above. For the spatial discretization, the code utilizes m Fourier modes in the periodic x direction where, for example, the temperature (T) can be written as

$$T(x, y, t) = \sum_{m=1}^{M} T_m(y, t) cos(m\pi x/\Gamma) \tag{2.128}$$

where m is the horizontal mode number, M is the total number of horizontal modes, and Γ is the aspect ratio of the box (length/height). The resulting equations are solved using a second-order accurate finite difference scheme in y. Finite-difference methods are obtained by utilizing a Taylor Series expansion of a variable based on the powers of the grid spacing. Under the second-order accurate finite difference scheme, the first derivative of a function such as temperature, T, is

$$\left(\frac{\partial T}{\partial y}\right)_k = \frac{T_{k+1} - T_{k-1}}{2\Delta y}, \tag{2.129}$$

and the second derivative can be computed using

$$\left(\frac{\partial^2 T}{\partial y^2}\right)_k = \frac{(T_{k+1} - 2T_k + T_{k-1})}{2\Delta y^2}, \tag{2.130}$$

where k is the index in the vertical direction and ranges from 1 to n_y. The spectral-transform method is applied to obtain the spectral coefficients for the nonlinear terms in equations 2.62 and 2.63. FFTs, with the FFTW package, are used to make the transform between physical and spectral space. The solution is dealised at each time step by restricting the number of Fourier modes to one third of the number of grid points in x.

The grid-spacing in y for the finite-difference method is non-uniform with Chebyshev mapping for finer resolution at the top and bottom boundaries defined by,

$$y_k = \frac{1}{2}\Big(1 - cos(\pi q_k)\Big) \text{ for } k = 1, ...n_y, \tag{2.131}$$

where $0 \leq q \leq 1$ and n_y is the total number of grid points in y. To solve the Poisson equation for the streamfunction based on the vorticity, the tridiagonal nature of the resulting matrix is exploited. A tridiagonal solver based on the Thomas algorithm is applied for each Fourier mode. An explicit, second-order Adams-Bashforth (AB2) scheme is used for the time integration. AB2 is easy to implement and efficient, since at teach time step the time derivatives are required only for the current and previous time steps. The equation to evolve a variable such as temperature, T, can be written as

$$T_{t+\Delta t} = T_t + \Delta t/2(3G_t - G_{t-\Delta t}), \tag{2.132}$$

where G represents $\partial T/\partial t$ at a time $t + \Delta t/2$, and where Δt is the computational time step. The time step is restricted by the stability constraints on linear diffusion

$$\Delta t < \frac{(\Delta y)^2}{4}, \tag{2.133}$$

and nonlinear advection,

$$\Delta t < \frac{\Delta y}{|u_y|_{max}}, \tag{2.134}$$

where equation 2.134 should also be considered for the x direction (Glatzmaier, 2014).

The parallelization, making use of Message Passing Interface (MPI), is implemented by decomposing the spatial domain in the vertical direction to solve the temperature and vorticity equations. For the Poisson equation, the parallelization is transposed to the Fourier modes in the horizontal direction, which allows the Thomas algorithm to remain the method for the tridiagonal solver.

The datasets produced are stored in a series of netCDF-4/HDF5 snapshot files of the flow fields, which is particular useful for storing multidimensional scientific data. We also take advantage of parallel I/O access to these files. In addition, checkpoint files are typically written a tenth of the frequency of the snapshot files, where each checkpoint file overwrites the previous file to minimize storage requirements. Python-based analysis scripts produce the necessary images and calculations from the snapshot files after run-time. If additional data is required from the run, the checkpoint file can be used to restart the simulation. Further, we output several ASCII files that are small in comparison to the snapshot files.

2.7.1 Validating the Code

The code developed for this study was validated throughout the writing process at each major development. This allowed us to increase the physical complexity of the system while ensuring that the previous iteration of the code was accurate. First, we developed the linear, hydrodynamic version of the solver and compared the results to theoretical predictions derived from linear stability analysis. Then, we added the electromagnetic term and again, compared the results of the code to theoretical predictions derived from magnetohydrodynamic linear stability analysis. Next, we added the nonlinear terms and carried out full models of 2D Rayleigh-Bénard convection and validated the results to similar studies in the literature. Finally, we included the electromagnetic term for a fully nonlinear magnotoconvection model, and benchmarked the results to additional studies in the literature.

2.7.1.1 Benchmarking to Linear Theory

The first and simplest step of the code development process is to solve the linearized governing equations for hydrodynamic Rayleigh-Bénard convection. The goal of carrying out this linear stability analysis is to find an analytical expression for the critical value of Ra, or buoyancy forcing, such that the solution will be convectively unstable and grow in time. Formally, the process is carried out by dropping the nonlinear terms in the governing equations and using Fourier expansion to represent all variables of interest, namely the temperature (T), vorticity, and stream function ψ.

Expanding these variables with Fourier analysis in the horizontal direction (and noting that in our 2D case, the vorticity only has one component in the $\hat{\boldsymbol{y}}$-direction) gives

$$T(x,y,t) = \sum_{m=1}^{M} T_m(y,t) cos(m\pi x/\Gamma) \tag{2.135}$$

$$\omega(x,y,t) = \sum_{m=1}^{M} \omega(y,t) sin(m\pi x/\Gamma) \tag{2.136}$$

$$\psi(x,y,t) = \sum_{m=1}^{M} \psi(y,t) sin(m\pi x/\Gamma). \tag{2.137}$$

where m is the horizontal Fourier mode, M is the total number of horizontal Fourier modes, and the aspect ratio of the domain is given by

$$\Gamma = \frac{Length}{Height} = \frac{L}{H}. \tag{2.138}$$

The sine and cosine functions in Eq. 2.135-2.137 are chosen to satisfy the sidewall boundary conditions.

We can substitute these into Eq. 2.62-2.63 and linearize the equations (but neglecting the electromagnetic terms), which gives a set of equations for each Fourier mode m

$$\frac{\partial T_m}{\partial t} = \frac{m\pi}{\Gamma}\psi_m + \Big(\frac{1}{\sqrt{Ra\ Pr}}\Big)\Big(\frac{\partial^2 T_m}{\partial y^2} - \Big(\frac{m\pi}{\Gamma}\Big)^2 T_m\Big) \tag{2.139}$$

$$\frac{\partial \omega_m}{\partial t} = \frac{m\pi}{\Gamma}T_n + \sqrt{\frac{Pr}{Ra}}\Big(\frac{\partial^2 \omega_m}{\partial y^2} - \Big(\frac{m\pi}{\Gamma}\Big)^2 \omega_m\Big) \tag{2.140}$$

$$\omega_m = -\Big(\frac{\partial^2 \psi_m}{\partial y^2} - \Big(\frac{m\pi}{\Gamma}\Big)^2 \psi_m\Big). \tag{2.141}$$

For the analytical solution, we expand the temperature, vorticity, and streamfunction in the vertical direction. Taking note that all variables vanish at the top and bottom boundaries, we find

$$T_n(y,t) = \sum_{n=1}^{N} T_{mn}(t) sin(n\pi y) \tag{2.142}$$

$$\omega_n(y,t) = \sum_{n}^{N} \omega_{mn}(t) sin(n\pi y) \tag{2.143}$$

$$\psi_n(y,t) = \sum_{n=1}^{N} \psi_{mn}(t) sin(n\pi y). \tag{2.144}$$

where n is the vertical mode number and N is the total number of vertical Fourier modes. Using the function $sin(n\pi y)$ for the Fourier expansion in the vertical direction is chosen because it satisfies the vertical boundary conditions at $y = 0, 1$ of the variables of interest.

Substituting the vertical Fourier expansions into Eq. 2.139-2.141 and noting that (1) $\partial/\partial t = 0$ for the stability problem, and (2) the $sin(n\pi y)$ factor exists in each term so it drops off gives

$$0 = \frac{m\pi}{\Gamma}\psi_n + \Big(\frac{1}{\sqrt{Ra\ Pr}}\Big)\Big((n\pi)^2 T_n - \Big(\frac{m\pi}{\Gamma}\Big)^2 T_n\Big) \tag{2.145}$$

$$0 = \frac{m\pi}{\Gamma}T_n + \sqrt{\frac{Pr}{Ra}}\Big((n\pi)^2\omega_n - \Big(\frac{m\pi}{\Gamma}\Big)^2\omega_n\Big) \tag{2.146}$$

$$\omega_n = -((n\pi)^2\psi_n - \Big(\frac{m\pi}{\Gamma}\Big)^2\psi_n). \tag{2.147}$$

This is a system of three equations and three unknowns. T_n, ω_n, and ψ_n can be eliminated through algebra, which is especially possible in this case because of the simple geometry and boundary conditions.

Thus, we can solve for the critical Rayleigh number Ra_c, which gives us the value of buoyancy relative to diffusion at which the solutions remain constant in time. Above above Ra_c, the solutions will begin to grow. For RBC, the relationship between Ra_c, Γ, and the horizontal and vertical mode numbers is

$$Ra_c(n, m, \Gamma) = \Big(\frac{\pi}{\Gamma}\Big)^4 \frac{(m^2 + (\Gamma n)^2)^3}{m^2}. \tag{2.148}$$

Next, we make the assumption that the most unstable convective pattern is that in which the vertical mode number n is 1, or where convective plumes extend from the bottom to top of the domain.

With this assumption, we can test Eq. 2.148 numerically by running a series of hydrodynamic and linear cases with the code at a given value of Ra and Γ. We gradually increase Ra and monitor which horizontal mode number m is the most unstable. This allows us to find the

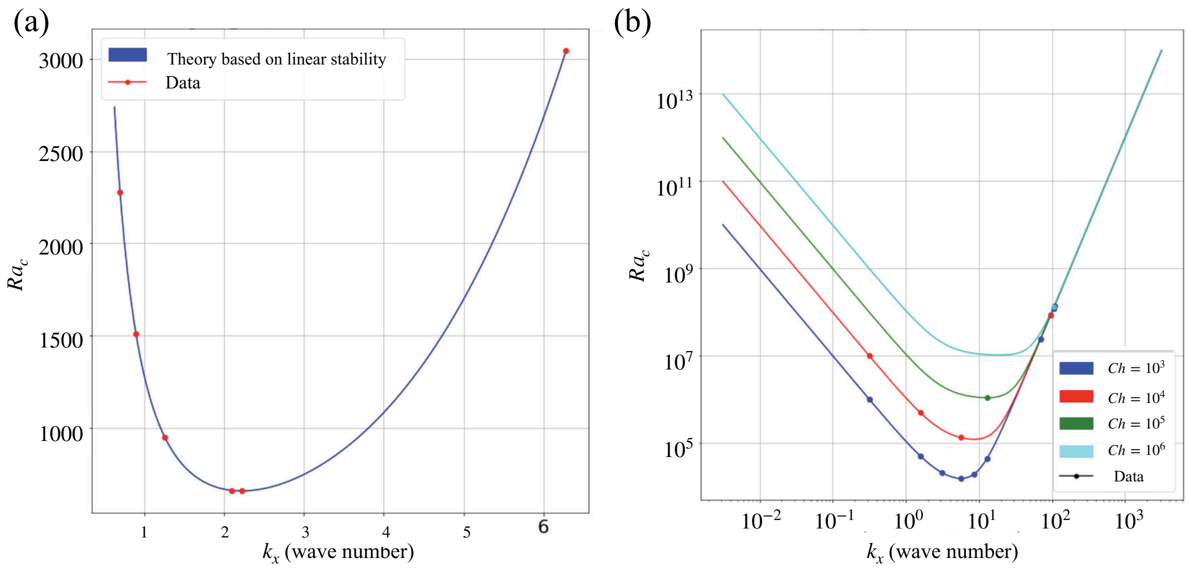

Figure 2.20: (a) Testing the RBC dispersion relationship Eq. 2.148 using the linear, hydrodynamic version of the code. The solid blue line represents the theoretical curve derived from linear stability analysis, and the red points give Ra_c found at six different horizontal wave numbers. (b) Testing the MC dispersion relationship Eq. 2.150 using the linear, magnetohydrodynamic version of the code. The solid colored lines represent the theoretical dispersion relationship between Ra_c, k_x, and Ch for four different values of Ch. The points then represent Ra_c as a function of k_x and Ch as found from linear MC simulations.

critical horizontal wavenumber k_x such that the convection instability sets in. The results of these simulations are shown in Fig. 2.20(a), where the red points show the most unstable wavenumber k_x where

$$k_x = \frac{2\pi m}{\Gamma}, \tag{2.149}$$

and its corresponding value of Ra_c. We find good agreement between our linear code (red points) and the theoretical marginal stability curve (dark blue line). This validates the hydrodynamic, linear version of our solver. Thus, we can increase the complexity by adding a magnetic field.

A similar analytical process can be carried out for MC linear theory to find a dispersion relationship for Ra_c where a quasi-static vertical magnetic field is included in the governing equations (Davidson, 2001). Since the presence of a magnetic field suppresses convection, Ra_c now depends also on Ch. Linearizing Eq. 2.62-2.63 with the electromagnetic term included, substituting the same Fourier expansions, solving the system of equations, and assuming the vertical mode number $n = 1$ is the most unstable gives

$$Ra_c(m, Ch, \Gamma) = \frac{(\Gamma^2 + m^2)(Ch\, \Gamma^4 \pi^2 + (\Gamma^2 + m^2)m^4)}{\Gamma^4 m^2}. \tag{2.150}$$

To test the efficacy of our linear magnetoconvection model, we again run a series of linear cases with the code at a given value of Ra and Γ. However, we also run an additional set of cases at various values of Ch. For each set up input parameters, we gradually increase Ra and monitor which horizontal mode number is the most unstable, and use this to find the critical horizontal wavenumber k_x such that the convection instability sets in. The results of these simulations are shown in Fig. 2.20(b), where the red points show the most unstable wavenumber k_x and its corresponding value of Ra_c. We find good agreement between our linear code (red points) and the theoretical marginal stability curve (dark blue line). This validates the hydrodynamic, linear version of our solver. Thus, we can increase the complexity by adding a magnetic field.

Fig. 2.20(a,b) demonstrate good agreement between both RBC and MC linear stability analysis and the linear version of the numerical model, which validates the code and methods chosen. We proceed by including nonlinear terms in our solver and comparing our results to similar studies.

2.7.1.2 Benchmarking to Fully Nonlinear RBC Code

We return to the hydrodynamic version of the code for the next benchmark. However, we include the nonlinear terms of Eq. 2.62-2.63 and use a finite difference approach to represent the variables in the vertical direction. There is no analytical solution for comparison with the model results. Rather, we validate our code using (Glatzmaier, 2014), who tabulates a set of Fourier coefficients T_m, ω_m, and ψ for the first 21 horizontal Fourier mode numbers at a particular set of input parameters.

The suggested benchmark case from (Glatzmaier, 2014) (pg. 46) was run at $Ra = 10^6, Pr = 0.3, \Gamma = 3$. The number of grid points in the vertical direction is $N_y = 101$ and the number of horizontal Fourier modes is $M = 50$. At this set of Rayleigh and Prandtl numbers, we expect the solution to first increase exponentially in time until the nonlinear terms are large enough to stop the growth. Eventually, the solution should reach steady state, where $d/dt \approx 0$ for all quantities.

Following (Glatzmaier, 2014), the values of $T_m(y = 0.32, m), \omega(y = 0.32, m), \psi(y = 0.32, m)$ were recorded after about one million time steps once the solution reached a steady staet. The values found from the code developed for this study are listed in Table 2.2. These are nearly identical to t (Glatzmaier, 2014) (Table 4.1), which confirms the accuracy of the RBC nonlinear code.

Table 2.2: Results of nonlinear RBC benchmark comparing to (Glatzmaier, 2014) (pg. 46). Table gives the steady state nondimensional values of the coefficients T_m, ω_m, ψ_m at $y = 0.32$ for up to the first 21 horizontal mode numbers. The input parameters are $Ra = 10^6, Pr = 0.3, \Gamma = 3$.

m	T_m	ω_n	ψ_m
0	0.5001	0.0000	0.0000
1	2.9144×10^{-3}	5815.6088	567.8245
2	2.5265×10^{-4}	-3.5893	-0.6740
3	2.9057×10^{-2}	1930.6893	103.8976
4	2.8771×10^{-4}	-6.6099	-0.5361
5	2.8900×10^{-2}	1149.4034	32.3309
6	3.4964×10^{-4}	-11.0563	-0.39578
7	2.8701×10^{-2}	811.2963	13.1672
8	4.7860×10^{-4}	-14.7794	-0.2838
9	2.8273×10^{-2}	617.1739	6.3751
10	6.4516×10^{-4}	-16.9695	-0.2064
11	2.7427×10^{-2}	488.8297	3.4608
12	8.0751×10^{-4}	-21.4400	-0.15389
13	2.60558×10^{-2}	398.4199	2.0308
14	9.7796×10^{-4}	-26.1548	-0.1167
15	2.4158×10^{-2}	326.80564	1.2579
16	1.1648×10^{-3}	-24.6904	-0.08885
17	2.1898×10^{-2}	264.6190	0.80977
18	1.2858×10^{-3}	-20.3570	$-0.0.7782$
19	1.9553×10^{-2}	216.2080	0.537140
20	1.25455×10^{-3}	-21.9120	-0.0524029

Appendix A

Benchmarking to Fully Nonlinear RBC and MC Code

The final step of the code validation process is to compare the results of our fully nonlinear code to additional studies. Here, we include the flexible, open-source, pseudo-spectral DNS code DEDALUS (Burns et al., 2020) in the benchmarking process because Dedalus is used for numerically challenging cases at $Ra \geq 10^9$.

We begin by comparing a set of $Ch = 0$ (hydrodynamic) cases for the code developed for this study and Dedalus against the results of (Goluskin et al., 2014). The time-averaged Nusselt number, $\langle Nu \rangle_t$ was calculated for seven different Rayleigh numbers at $\Gamma = 2$, $Pr = 1$. Purposefully, we include cases in which jets develop. In addition, the code developed for this and Dedalus were benchmarked to one another for a set of eight different $Ch \neq 0$ with varying Ra. Differences in the three codes yield errors less than 0.15%. Both the code developed for this study and Dedalus converged to the values listed in the table as the resolution was increased and the simulations were run for longer periods of time. Table A gives the results.

Table A.1: Comparison of the time averaged Nusselt number for the code used for this study (TS), Dedalus (D), and (Goluskin et al., 2014) (G). Each row gives the set of input parameters, and the time averaged Nusselt number from each code.

Γ	Ra	Ch	$\langle Nu\rangle_t(TS)$	$\langle Nu\rangle_t(D)$	$\langle Nu\rangle_t(G)$.
2	10^4	0	4.988	4.988	4.993
2	1.75×10^4	0	6.184	6.183	6.188
2	2×10^4	0	6.505	6.505	6.509
2	10^5	0	11.740	11.736	11.738
2	5×10^5	0	3.553	0	3.530
2	10^6	0	3.710	0	3.714
2	2.5×10^6	0	3.584	0	3.540
2	3×10^5	10	16.300	16.299	–
2	3×10^5	10^2	10.293	10.297	–
2	3×10^5	10^4	3.170	3.173	–
2	1×10^8	10^6	14.486	14.478	–
2	3×10^6	10	13.169	13.779	–
2	3×10^7	10^2	29.025	28.973	–
2	3×10^6	10^3	13.234	13.250	–
2	1×10^8	10^5	25.983	26.012	–

Appendix B

Data Tables

Table B.1: Details of the DNS. Each row gives Ch, Ra, its ratio above onset Ra/Ra_c, vertical resolution n_y, horizontal resolution n_x, the time average of the Nusselt number ($\langle Nu\rangle_t$), and the area-time averages of the horizontal Reynolds number and vertical Reynolds number ($\langle Re_x\rangle_t$, $\langle Re_y\rangle_t$) respectively.

Ch	Ra	Ra/Ra_c	n_y	n_x	$\langle Nu\rangle_t$	$\langle Re_x\rangle_{x,y,t}$	$\langle Re_y\rangle_{x,y,t}$
0	3×10^3	4.56	96	356	3.08	10.14	9.99
0	7×10^3	10.64	96	356	4.34	19.23	18.86
0	3×10^4	45.62	96	356	7.57	52.19	51.87
0	7×10^4	1.06×10^2	96	356	10.32	91.94	91.71
0	3×10^5	4.56×10^2	120	380	17.31	241.76	241.62
0	7×10^5	1.06×10^3	120	380	4.33	309.68	35.28
0	3×10^6	4.56×10^3	132	404	3.46	584.80	36.38
0	7×10^6	1.06×10^4	132	404	3.58	1030.43	60.53
0	3×10^7	4.56×10^4	168	452	4.03	2214.02	83.24
0	1×10^8	1.52×10^5	516	1032	4.73	7030	120.1
0	1×10^9	1.52×10^6	1024	2048	6.85	25240	251.1
0	1×10^{10}	1.52×10^7	3072	6144	8.61	118270	500.20
10	3×10^3	3.25	96	356	2.78	8.39	8.29
10	7×10^3	7.58	96	356	3.99	16.34	15.94
10	3×10^4	32.5	96	356	7.04	44.42	43.96
10	7×10^4	75.8	96	356	9.66	77.88	77.59
10	3×10^5	3.25×10^2	120	380	16.30	203.76	203.61
10	7×10^5	7.58×10^2	120	380	9.64	390.77	79.37
10	3×10^6	3.25×10^3	132	404	13.78	973.89	153.56
10	7×10^6	7.58×10^3	132	404	8.99	1115.95	115.44
10	3×10^7	3.25×10^4	168	452	9.06	2295.66	148.98

Table B.2: Previous table continued.

Ch	Ra	Ra/Ra_c	n_y	n_x	$\langle Nu\rangle_t$	$\langle Re_x\rangle_{x,y,t}$	$\langle Re_y\rangle_{x,y,t}$
10	1×10^8	1.08×10^5	360	720	9.14	4656.67	159.79
10	1×10^9	1.08×10^6	1536	3072	22.3	23497	2200.4
10	1×10^{10}	1.08×10^7	2048	4096	41.2	101131	1347
10^2	3×10^3	1.13	96	356	1.17	1.54	1.54
10^2	7×10^3	2.64	96	356	2.55	7.11	6.96
10^2	3×10^4	11.3	96	356	4.703	14.10	28.22
10^2	7×10^4	26.4	96	356	5.61	35.41	30.35
10^2	3×10^5	1.13×10^2	120	380	10.30	96.46	89.38
10^2	7×10^5	2.64×10^2	120	380	13.48	168.51	154.96
10^2	3×10^6	1.13×10^3	132	404	19.94	441.64	375.33
10^2	7×10^6	2.64×10^3	168	452	23.35	754.73	547.60
10^2	3×10^7	1.13×10^4	192	500	28.97	1900.81	843.33
10^2	1×10^8	3.77×10^4	256	636	32.88	4149.99	758.15
10^2	1×10^9	3.77×10^5	768	1536	43.06	15246	1123.95
10^2	1×10^{10}	3.77×10^6	3072	6144	61.05	59423	2214.6
10^3	3×10^4	1.97	96	356	2.35	4.52	9.23
10^3	7×10^4	4.60	96	356	3.96	10.18	19.99
10^3	3×10^5	19.7	120	380	7.48	23.94	71.96
10^3	7×10^5	46.0	120	380	9.28	49.11	84.79
10^3	3×10^6	1.97×10^2	132	404	13.25	123.31	171.07
10^3	7×10^6	4.60×10^2	168	452	16.23	218.0	247.99
10^3	3×10^7	1.97×10^3	168	452	24.56	576.78	543.45
10^3	1×10^8	6.58×10^3	252	636	36.25	1294.93	1199.18
10^3	1×10^9	6.58×10^4	984	1964	79.403	6136.48	5936.12
10^3	1×10^{10}	6.58×10^5	1536	3072	165.22	27012	26218

Table B.3: Previous table continued.

Ch	Ra	Ra/Ra_c	n_y	n_x	$\langle Nu \rangle_t$	$\langle Re_x \rangle_{x,y,t}$	$\langle Re_y \rangle_{x,y,t}$
10^4	3×10^5	2.50	120	380	3.17	5.47	23.17
10^4	7×10^5	5.84	120	380	5.78	12.33	50.96
10^4	3×10^6	25.0	132	404	10.30	34.72	131.55
10^4	7×10^6	58.4	192	380	14.48	58.97	205.67
10^4	3×10^7	2.50×10^2	192	452	23.61	167.38	471.86
10^4	1×10^8	8.34×10^2	216	472	31.09	384.21	775.10
10^4	1×10^9	8.34×10^3	576	1172	59.03	1786.98	1988.51
10^4	1×10^{10}	8.34×10^4	1536	3072	112.7	7924.37	7441.40
10^5	3×10^6	2.78	132	404	4.04	6.45	48.73
10^5	7×10^6	6.49	168	452	8.42	14.06	122.81
10^5	3×10^7	27.8	168	452	16.38	39.03	362.61
10^5	1×10^8	92.73	192	500	26.01	78.90	714.50
10^5	1×10^9	9.27×10^2	360	692	58.89	516.79	2112.05
10^5	1×10^{10}	9.27×10^3	1536	3072	115.50	2520.92	4850.22
10^6	1×10^8	9.72	96	356	14.47	23.49	332.0
10^6	1×10^9	97.2	384	764	38.36	103.37	1689.52
10^6	1×10^{10}	9.72×10^3	1536	3072	108.34	621.39	5870.90

CHAPTER 3

Rotating Convective Flows in Paraboloidal Laboratory Experiments

3.1 Introduction

Planetary magnetic fields, which are typically generated and sustained through conducting fluid motions, reveal global-scale features on all planets with an active dynamo (Bloxham and Gubbins, 1985). For Earth, where the magnetic field data is of the highest resolution to date, a number of hypotheses have been proposed to explain the planet's domain-scale, dipolar magnetic field structure. The list includes the dominance of low wave number modes in core flows, or the transfer of energy from small to large scales that can occur in constrained, turbulent systems (Aurnou et al., 2015). It is turbulent fluid motions in Earth's liquid iron outer core that likely sustain the dynamo generating the large-scale geomagnetic field. However, the remote nature of core flow precludes the direct measurement of these fluid motions. Understanding the flow, which is influenced by planetary rotation, buoyancy and magnetic forces, and the geometry of the spherical shell, among other mechanisms, has been the focus of a number of recent forward models, which often employ simplifications due to the complexity of the system (Glatzmaier and Roberts, 1995; Guervilly et al., 2019; Aurnou et al., 2015).

One such simplification can be made by modeling the outer core as a quasi-geostrophic system (QG). In the outer core, flows are dominated by rotation and the Coriolis force nearly balances pressure gradients (Phillips, 1963). As a result, flows tend to align with the axis

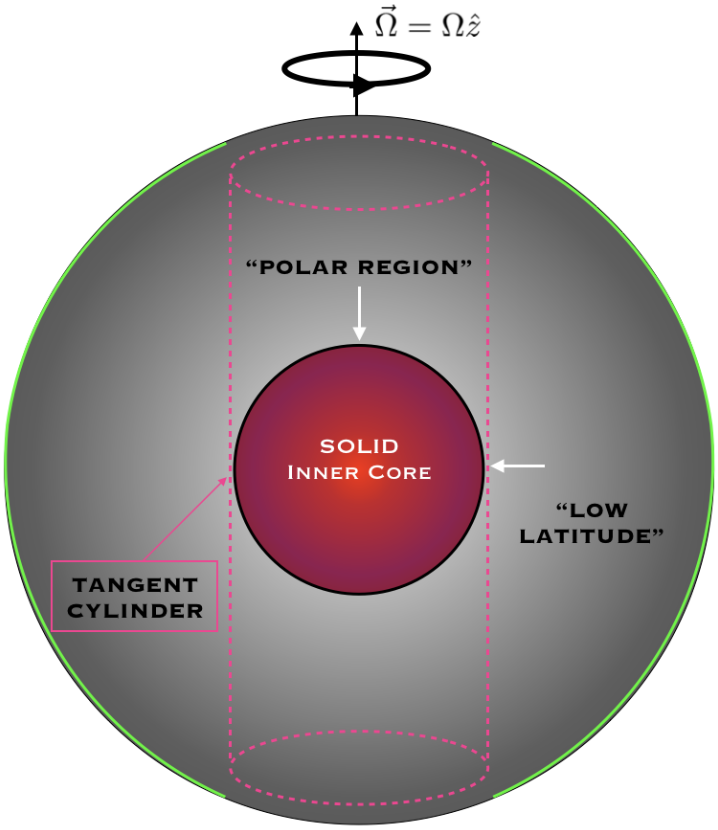

Figure 3.1: Schematic of Earth's interior below the mantle, with a hot inner core, tangent cylinder, and gravitational acceleration that is radially inwards. The green curves emphasize the shape of the sphere's outer boundary, which plays a crucial role in core fluid dynamics.

of rotation, which leads to two dynamically distinct fluid regions defined by the tangent cylinder (TC), the axially aligned cylindrical region bisecting the inner core. The first region is at high latitudes, inside the TC, where radially directed buoyancy forces align with the axis of rotation. Fig. 3.1 gives a schematic of the core, where the tangent cylinder is denoted with a pink dashed line. Core flow inside the TC has been studied in King and Aurnou (2015); Cheng et al. (2015), among others. The second, highlighted with the green line in Fig. 3.1, describes the area outside the TC at lower latitudes where the curvature of the spherical domain becomes large and the buoyancy forces are approximately perpendicular to the axis of rotation. Buoyancy, originating at the Inner Core Boundary (ICB), is of particular importance in core dynamics because it likely drives inertial flows through convection (Lister and Buffett, 1995). Furthermore, this leading order balance between Coriolis and pressure also allows us to model core flow with a purely hydrodynamic system, where we neglect electromagnetic forces (Soderlund et al., 2012, 2015; Yadav et al., 2016; Sheyko et al., 2018).

The strongly nonlinear regime of turbulent convection outside the TC has not been well-characterized to date (Gillet et al., 2007; Aurnou et al., 2015). Though studies have been done on weakly nonlinear convection in a sphere (Guervilly and Cardin, 2016), the turbulent, fully 3D regime remains difficult to access experimentally owing primarily to Ekman friction at the boundaries and limitations on container size (Cardin and Olson, 1994; Aubert et al., 2001). By forgoing a spherical container, and instead relying on a paraboloidal free surface for curvature, we minimize Ekman friction while taking advantage of the strong laboratory turbulence necessary to create analog models of Earth-like core convection. Fig. 3.2(a,b) emphasizes the similarities in flow morphologies between our paraboloidal free surface device (left panel) and a computationally expensive 3D spherical shell model of core convection carried out by Mound et al. (2019) (right panel). In both images, one can observe similarities in the length scale of convection and alternating bands of retrograde/prograde flow. Our laboratory device, which is more tractable and flexible than current spherical shell direct numerical simulations, offers a new method to study turbulent core convection.

Laboratory experiments that utilize a curved free surface have been carried out, but either have a limited strength of boundary curvature or use hydraulic pumps to force small-scale turbulence (Matulka et al., 2016; Cabanes et al., 2017; Lemasquerier et al., 2021; Smith et al., 2014). The device presented in this study is the first, to our knowledge, that leverages significant curvature from a paraboloidal free surface, generates a heat flux comparable to that of a spherical shell, and drives the system self-consistently using convection to model low-latitude core dynamics.

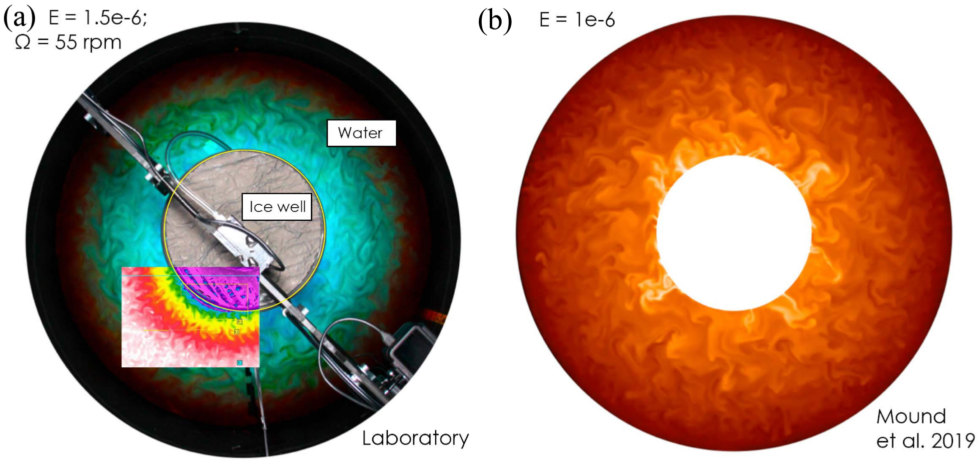

Figure 3.2: (a) Top view of the laboratory paraboloidal free surface device used in this study at a rotation rate of $\Omega = 55$ RPM. Dye is used to color the working fluid (water) and trace fluid motions. The inset at the bottom left shows a comparative thermographic image from the thermal IR camera, where red corresponds to warmer fluid and blue corresponds to cooler fluid. (b) Temperature snapshot of an equatorial slice of a spherical shell core convection model carried out by (Mound et al., 2019). Light colors are used for warmer fluid, and dark colors are used for cooler fluid.

Boundary curvature can strongly influence core flow outside the TC, as the curvature of a spherical shell increases towards lower latitudes. The boundary curvature of a rotating system, where the fluid layer height varies with cylindrical radius, can best be described by a mechanism known as the topographic β-effect,

$$\beta = -\frac{2\Omega}{h(s)}\frac{dh}{ds}, \tag{3.1}$$

where Ω is the global rotation rate, h is the fluid layer height, and s is the cylindrical radius (Sinha and Richards, 1999).

In this approximately axially-invariant system with geostrophic turbulence, energy can be transferred from high to low wavenumbers, also known as the inverse energy cascade

(Kraichnan, 1967). However, the β-effect can anisotropize the QG flow and halt the inverse energy cascade at a scale known as the Rhines scale (Rhines, 1975), which corresponds to the wavenumber,

$$k_{Rh} = \sqrt{\frac{\beta}{2U}}, \tag{3.2}$$

where U is a characteristic velocity. Jets, whose widths follow this characteristic Rhines scale, have been observed in several numerical simulations of the Jovian atmosphere (Heimpel et al., 2005; Scott and Dritschel, 2012b), but could also be prominent large-scale features in low-latitude core flow (Gastine, 2019; Calkins et al., 2012b; Gillet and Jones, 2006).

Zonal flows are often essential in dynamo processes, providing large-scale shears that can convert components of poloidal fields into toroidal fields. Fig. 3.3(a) is a schematic depicting a simplified version of this process, also known as the Ω-effect. Here, a vertical magnetic field $\boldsymbol{B}$ is sheared by a perpendicular velocity field $\boldsymbol{u}$, leading to a new $\boldsymbol{B}$ with a horizontal component. The Ω-effect is the main driver of the dynamo process in astrophysical bodies like the Sun, where differential rotation winds up an initially poloidal field into a toroidal field (Stix, 1976; Cameron et al., 2017). Convection can also drive an additional dynamo process, known as the α-effect, in which a toroidal magnetic field $\boldsymbol{B}$ is twisted into a poloidal field, directed in r, through helical fluid motions. Therefore, characterizing the formation and evolution of zonal flows driven by convection in our novel paraboloidal device can further our understanding of core dynamo processing by elucidating the importance of the Ω-effect.

The rest of this chapter is organized as follows: Sec. 3.1.1 and Sec. 3.1.2 give the mechanisms through which we drive turbulence in this system, namely centrifugal acceleration and baroclinic instability. The experimental set up is discussed in Sec. 3.2. Sec. 3.3 compares key features of the paraboloidal geometry, the topographic β-effect and heat flux, with that of a spherical shell. In Sec. 3.4 we give the results including Rossby waves, alternating prograde-retrograde jets that closely follow the Rhines scale, jets that migrate laterally, and the Stewartson boundary layer. Sec. 3.4.5 lays the groundwork for future quasi-geostrophic

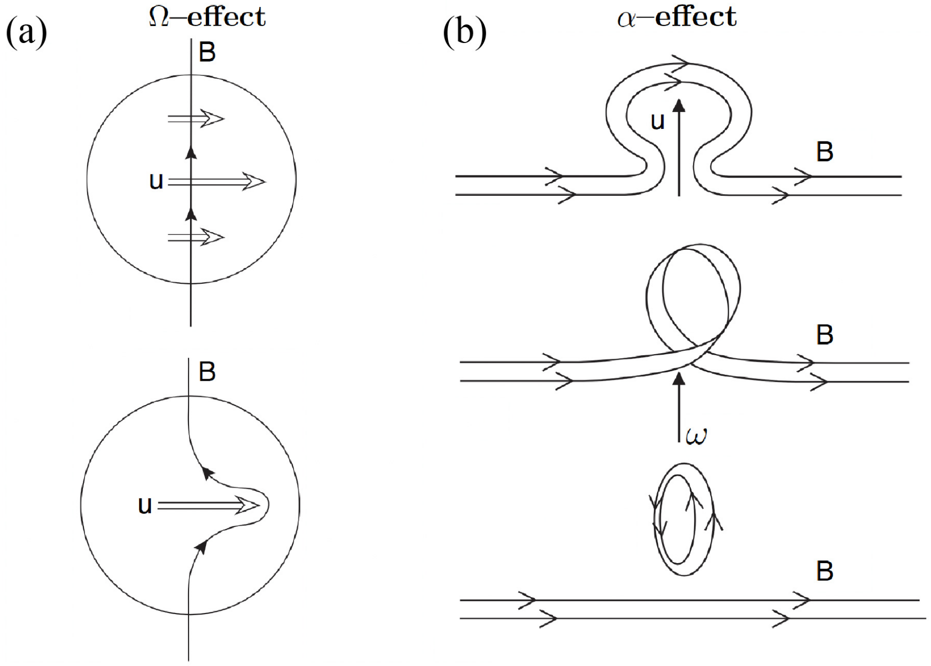

Figure 3.3: Figure adapted from Roberts (2015). Schematic illustrating the dynamo process. (a) The Ω-effect in which a vertical magnetic field $\boldsymbol{B}$ is sheared by a perpendicular velocity field $\boldsymbol{u}$, leading to a new $\boldsymbol{B}$ with a horizontal component. (b) The α-effect, in which a toroidal magnetic field $\boldsymbol{B}$, directed in (θ, ϕ) is twisted into a poloidal field, directed in r, through helical fluid motions.

paraboloidal models. We conclude in Sec. 3.5. App. C gives additional work carried out to fit the jet migration velocity. In App. D we provide a script used to track the radial migration of a jet core in time.

3.1.1 Governing Equations

The source of turbulence in nature is often convection, an instability driven by a fluid in an unstable density configuration. The archetype laboratory and numerical set up is Rayleigh-Bénard convection (RBC), where a fluid is vertically confined between two parallel plates, and heated at the bottom boundary and cooled from the top. Further, when rotation is applied to RBC, typically along the axis parallel to gravity, fluid motions can be constrained along the axis of rotation. "Geostrophic turbulence" is then a regime where rotation remains dominant, but less significant due to strongly nonlinear interactions (in this case driven by convection) (McWilliams, 2006). It has been shown by Guervilly and Hughes (2017) and Julien et al. (2018a) that domain-scale structures, such as vortices can result from geostrophic turbulence in rotating RBC with periodic boundary conditions.

For the purposes of simulating core convection outside of the TC, we model buoyancy that is orthogonal, in addition to parallel, to the rotation axis. The idea of using centrifugal acceleration as a laboratory proxy for radially directed gravity in the core was proposed by Busse and Carrigan (1974). A cold source at radius R_i is located at the center of a rotating tank of fluid total radius R_o. The colder, denser parcels of fluid are pushed radially outwards, and warmer parcels at the outer boundary are pulled radially inwards with a centrifugal acceleration, $\boldsymbol{a_c} = \Omega^2 s\boldsymbol{\hat{s}}$, where Ω is the rotation rate.

To understand the control parameters that give the onset of the centrifugally driven convective instability, we turn to the governing equation of momentum conservation for a Boussinesq, rotating fluid

$$\rho\Big(\frac{\partial \boldsymbol{u}}{\partial t} + (\boldsymbol{u}\cdot\boldsymbol{\nabla})\boldsymbol{u}\Big) + \rho(2\Omega\boldsymbol{\hat{z}}\times\boldsymbol{u}) = -\nabla P + \rho g\boldsymbol{\hat{z}} - \rho\Omega^2 s\boldsymbol{\hat{s}} + \nu\rho\boldsymbol{\nabla}^2\boldsymbol{u}, \tag{3.3}$$

where $\boldsymbol{u}$ is the fluid velocity, P is the pressure, ρ is the fluid density, α is the expansivity of the fluid, g is gravity in the $\boldsymbol{\hat{z}}$-direction, ν is the viscosity, and Ω is the rotation rate. The second to last term on the right hand side of Eq. 3.3 is the centrifugal buoyancy contribution.

The temperature equation is

$$\frac{\partial T}{\partial t} + (\boldsymbol{u}\cdot\boldsymbol{\nabla})T = \kappa\nabla^2 T, \tag{3.4}$$

where κ is the thermal diffusivity. We can apply the Boussinesq approximation, where ρ is equal to the mean density ρ_0 in all terms but the buoyancy terms. In the buoyancy terms, density variations are related directly to variations in the fluid temperature by

$$\rho = \rho_0(1 - \alpha(T - T_0)), \tag{3.5}$$

where α is the thermal expansion coefficient of the fluid and T is the fluid temperature relative to the mean T_0.

We can find hydrostatic balance from the momentum equation. The static state is recovered when $\boldsymbol{u} = 0$

$$\boldsymbol{\nabla} P = \rho g \hat{\boldsymbol{z}} - \rho \Omega^2 \hat{\boldsymbol{s}}. \tag{3.6}$$

Subtracting this from Eq. 3.3 gives

$$\frac{\partial \boldsymbol{u}}{\partial t} + (\boldsymbol{u} \cdot \boldsymbol{\nabla})\boldsymbol{u} + (2\Omega \hat{\boldsymbol{z}} \times \boldsymbol{u}) = -\frac{1}{\rho_0}\nabla p + \alpha(T - T_0) g \hat{\boldsymbol{z}} - \alpha(T - T_0)\Omega^2 s \hat{\boldsymbol{s}} + \nu \boldsymbol{\nabla}^2 \boldsymbol{u}, \tag{3.7}$$

where p is now the dynamic pressure.

We can nondimensionalize the equations for momentum and temperature. Length is scaled by $R_o - R_i$, temperature is scaled by $\Delta T_\perp, \Delta T_\parallel$ in the radial and vertical directions respectively, and pressure is scaled by $\rho_0 \alpha \Delta T_\perp \Omega (R_o - R_i)^2$. Time is scaled by the free fall time scale, which estimates the time it takes for a buoyant, undamped parcel of fluid to radially cross the fluid layer

$$\tau_{ff\perp} = \frac{(R_o - R_i)}{\sqrt{\alpha \Delta T_\perp \Omega^2 (R_o - R_i)^2}}. \tag{3.8}$$

The velocity is scaled by the free fall velocity, which estimates the speed at which a buoyant, undamped parcel of fluid will radially cross the fluid layer

$$U_{ff\perp} = \sqrt{\alpha \Delta T_\perp \Omega^2 (R_o - R_i)^2}. \tag{3.9}$$

Using these scales gives

$$\frac{\partial \boldsymbol{u}}{\partial t} + (\boldsymbol{u} \cdot \boldsymbol{\nabla})\boldsymbol{u} + Ro_\perp^{-1}(\hat{\boldsymbol{z}} \times \boldsymbol{u}) = -\nabla P + \frac{\gamma}{Fr} T \hat{\boldsymbol{z}} - T s \hat{\boldsymbol{s}} + \sqrt{\frac{Pr}{Ra_\perp}} \nabla^2 \boldsymbol{u} \tag{3.10}$$

and

$$\frac{\partial T}{\partial t} + (\boldsymbol{u} \cdot \boldsymbol{\nabla}) T = \frac{1}{\sqrt{Ra_\perp Pr}} \nabla^2 T. \tag{3.11}$$

Additional definitions to note are the Coriolis (τ_Ω), viscous (τ_ν), and thermal diffusion (τ_κ) timescales

$$\tau_\Omega = \frac{1}{2\Omega};\ \tau_\nu = \frac{(R_o - R_i)^2}{\nu};\ \tau_\kappa = \frac{(R_o - R_i)^2}{\kappa}. \tag{3.12}$$

The control parameters here are: the perpendicular Rayleigh number that describes the ratio of centrifugal buoyancy to diffusion

$$Ra_\perp = \frac{(\tau_{ff\perp})^2}{\tau_\nu \tau_\kappa} = \frac{(\alpha \Delta T_\perp \Omega^2)(R_o - R_i)^4}{\nu\kappa}, \tag{3.13}$$

the centrifugal convective Rossby number that describes the ratio of buoyancy to Coriolis

$$Ro_\perp = \frac{\tau_\Omega}{\tau_{ff_\perp}} = \frac{\sqrt{\alpha \Delta T_\perp \Omega^2 (R_o - R_i)^2}}{2\Omega(R_o - R_i)}, \tag{3.14}$$

the Prandtl number that describes viscous to thermal diffusion

$$Pr = \frac{\tau_\kappa}{\tau_\nu} = \frac{\nu}{\kappa}, \tag{3.15}$$

the Froude number, the ratio of centrifugal acceleration to gravitational acceleration,

$$Fr = \frac{a_c}{g} = \frac{\Omega^2 (R_o - R_i)^2}{g}. \tag{3.16}$$

and the ratio of vertical to radial temperature gradient

$$\gamma = \frac{\Delta T_\parallel}{\Delta T_\perp}. \tag{3.17}$$

The convective Rossby number can be written as

$$Ro_\perp = \frac{Ek}{\sqrt{Ra_\perp\ Pr}}, \tag{3.18}$$

where Ek is the Ekman number that is frequently used as a control parameter in studies of core convection

$$Ek = \frac{\tau_\Omega}{\tau_\nu} = \frac{\nu}{\Omega (R_o - R_i)^2}. \tag{3.19}$$

Taking the curl of Eq. 3.7 gives the vorticity equation

$$\frac{\partial \boldsymbol{\omega}}{\partial t} + (\boldsymbol{\omega} \cdot \boldsymbol{\nabla})\boldsymbol{u} = ((\boldsymbol{\omega} + Ro_\perp^{-1} \hat{\boldsymbol{z}}) \cdot \boldsymbol{\nabla})\boldsymbol{u} + \boldsymbol{\nabla} \times \frac{\gamma}{Fr} T \hat{\boldsymbol{z}} - \boldsymbol{\nabla} \times T s \hat{\boldsymbol{s}} + \sqrt{\frac{Pr}{Ra_\perp}} \nabla^2 \boldsymbol{\omega}, \tag{3.20}$$

where the first term on the right hand side of Eq. 3.20 is a result of vortex stretching.

The $\hat{\boldsymbol{z}}$-component of Eq. 3.20 is

$$\frac{D\omega}{Dt} = ((\omega + Ro_{\perp}^{-1})\frac{\partial u_z}{\partial z} - \frac{\partial T}{\partial \phi} + \sqrt{\frac{Pr}{Ra_{\perp}}}\nabla^2 \omega, \tag{3.21}$$

In the quasigeostrophic limit where $Ro_{\perp}^{-1} \ll 1$ and viscous effects are neglected, Eq. 3.62 becomes

$$\frac{D\omega}{\partial t} = (Ro_{\perp}^{-1})\frac{\partial u_z}{\partial z} - s\frac{\partial T}{\partial \phi}. \tag{3.22}$$

We can integrate Eq. 3.22 over the axial z direction from $z = 0$ to nondimensional height $z = h(s)/(R_o - R_i)$ which yields

$$\frac{h(s)}{R_o - R_i}\frac{D\omega}{Dt} = Ro_{\perp}^{-1}\int_0^{h(s)/(R_o - R_i)} \frac{\partial u_z}{\partial z} dz - \Big(\frac{h(s)}{R_o - R_i}\Big)\frac{\partial T}{\partial \phi}. \tag{3.23}$$

The fluid layer height, h varies with radius, s, which results in

$$(u_z h(s) - u_z(s)) = \frac{Dh}{Dt} = u_s\frac{dh}{ds}. \tag{3.24}$$

Using Eq. 3.24 to simplify Eq. 3.23 gives

$$\frac{D\omega}{Dt} = Ro_{\perp}^{-1}\Big(\frac{(R_o - R_i)}{h(s)}\frac{dh}{ds}\Big)u_s + \frac{\partial T}{\partial \phi}. \tag{3.25}$$

The dimensional topographic β effect is defined as

$$\beta = -\frac{2\Omega}{h(s)}\frac{dh}{ds}. \tag{3.26}$$

We can nondimensionalize Eq. 3.26 with time scale $\tau_{ff_{\perp}}$ and length scale $R_o - R_i$ which gives nondimensional β'

$$\beta' = -Ro_{\perp}^{-1}\Big(\frac{R_o - R_i}{h(s)}\Big)\frac{dh}{ds}. \tag{3.27}$$

Substituting Eq. 3.27 into Eq. 3.25, we have

$$\frac{D\omega}{Dt} = -\beta' u_s + \frac{\partial T}{\partial \phi}. \tag{3.28}$$

Thus, the variation of fluid layer height stretches planetary vorticity, and generates local vorticity in the axial direction. This is quantified through the topographic β effect. In addition, the system is thermally forced through gradients of T in the azimuthal direction.

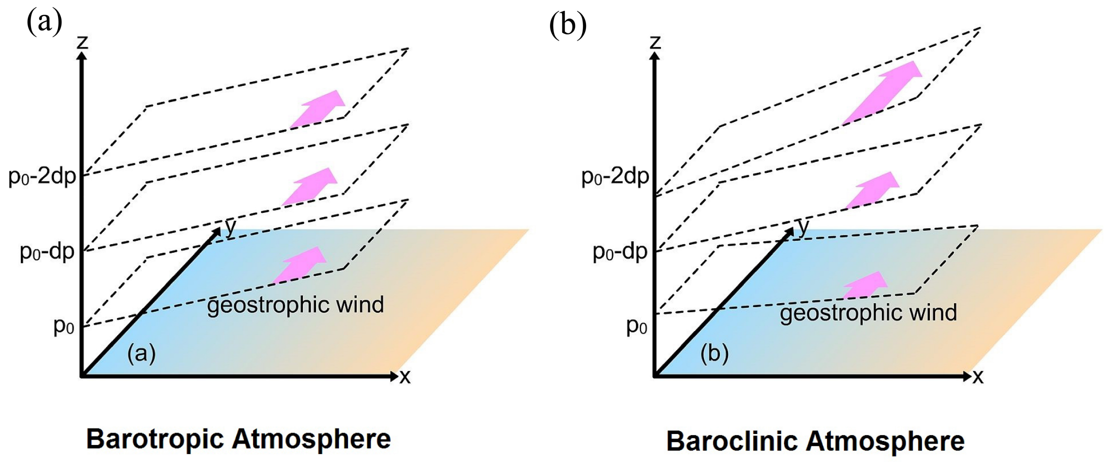

Figure 3.4: The horizontal flow on different isobaric levels in a (a) barotropic atmosphere compared to a (b) baroclinic (b). The blue portion denotes a cold region while the orange portion denotes a warm region. This temperature field extends throughout the fluid layer in the baroclinic case, though it is constrained to the surface in the barotropic case. The dotted lines give isobaric surfaces. Pink arrows demarcate the direction and amplitude of the horizontal flow. Only in the baroclinic atmosphere does the horizontal flow vary in height, which is known as thermal wind. Figure adapted from Wikipedia.

3.1.2 Baroclinic Flows

Though the centrifugal acceleration likely plays a key role in driving turbulence in this system, there is another mechanism that we consider here: baroclincity. The turbulence in this system may also be governed by the instability associated with constant density surfaces that are misaligned with constant pressure surfaces, which can in turn drive baroclinic eddies (Salmon, 1980; Pierrehumbert, 1984; McWilliams, 2006; Smith et al., 2014). In such a system, we can examine the vorticity, Eq. 3.20 under the quasigeostrophic limit where $Ro_\perp \ll 1$ and only the buoyancy balances Coriolis

$$(Ro_\perp^{-1}\hat{\boldsymbol{z}}\cdot\boldsymbol{\nabla})\boldsymbol{u} = \boldsymbol{\nabla}\times Ts\hat{\boldsymbol{s}} - \boldsymbol{\nabla}\times\frac{\gamma}{Fr}T\hat{\boldsymbol{z}}. \tag{3.29}$$

Retaining only the azimuthal component of Eq. 3.29 yields

$$\frac{\partial u_\phi}{\partial z} = Ro_\perp\left(\frac{\gamma}{Fr}\frac{\partial T}{\partial s} + s\frac{\partial T}{\partial z}\right), \tag{3.30}$$

which is also known as thermal wind balance (Cushman-Roisin and Beckers, 2011; McWilliams, 2006). Eq. 3.30 shows that the buoyancy gradients in this system set up a vertical shear of the zonal velocity, “thermal wind.”

Fig. 3.4(a,b) also demonstrates how a baroclinic system can set up a thermal wind. It shows a schematic of a barotropic atmosphere compared to a baroclinic atmosphere. In the baroclinic case, the temperature gradient at the bottom surface extends throughout the fluid layer, and leads to a tilt in the isobaric surfaces with height. This sets up a horizontal flow that changes with height. This shear is unstable, and can drive a mechanism known as baroclinic instability (BCI).

By linearizing the baroclinic, unforced governing equation of momentum and carrying out linear stability analysis, one can show that the scale of waves which grow most rapidly is the Rossby deformation radius (McWilliams, 2006)

$$R_D = \frac{N\mathcal{L}}{2\Omega}. \tag{3.31}$$

where $\mathcal{L}$ is a characteristic scale (typically the local height of the fluid layer). In addition, N is the Brunt-Väisälä frequency,

$$N = \sqrt{-\frac{g}{\rho_0}\frac{\partial \rho}{\partial z}}, \tag{3.32}$$

which characterizes the stability of a fluid to displacements driven by buoyancy.

A system can be forced by both baroclinic and convective instabilities. For example, Fig. 3.5 shows an image from a demonstration by the DIYnamics team. A tank with a radius of 18 cm is rotated at 10 RPM while a cold can of ice (radius approximately 4 cm) is placed at the center of the domain. The lateral temperature gradient of about 3° C, orthogonal to the vertical pressure gradient, sets up a thermal wind which undergoes

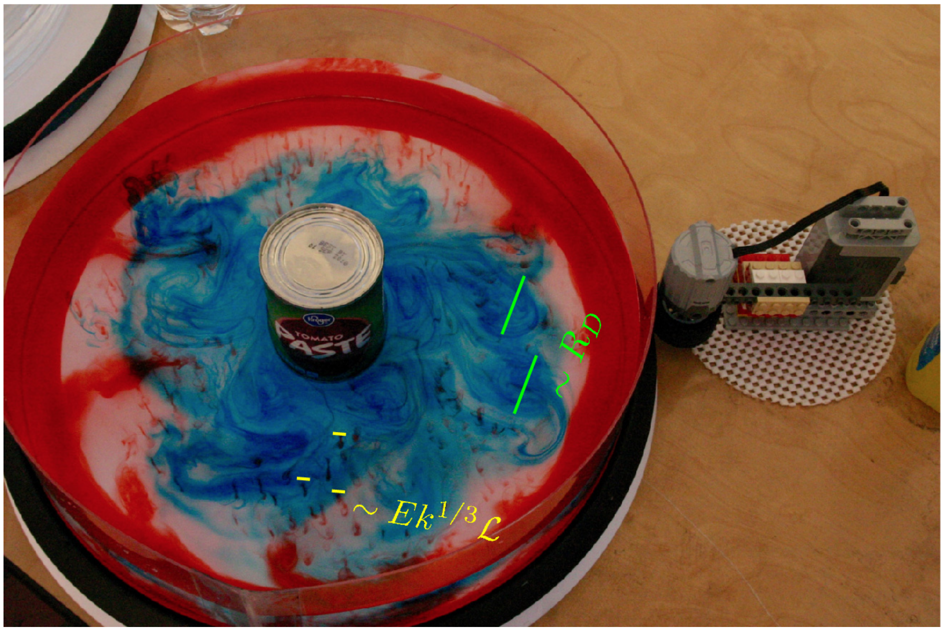

Figure 3.5: Figure adapted from Spencer Hill. Image of both baroclinic and convective instabilities in a DIYnamics demonstration. A tank of 18 cm is rotated at 10 RPM, while a can of ice is placed in the center of the domain. Both baroclinic eddies and rotating convective columns are observed, which closely match predicted scales. Calculations of R_D and $Ek^{1/3}\mathcal{L}$ are shown in the green and yellow lines respectively.

baroclinic instability. We can use Eq. 3.31 to predict the scale of the resulting eddies which gives $R_D = \sqrt{(\alpha g \Delta T_\perp (R_o - R_i))/(2\Omega^2)} \approx 1.94$ cm (bright green lines).

The dye used in this demonstration is denser than the water, which causes it to sink. The width of the columns which arise from rotating convection scale as $l_c \sim Ek^{1/3}\mathcal{L}$ where $\mathcal{L}$ is a characteristic length scale (details of this relationship are given in Sec. 3.4.4). Using the gap width for $\mathcal{L}$ gives $l_c \approx 0.405$ cm (bright pink lines). Both R_D and $Ek^{1/3}\mathcal{L}$ closely match the width of structures observed in this demo, which shows that baroclinic and convective instabilities coexist here.

3.2 Experimental Setup

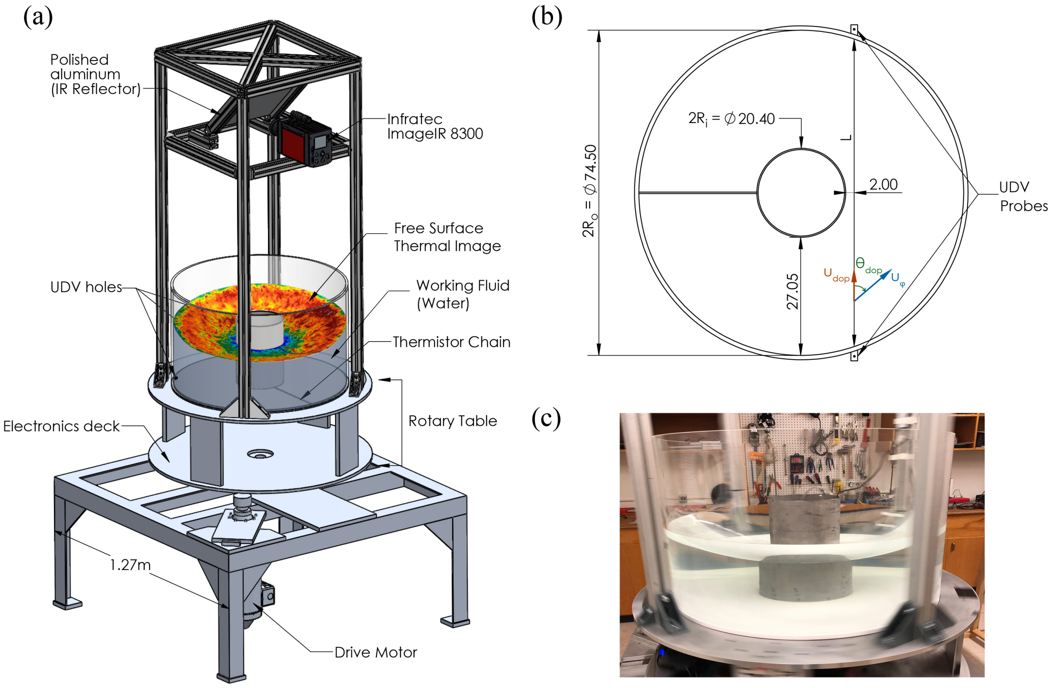

Figure 3.6: Figure from T. Lonner. (a) Novel experimental device to simulate low-latitude convection. Superimposed in the tank is a snapshot of the thermal IR field recorded from the ImageIR. A base temperature profile is recorded by the labeled thermistor chain, and the transducers for the Doppler Velocimeter are placed in the UDV holes. (b) The relevant dimensions of the tank. All values listed are in centimeters. (c) Side view of the tank where the curvature of the free surface is observable.

The natural convection experiments at three different rotation were performed by previous UCLA student, Taylor Lonner, using a novel laboratory device shown in Fig. 3.6. The tank is 1cm-thick acrylic and has an inner diameter of 74.5cm. Centered with this tank is a 3-mm thick aluminum insert with an outer diameter of 20.4cm. Convection is established by using hot water in the annulus of the acrylic tank and placing a solid block of ice in the inner aluminum cylinder. Cold water is added to the cylinder to couple the ice to the aluminum and allow for efficient heat transfer. This passive cooling is the main source of turbulence in the system. As the device rotates, the cold water at the boundary of the inner cylinder is centrifuged out and the hot water in the bulk moves inward. This centrifugal force works as a proxy for gravity at low latitudes in geophysical and astrophysical bodies where the forcing is similarly perpendicular to the axis of rotation (Busse and Carrigan, 1974).

In order to collect data from our system, we employ the use of the DOP 3010 Ultrasonic Doppler Velocimeter (UDV) from Signal Processing to collect azimuthal velocity profiles, an ImageIR 8300 from InfraTec for surface thermography, and a custom wireless thermistor array for additional point temperature measurements at the base of the tank. We use the UDV to multiplex through two transducers at sub-second frequencies. As shown in Fig. 3.6B, the transducers are placed opposite each other along a chord. The UDV is capable of reading velocities with 16-bit precision. Given our velocity scale, this equates to a precision of 0.9μ m/s and an accuracy within 5%. The ImageIR is located on the upper frame of the device facing a polished aluminum plate, which acts as a mirror for the water's surface. The pixel resolution of the camera's CCD is 640x512 and each pixel provides temperature reading with a precision of 20 mK. Finally, the wireless thermistor array was developed in-lab using an Arduino Mega and Xbees for wireless serial data transfer, and custom-calibrated Ametherm PANE-103395 thermistors. Seven thermistors were placed in a chain from the inner cylinder to the edge of the tank. The Arduino Mega has 10-bit precision which leads to thermistor precision around 25 mK.

Each case is run as follows. While the tank is stationary, it is filled to a set point and heated with a submersible heater to 50°C. The water is seeded with copolyamide particles at a density of 0.35 g/L. Once the desired temperature is reached, the ice block is placed in the aluminum cylinder and the device is slowly spun up to the desired rotation rate over about 3 minutes. Data collection begins here so we can observe spin-up dynamics if desired. From the beginning of spin-up, we record data for 40 minutes. We can find how long the device takes to reach solid-body rotation by formulating an Ekman spin-up time, τ_{Ek_l} for a cylindrical apparatus with one solid boundary and a free surface. The spin-up timescale for a homogenous fluid in a closed, cylindrical container is given by

$$\tau_{Ek,closed} = (8Ek_l)^{-1/2}\Omega^{-1} \tag{3.33}$$

where the $Ek_l = \nu/(2\Omega h^2)$ is the Ekman number (the ratio of viscosity to Coriolis) (Warn-Varnas et al., 1978; Greenspan and Howard, 1963). For a cylindrical system with only one boundary, the timescale for the fluid to reach solid-body rotation will be longer by a factor of two. This gives,

$$\tau_{Ek} = ((8Ek)^{-1/2}\Omega^{-1})2 = (2Ek)^{-1/2}\Omega^{-1} = h(\nu\Omega)^{-1/2}. \tag{3.34}$$

The Ekman number for each case is defined in Table 3.4.4.2, and solid-body rotation is observed after about 20 minutes. After finishing data collection, initial corrections are made to the data. For the UDV velocity data, this includes applying a Doppler angle correction assuming azimuthal flow on average for the transducers. Given the length of the chord, L, the depth from the transducer, d, and the radius of the aluminum cylinder, R_i, the Doppler angle can be calculated as

$$\theta\left(d\right)_{dop} = \tan^{-1}\left(\frac{L/2 - d}{R_i + 2cm}\right). \tag{3.35}$$

The 2cm adjustment in the denominator of 3.35 is due to the position of the chord relative to the inner cylinder as shown in Fig 3.6(b). To translate from Doppler velocity to azimuthal velocity, we merely apply a projection as follows at each depth from the transducer:

$$u_\phi = \frac{u_{dop}}{cos(\theta_{dop})} \tag{3.36}$$

In addition to the Doppler angle correction, we remove a surface wave from the UDV data. Since our system is slightly imbalanced, a surface wave with an angular frequency that matches the rotational frequency is present. However, we are able to characterize this wave, fit it, and subtract it from the velocity data.

For thermography, the IR camera assumes the surface is flat, rather than paraboloidal. Therefore, additional corrections must be made to the thermographic data. Calibration cases were taken prior to running experiments where the water was room temperature and there was no ice in the aluminum cylinder. These uniform-temperature cases are used to fit the temperature read by the IR camera to the temperature measured by the thermistors using Lambert's Cosine Law as follows:

$$T_0 = \frac{a\left(\theta_L\right) T}{\cos\left(\theta_L\right)} + b. \tag{3.37}$$

For 3.37, T_0 is the temperature measured by the thermistors, a is an adjustment coefficient which is approximately 1, θ_L is the angle between the surface normal and the axis of rotation, T is the temperature measured by the IR camera, and b is an offset used to match the IR camera's accuracy to that of the thermistors. Thermography data was sampled strategically at one image per rotation to remove the effects of the surface wave.

The thermographic data provides a method of extrapolating the velocity field. This can be shown by examining the equation for the evolution of temperature

$$\frac{\partial T}{\partial t} + \boldsymbol{u} \cdot \boldsymbol{\nabla} T = \kappa \nabla^2 T, \tag{3.38}$$

The thermal diffusivity of water is $\kappa = 1.4 \times 10^{-7}$ m^2/s. Considering two snapshots of the surface thermal field taken one second apart, the small-scale structures show little thermal diffusion. Therefore, it is possible to relate the evolution of the temperature field over time with the advection of the velocity field.

3.3 Theoretical Comparison Between Paraboloid and Sphere

3.3.1 Topographic β

The paraboloid also serves as a quantitative proxy to the topographic β effect resulting from a sphere. The shape of the paraboloidal free surface is controlled by the rotation rate and is described by the following equation

$$h(s)_{para} = h_0 + \frac{\Omega^2 s^2}{2g} = \frac{\Omega^2 s^2 + 2gh_0}{2g}, \tag{3.39}$$

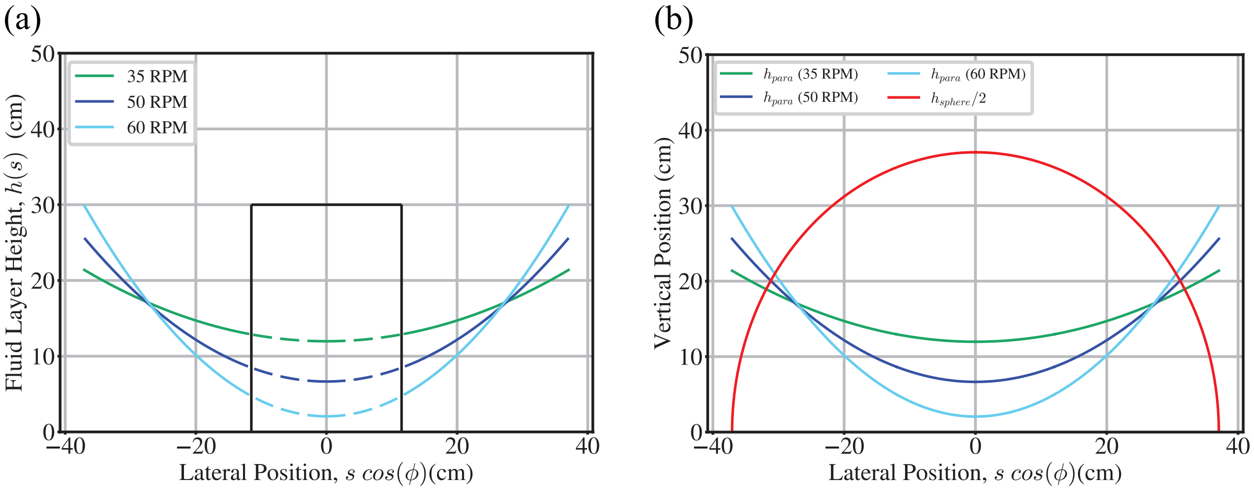

Figure 3.7: (a) Cross section of paraboloidal free surfaces, where the black solid line gives the location and height of the inner cylinder. (b) Comparing the paraboloidal free surfaces with that of a sphere. The x-axis for both plots is the lateral position across the tank where s is cylindrical radius and ϕ is the azimuthal position.

where h_0 is the theoretical minimum layer depth when $s = 0$, and g is the acceleration due to gravity.

Fig. 3.7(a) gives the height of the free surface for the three experimental cases as well as the position of the aluminum inner cylinder. This figure serves as a cross section of what the system will look like at each rotation rate. Fig. 3.7(b) then compares the paraboloidal shape to that of a sphere. Taking the derivative of 3.39 with respect to s, we find

$$\frac{dh}{ds} = \frac{\Omega^2 s}{g_0}, \tag{3.40}$$

From 3.39 and 3.40, we can determine the topographic β-effect for a paraboloid given by

$$\begin{aligned} \beta_{para} = -\frac{2\Omega}{h}\left(\frac{dh}{ds}\right) &= \frac{-2\Omega}{h_0 + \frac{\Omega^2 s^2}{2g}} \frac{\Omega^2 s}{g} \\ &= -\frac{2\Omega}{\frac{gh_0}{\Omega^2} + \frac{s^2}{2}} \\ &= \frac{2\Omega s}{4R_D'|_{h_0}^2 + \frac{s^2}{2}} \end{aligned} \tag{3.41}$$

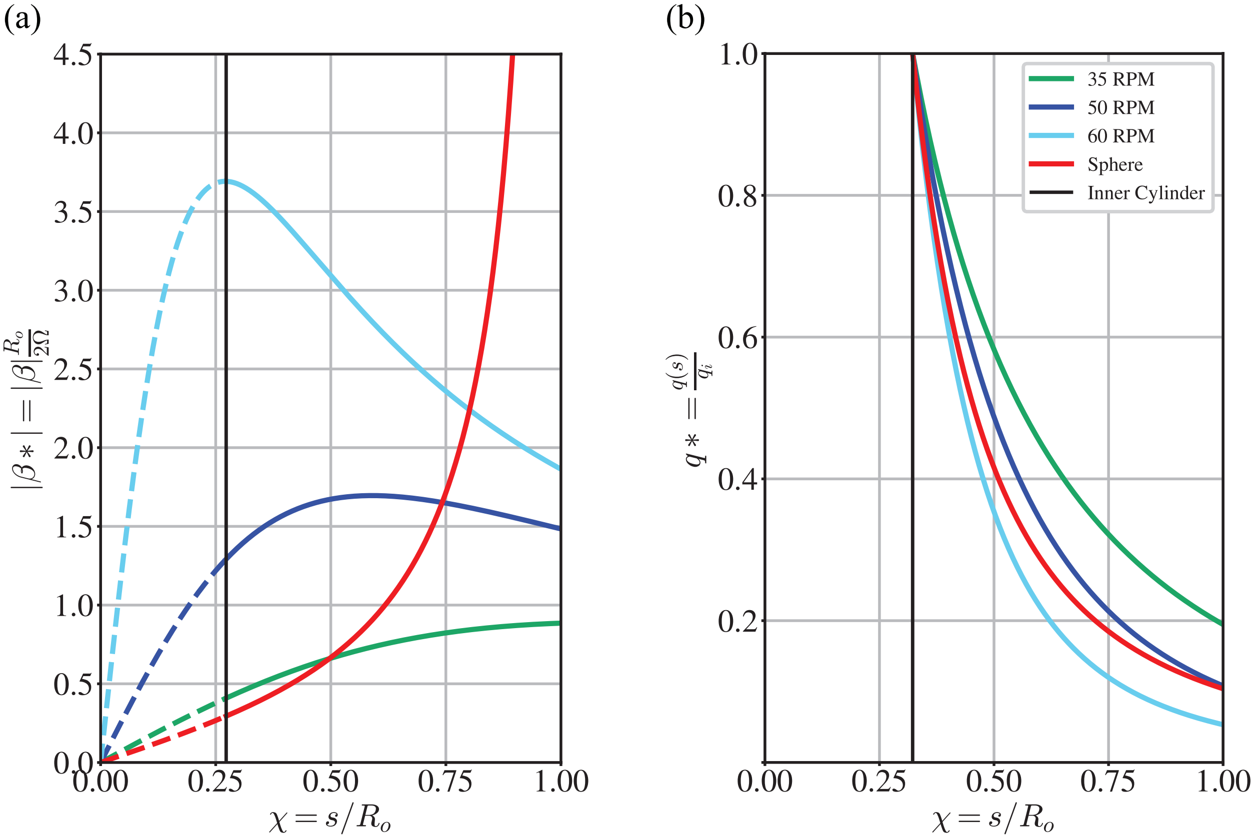

Figure 3.8: (a) Nondimensional topographic beta for paraboloids and sphere. (b) Normalized head flux for paraboloids and sphere.

In 3.41, $R'_D = \sqrt{gh_0}/2\Omega$ is a version of the Rossby deformation radius which describes the scale at which the effects of rotation and inertia near the inner boundary are approximately balanced. Eq. 3.41 can be nondimensionalized by multiplying $R_o/2\Omega$ where R_o is the radius of the tank. This gives a nondimensional β^* that is related to Eq. 3.27 by the relationship

$$\beta^* = \zeta Ro_{\perp}\beta' \tag{3.42}$$

where $\zeta = R_o/(R_o - R_i)$. Using β^* to recast the paraboloidal Eq. 3.41 gives

$$\begin{aligned}\beta^*_{para} &= -\frac{2\Omega s}{4R_D'|^2_{h_0} + \frac{s^2}{2}}\frac{R_o}{2\Omega} \\ &= \frac{sR_o}{4R_D'|^2_{h_0} + \frac{s^2}{2}} \\ &= -\frac{\frac{s}{R_o}}{\frac{4R_D'|^2_{h_0}}{R_o^2} + \frac{s^2}{2R_o^2}} \\ &= -\frac{\chi}{Bu^2 + \chi^2/2}\end{aligned} \tag{3.43}$$

where $\chi = s/R_o$ is a normalized radius and $Bu = R_D'/R_o$ is the Burger number.

The same procedure above can be used to determine the topographic β-effect of a sphere, resulting in the following equation for layer depth:

$$h(s)_{sph} = 2\sqrt{R_o^2 - s^2}. \tag{3.44}$$

Using Eq. 3.44, the topographic β-effect of a sphere is

$$\beta_{sph} = \frac{2\Omega s}{R_o^2 - s^2}. \tag{3.45}$$

We can nondimensionalize eq. 3.45 by multiplying it by $R_o/2\Omega$ which gives

$$\beta^*_{sph} = \frac{\chi}{1 - \chi^2}. \tag{3.46}$$

Fig. 3.8(a) compares the absolute values of the topographic β-effect for the sphere (red) and paraboloid at 35, 50, and 60 RPM (cyan, blue, green respectively). While the topographic β-effect for a parabola differs from that of a sphere, the values are on the same order of magnitude in the bulk of the fluid. In addition, for the lowest rotation rate they share monotonic behaviors. These similarities and the flexibility of the parabolic β-effect with the rotation rate make the parabola an excellent proxy for a sphere. The values of our maximum topographic β for each case is listed in Table 3.4.4.2. Given the dimensions of our system, we are able to reach higher topographic β values than earlier experiments (Matulka et al., 2016; Lemasquerier et al., 2021).

3.3.2 Heat flux

Radially directed buoyancy, characterized by heat flux, is a crucial parameter when comparing the geometries as it ultimately drives the flow. We do a simple comparison of the heat flux profiles by assuming that both the spherical shell and paraboloidal free surface configurations have a fixed buoyancy flux, q_i, at the inner radius, R_i. Then, assuming that there are no sources or sinks in the fluid layer, and Power $= qA =$ constant, we can apply thermal energy conservation to approximate the variation of thermal flux with radius.

For a paraboloidal free surface, the geometry is as follows:

$$2\pi r_i h_i q_i = 2\pi s h(s) q(s), \tag{3.47}$$

into which we can substitute the following quantities:

$$h_i = h_0 + \frac{\Omega^2 R_i^2}{2g}, \tag{3.48}$$

and

$$h(s) = h_0 + \frac{\Omega^2 s^2}{2g}. \tag{3.49}$$

Making the substitutions and rearranging,

$$q(s) = \frac{q_i R_i \Big(h_0 + \frac{\Omega^2 R_i^2}{2g}\Big)}{s\Big(h_0 + \frac{\Omega^2 s^2}{2g}\Big)}. \tag{3.50}$$

The same procedure can be followed to determine the heat flux through the spherical shell, resulting in

$$q(r) = \frac{q_i R_i^2}{r^2}. \tag{3.51}$$

The heat flux of the spherical and paraboloidal geometries are compared in Fig.3.8(b) , and all profiles have a similar decay. This demonstrates the efficacy of using the paraboloid to model the heat flux through a spherical shell.

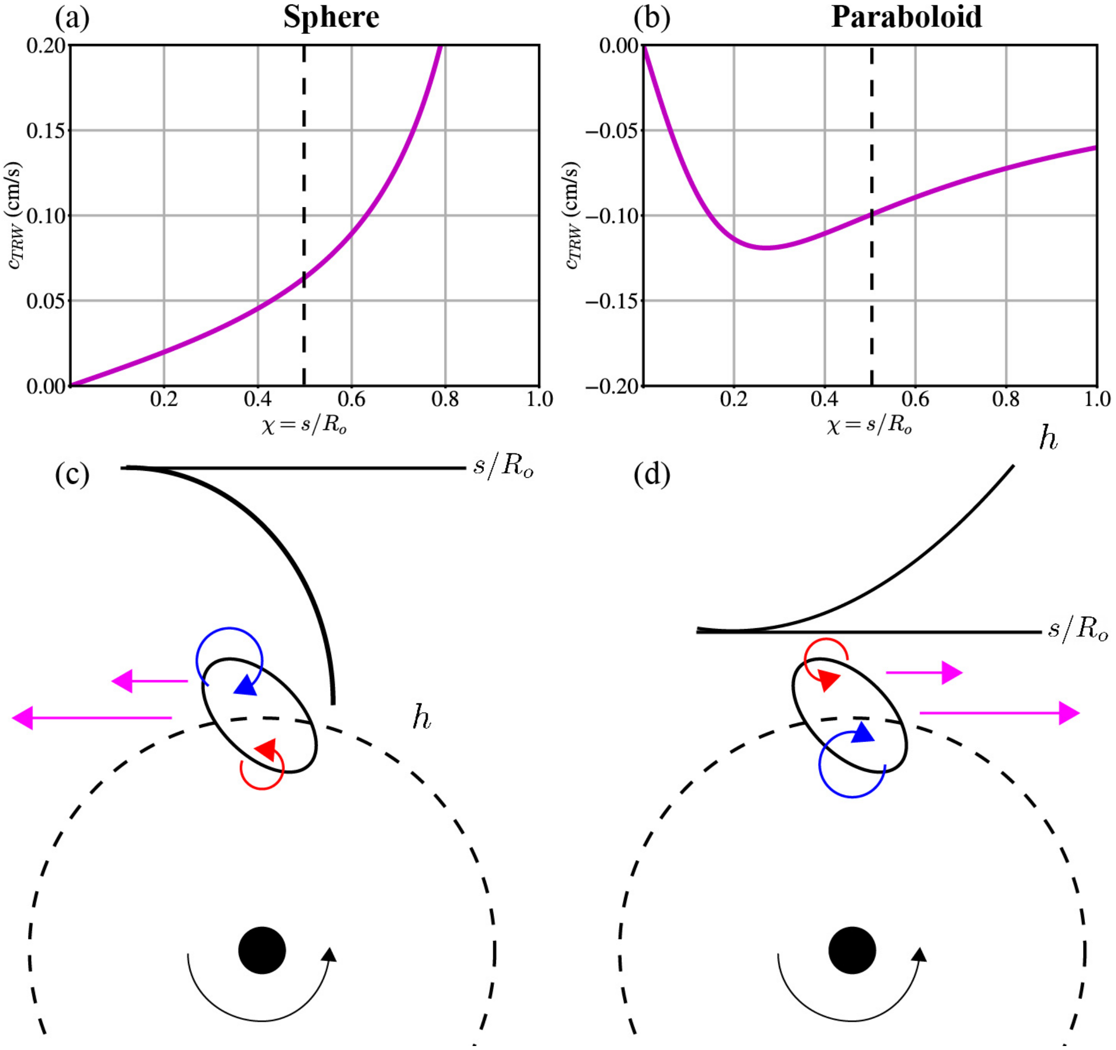

Figure 3.9: The thermal Rossby wave speeds predicted by Eq. 3.63 ($Pr = 3.810$) for a (a) sphere and (b) paraboloid at 60 RPM. Schematics of expected vorticity dynamics given a system with a (c) negative, nonlinear decrease in fluid layer height with radius and (d) a positive, nonlinear increase in fluid layer height with radius. The vortex (solid black line) is fixed at $s/R_o = 0.5$ (black dashed line). The outer edge is compressed (stretched), leading to a negative (positive) vorticity. The inner edge is stretched (compressed), leading to a positive (negative) vorticity. In both cases, the net azimuthal drift velocity will vary in radius (pink arrows).

3.3.3 Vorticity Dynamics

One of the advantages of our experimental device is the paraboloidal free surface, which generates a significant β-effect comparable to that of a deep spherical shell as shown in Sec. 3.3.1. This analogy is important because a certain geometry with fluid layer height $h(s)$ will affect a local column of fluid with some vorticity, ω_0 differently, depending on the geometry. A simplified relationship that describes the induced vorticity by stretching of fluid columns by motion in s is given by

$$\Delta\omega \sim \beta\Delta s, \tag{3.52}$$

where $\Delta\omega$ is the induced vorticity and Δs is the change of the fluid column's radial position.

Let us consider a system with a counter-clockwise background rotation rate, Ω and a gently sloping boundary such that $dh/ds = -B$, where B is a constant, or where the height is decreasing constantly with radius. As a reminder, $\beta \sim -dh/ds$. Thus, when the outer edge of the vortex is compressed (according to Eq. 3.52) the local vorticity relative to the background flow decreases. However, the inner edge of the vortex is stretched, leading to a positive vorticity. The net velocity drift of the vortex, proportional to dh/ds, will then be in the counter-clockwise direction.

For more complex geometries, we turn to Fig. 3.9 which shows a schematic of this process for a sphere versus a paraboloid. Fig. 3.9(a,b) give the Rossby wave speed as a function of nondimensional radius χ for each geometry predicted by Eq. 3.63, which is discussed in greater detail in Sec. 3.4.1. We find that c_{TRW} is positive for the sphere, and negative for the paraboloid. This can be understood by considering the schematics in Fig. 3.9(c,d), which show the vorticity dynamics behind each process at $\chi = 0.5$. In the first case, the outer edge of the vortex is compressed, and according to Eq. 3.52, this will lead to a local decrease of vorticity relative to the background shown by the blue circle. The opposite is true for the inner edge, demarcated by a red circle. The net azimuthal drift (Rossby wave propagation) of the vortex will be in the positive azimuthal direction (pink arrows).

Now, consider a system where the fluid layer height is increasing, rather than decreasing, nonlinearly with radius such as the paraboloid. The outer edge of some vortex will be stretched. According to Eq. 3.52, leads to an increase of vorticity relative to the background shown by the red circle. The opposite will be true for the inner edge. The net azimuthal drift (Rossby wave propagation) of the vortex will be in the negative azimuthal direction direction. For both the paraboloidal and spherical systems, the fluid layer height is changing nonlinearly with radius and we expect structures to drift and tip due with an angle proportional to the second derivative of height with radius (Busse and Hood, 1982).

3.4 Results

Table 3.1: Characteristic dimensional values from each experimental run. Averages are carried out over the last ten minutes wherever applicable. Each row gives the rotation rate Ω, $max(|u_\phi|)$, $\Delta T_\perp$, $\Delta T_\parallel$, and $\langle h \rangle_s$.

Ω (RPM; rad/s)	$max(\lvert u_\phi \rvert)$ (cm/s)	$\Delta T_\perp$ (°) C	$\Delta T_\parallel$ (°) C	$\langle h \rangle_s$ (cm)
$35, 3.7$	0.53	4.19	-10.74	15.76
$50, 5.2$	0.47	6.60	-12.27	14.29
$60, 6.3$	0.49	7.60	-5.02	13.26

We present three natural convection cases at 35, 50, and 60 RPM where we collect UDV velocity profiles, surface thermography, and basal thermometry. Details regarding these cases can be found in Table 3.1, which gives several key measurements that will be used throughout the analysis, and Table 3.2, which gives a more comprehensive list of control parameters and non-dimensional numbers. Given the combination of a geostrophic turbulence and a topographic β-effect, we expect to see several jets in the system following the Rhines scale wavenumber from Eq. 3.2.

Table 3.2: Details of the final ten minutes of each experimental run. Each row gives the rotation rate Ω, fluid layer heights h_0, h_i, h_o at $s = 0$ and inner and outer radii respectively, the ratio $\eta = (h_o - h_i)/(R_o - R_i)$, maximum topographic β, the Ekman number, $Ek = \nu/(2\Omega(R_o - R_i)^2)$ the Rayleigh number given by the radial temperature gradient, $Ra_\perp = ((\alpha \Delta T_s \Omega^2)(R_o - R_i)^4)/(\nu\kappa)$, the Froude number $Fr = (\Omega^2(R_o - R_i))/g$, the Rossby number $Ro = max(u_\phi)/(2\Omega(R_o - R_i))$, the Reynolds number, $Re = max((u_\phi)(R_o - R_i))/\nu$, the baroclinic deformation radius $R_D = \sqrt{\alpha g \Delta T_s \langle h(s) \rangle_s/(2\Omega^2)}$ (Smith et al., 2014), and the zonostrophy index $\mathcal{R}_\beta = L_{Rh}/L_\beta$ where L_β represents the scale above which β-effects impact the energy cascade. If ϵ is the cascade rate, $L_\beta = (\epsilon/\beta^3)^{1/5}$ (Cabanes et al., 2017).

Ω RPM	(h_0, h_i, h_o) cm	η	max(β) cm^{-1}s^{-1}	$Ek/10^{-6}$	$Ra_\perp/10^9$	Fr	$Ro/10^{-3}$	Re	R_D cm	$\mathcal{R}_\beta$
35	$(11.97, 12.96, 21.38)$	0.309	0.174	1.84	0.443	0.37	2.64	1440	0.694	2.22
50	$(6.65, 8.64, 25.60)$	0.622	0.473	1.29	1.41	0.75	1.67	1282	0.584	2.43
60	$(2.06, 4.98, 29.87)$	0.913	1.23	1.07	2.38	1.10	0.57	530	0.499	2.42

3.4.1 Rossby Wave Propagation

Geostrophic turbulence, or that where rotation is the dominant force has been shown to mimic two-dimensional turbulence (Danilov and Gurarie, 2008). However, deviations from geostrophy occur in nearly all geophysical systems. One such phenomena that anistropizes the nearly axially invariant flow through wave propagation, and thus halts the inverse energy cascade is the topographic-β effect. For a deep spherical shell, such as the outer core, $\beta \to \infty$ at the equator, and thus likely has leading order effects on the dynamics.

To clarify how topographic-β breaks the two-dimensionality of the otherwise geostrophic system and excites Rossby waves that propagate anisotropically, we turn to the governing equations of motion in Cartesian coordinates where rotation $\boldsymbol{\Omega} = \Omega\hat{z}$.

$$\frac{\partial \omega}{\partial t} + (\boldsymbol{u}_h \cdot \boldsymbol{\nabla}_h)\omega + \beta u_y = n.c.t., \tag{3.53}$$

and for geostrophic (two-dimensional flows),

$$\omega = \nabla_h^2 \psi, \tag{3.54}$$

where β accounts for an increase in fluid layer height in the $\hat{\boldsymbol{y}}$ direction, ω is the vorticity, ψ is the streamfunction, h is the horizontal directions x and y, and $n.c.t.$ denotes non-conservative terms such as forcing and dissipation. We can rewrite Eq. 3.53 allowing $\boldsymbol{u} = \boldsymbol{U} + \boldsymbol{u}'$ where the background zonal flow $\boldsymbol{U} = U\hat{\boldsymbol{x}}$. Assuming $\boldsymbol{u}' \ll \boldsymbol{U}$ gives Eq. 3.53 becomes

$$\frac{\partial \omega}{\partial t} + U\frac{\partial \omega}{\partial x} + \beta u_y = n.c.t.. \tag{3.55}$$

We can write Eq. 3.62 purely in terms of the streamfunction, which gives

$$\frac{\partial \nabla_h^2 \psi}{\partial t} + U\frac{\partial}{\partial x}\nabla_h^2\psi + \beta\frac{\partial \psi}{\partial x} = n.c.t.. \tag{3.56}$$

Asymmetry in the system is already observed in Eq. 3.110 by the third term on the left hand side, which is only a derivative in x. Furthermore, assuming an unbounded domain and inviscid flow, with a traveling wave solution of the form

$$\psi = \psi_0 e^{i(kx+ly-\sigma t)}, \tag{3.57}$$

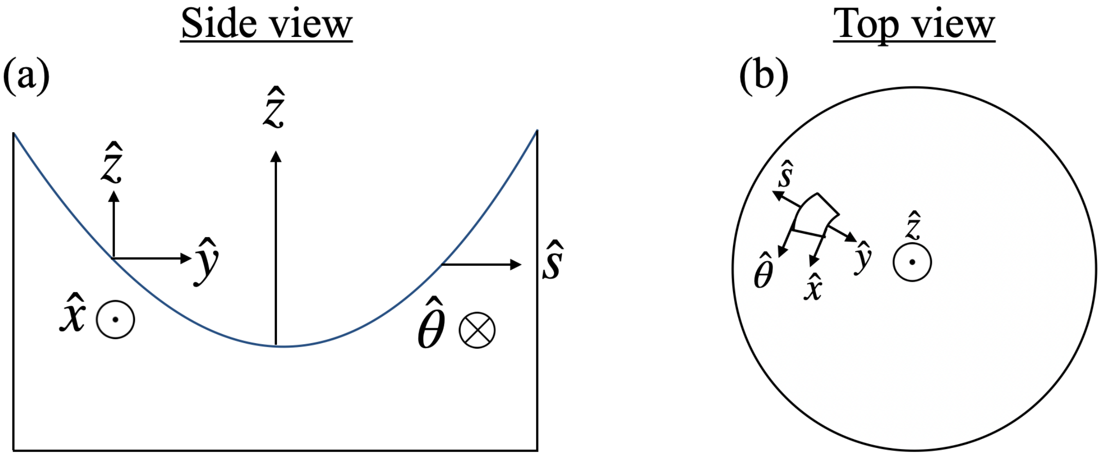

Figure 3.10: (a) Side view of the rotating free surface cylindrical apparatus. The left hand side of the schematic shows the Cartesian coordinates, and the right hand side shows the cylindrical coordinates. (b) Top view of the same system.

where k and l are the wavenumbers in x and y respectively, and σ is the wave frequency. Substituting into a linearized Eq. 3.110 yields the following normal mode dispersion relationship for the barotropic Rossby waves (Vallis, 2006; McWilliams, 2006) Doppler shifted by the advection by the zonal flow

$$\sigma = kU - \beta \frac{k}{(k^2 + l^2)}, \tag{3.58}$$

where σ is the barotropic Rossby wave frequency. From the propagation of barotropic Rossby waves in Eq. 3.58, we observe that the two-dimensional isotropy of the system no longer holds due to the topographic-β effect. We can multiply Eq. 3.58 by a characteristic length scale in x to find the speed of the Rossby waves in the x-direction,

$$c = U - \frac{\beta}{k^2 + l^2} \tag{3.59}$$

where c gives the barotropic Rossby wave phase speed in the x-direction.

We follow (Lemasquerier et al., 2021) to apply Eq. 3.59 and estimate the barotropic Rossby wave phase speed in our system. Because of the strong influence of rotation in this device, we can transform our cylindrical coordinate system to a set of local Cartesian coordinates at a given location in s. In the Cartesian framework, $\phi \to x$ and $s \to y$. The details are given in Fig. 3.10 which illustrates this transformation. In local Cartesian coordinates, $dh/dy < 0$, which yields a positive β. According to Eq. 3.59, we then expect barotropic Rossby waves that propagate in the retrograde direction. In addition, we can simplify Eq. 3.59 by assuming the structures will be similar in length scale in the azimuthal and radial directions, which gives

$$c = U - \frac{\beta}{k^2 + l^2} \approx \frac{-\beta}{2k^2}. \tag{3.60}$$

Noting that the background zonal flow in our system is the time-averaged azimuthal velocity such that $U \approx \langle u_\phi \rangle_t$ gives

$$c = \langle u_\phi \rangle_t - \frac{\beta}{2k^2}. \tag{3.61}$$

The time average $\langle u_\phi \rangle_t$ is carried out over the 400 second Hovmöller window.

We force our system through buoyancy gradients that rely on the thermal field. Therefore, we may expect thermal Rossby waves (TRW) rather than the barotropic Rossby waves. In this case, the axial vorticity equation is given by

$$\frac{\partial \omega}{\partial t} + U\frac{\partial \omega}{\partial x} + \beta u_y = \alpha \Omega^2 \frac{\partial T}{\partial x}. \tag{3.62}$$

This is coupled to the temperature evolution equation given by Eq. 3.4. The linear stability analysis for this set up was carried out by Busse and Or (1986); Busse (2004), where a phase speed for thermal Rossby waves is found to be

$$c_{TRW} = \langle u_\phi \rangle_t - \frac{1}{(1 + Pr(T))}\left(\frac{\beta}{2k^2}\right). \tag{3.63}$$

In this case, $Pr(T)$ is the Prandtl number as a function of temperature. Now it is possible to use Eq. 3.63 in local Cartesian coordinates to calculate the thermal Rossby wave phase speed expected at a given radius. We choose $\Gamma = 0.5$, where Γ is introduced for gap position, the normalized position from the inner cylinder radius, R_i to the tank radius, R_o. The azimuthal wavenumber, k, is then measured by taking an FFT of the thermal anomaly in azimuth over time at fixed radius $\Gamma = 0.5$. Fig. 3.11(a,b) shows this FFT for the 50 and 60 RPM cases respectively. The peak of the FFT is demarcated by a black dashed line and $k/2\pi = 0.141\text{cm}^{-1}$ for the 50 RPM case, and $k/2\pi = 0.262\text{cm}^{-1}$ for the 60 RPM case.

In addition for the 50 RPM case, we find $\langle u_\phi \rangle_t = 0.08871$ cm/s for the background zonal flow, and use the Prandtl number at the fluid's mean temperature of $T = 48.5629$°C, which gives $Pr = 3.5527$. For the 60 RPM case, these values are $\langle u_\phi \rangle_t = -0.16145$ cm/s and using a mean fluid temperature of $T = 44.8377$°C gives $Pr = 3.8310$. All Prandtl number values used in this calculation are provided by UCLA Ph.D. student Jewel Abbate. Fig. 3.11(c,d) give Hovmöller diagrams of the thermal anomalies in time and ϕ where the green, black, and pink lines now correspond to the phase speeds found using Eq. 3.63. This range of slopes show good agreement with the phase speed of the measured waves, demonstrating that we likely have a variety of Rossby waves excited in our system.

Using the wavenumber values from each FFT, we can also find the wavelength of the structures using

$$\lambda = \frac{2\pi}{k}, \tag{3.64}$$

and the length scale of the structures

$$\ell = \frac{\lambda}{2} = \frac{\pi}{k}. \tag{3.65}$$

This yields $\lambda_\phi = 7.41; \ell_\phi = 3.70\text{cm}$ and $\lambda_\phi = 4.25; \ell_\phi = 2.13\text{cm}$ for the 50 and 60 RPM cases respectively. These values will be useful in Sec. 3.4.4, where we compare length scales measured in the device to theoretical predictions.

3.4.2 Rhines Scale Jets

The topographic Rossby waves discussed in Sec. 3.4.1 likely drive the alternating prograde-retrograde jets observed in the 35, 50, and 60 RPM cases. Another question to consider is at which length scale will the topographic β-effect impact the inverse energy transfer typical of two dimensional turbulence. To characterize this scale, we can return to Eq. 3.110 and take

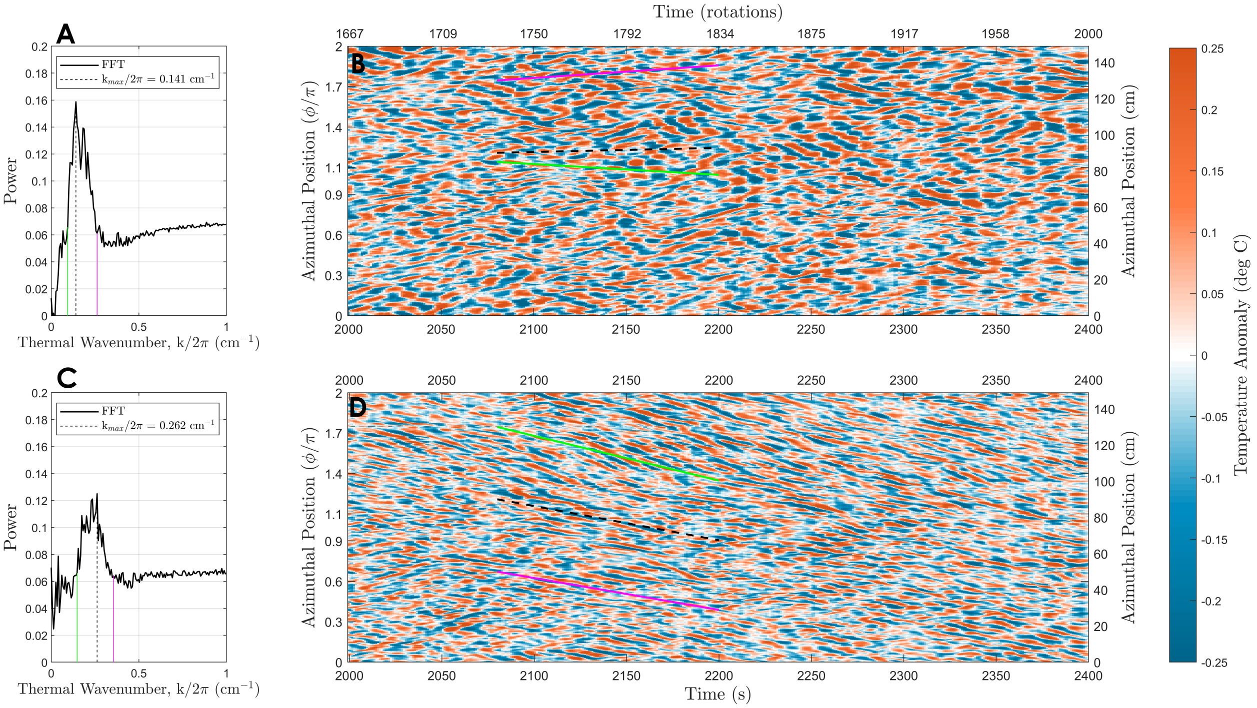

Figure 3.11: Temperature anomaly in azimuth at mid-gap position, $\Gamma = 0.5$, for ((a), (b)) 50 RPM and ((c), (d)) 60 RPM cases. The temperature anomaly is calculated such that $\Delta T = T(\phi, t) - \langle T(t) \rangle_\phi$. (a) and (c) show the respective peak wavelengths when an FFT is taken over the azimuth and detrended. (b) and (d) are bandpass filtered from 0.03cm^{-1} to 0.35cm^{-1}. The dashed black lines represent the theoretical stationary thermal Rossby phase speed from Eq. 3.63. $c_{50} = -0.055$cm/s and $c_{60} = -0.225$cm/s. Variations in experimental phase speed can be attributed to the thickness of the peaks in both cases, which are denoted with pink and green lines.

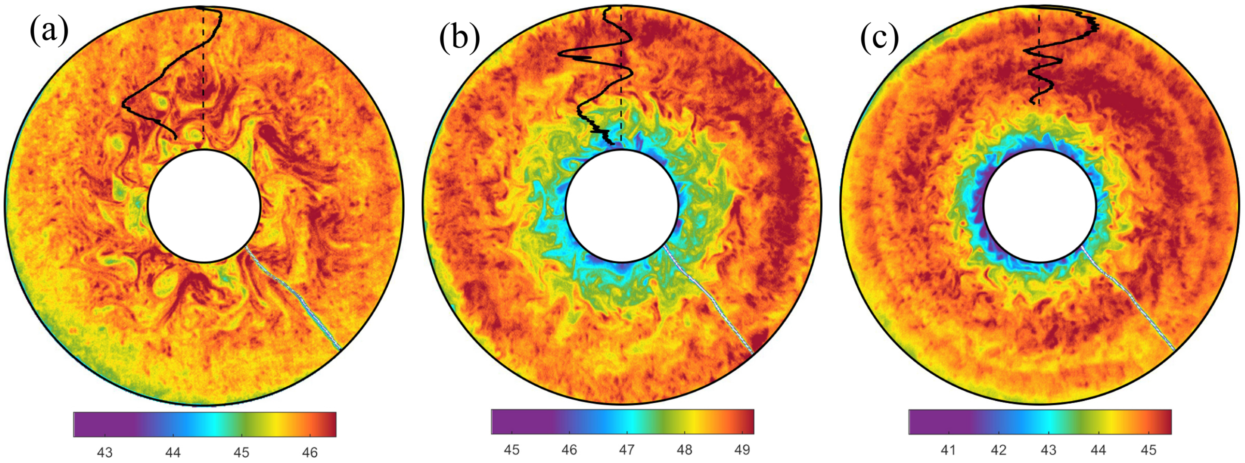

Figure 3.12: Figure from T. Lonner. IR Snapshots of the thermal field mid-case for (a) 35 RPM, (b) 50 RPM, and (c) 60 RPM. Color denotes temperature in degrees Celsius. Video clips corresponding to each of these cases are available in the supplement. Overlayed at 3 O'Clock in each image is the time-averaged azimuthal UDV velocity data from the last 10 minutes of each case. The dashed black line signifies where velocity is zero. In (a), the cooler region in the lower left of is an artifact caused by the IR camera being slightly off-center. In (c), the ring at around $\Gamma = 3/4$ is due to reflections from the white tarp that covers the device. The white line in the bottom right of each image the wire of a thermistor crossing over the tank and can be disregarded.

the ratio of the inertial to topographic β terms. Noting that $J(\psi, \nabla_h^2 \psi) \sim U^2/L^2$ and $\beta(\partial\psi/\partial x) \sim \beta U$ (where U, L are characteristic velocity and length scales respectively) we find

$$L_{Rh} \sim \sqrt{\frac{U}{\beta}}, \tag{3.66}$$

first noted by (Rhines, 1975). More accurately, L_R is the length scale of a jet, or half a wavelength λ_{Rh} given by

$$\lambda_{Rh} = \frac{2\pi}{k_{Rh}}, \tag{3.67}$$

where k_{Rh} is the Rhines wavenumber. Therefore,

$$L_{Rh} = \pi\sqrt{\frac{2U}{\beta}}. \tag{3.68}$$

where a factor of $\sqrt{2}$ is often included in the numerator of (3.68) in the literature and demonstrates its approximate nature Heimpel and Aurnou (2007). For scales $L < L_{Rh}$, advection dominates whereas at $L \geq L_{Rh}$, Rossby wave propagation dominates. The length scale of zonal jets emerging from this system has been proposed to be L_{Rh}.

An additional scale of importance can be found by equating a turbulent eddy-turnover timescale $\tau_t = \epsilon^{-1/3}k^{-2/3}$, where ϵ is the rate of upscale energy transfer within the turbulent energy cascade and k is a wavenumber, to a Rossby wave timescale $\tau_w = k/\beta$. This gives the scale

$$L_\beta = \left(\frac{\epsilon}{\beta^3}\right)^{1/5} \tag{3.69}$$

and is often thought of as the threshold of turbulence anisotropisation owing to the β effect. Taking the ratio of (3.66) and (3.69) characterizes the magnitude of the flow anisotropy and the strength of the resulting jets. It is the zonostrophy index Lemasquerier et al. (2021)

$$\mathcal{R}_\beta = \frac{L_{Rh}}{L_\beta} = \beta^{1/10}(U)^{1/2}\epsilon^{-1/5} \approx \left(\frac{\beta U}{\Omega^2}\right)^{1/10}\left(\frac{h^2 Ek}{(R_o - R_i)^2}\right)^{-1/10}. \tag{3.70}$$

where ϵ is estimated from the rate of energy loss due to dissipation, $\epsilon \approx U^2/\tau_E$ and $\tau_E = (h/(R_o - R_i))(2E)^{-1/2}\Omega^{-1}$ is the Ekman spin-down time scale written in terms of Ek.

A regime of strong jets typically occurs when the Rossby waves are separated from the final jet scale, or where the zonostrophy index $\mathcal{R}_\beta > 2.5$. Fig. 3.13 shows $\mathcal{R}_\beta$ throughout the fluid layer, and Table 3.4.4.2 gives the average value for our three cases. In all cases, we find that we are close to this threshold and likely in a regime of moderate to strong jets.

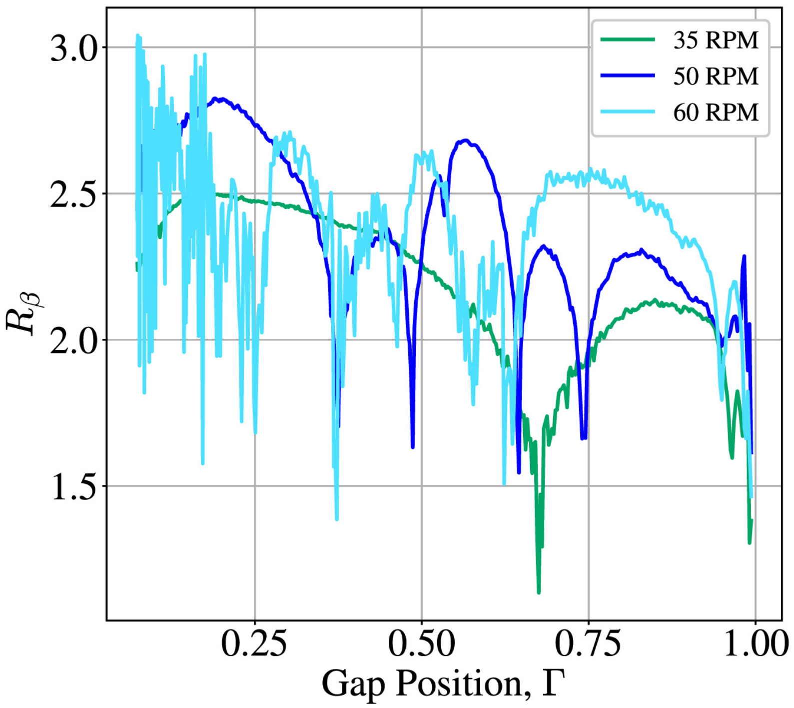

Figure 3.13: Zonostrophy index, according to Eq. 3.70, for the three cases throughout the fluid layer.

Fig. 3.12 shows snapshots of the surface thermal fields for each case. The azimuthal velocity is time-averaged over the last ten minutes of each run and overlayed at the top of the snapshots, indicated by the solid black line. For the 35 RPM and 50 RPM cases, there is a net prograde drift, whereas the 60 RPM case has a net retrograde drift. The difference in drift direction may be, in part, due to migrating jets in the 60 RPM case (discussed further in Sec. 3.4.3). The system is potentially transient and a longer experimental run may show the jets stabilizing with a prograde drift like the other two cases. The net azimuthal drift observed in Fig. 3.12(a,b) could be a thermal wind effect driven by a lateral buoyancy gradient (Aurnou et al., 2003). Regardless of the background drift, the zonal flow profile in all cases is dominated by alternating prograde and retrogrades jets. The width of the jets, L_J, in each case can be measured and compared to the Rhines jet width prediction, L_{Rh}.

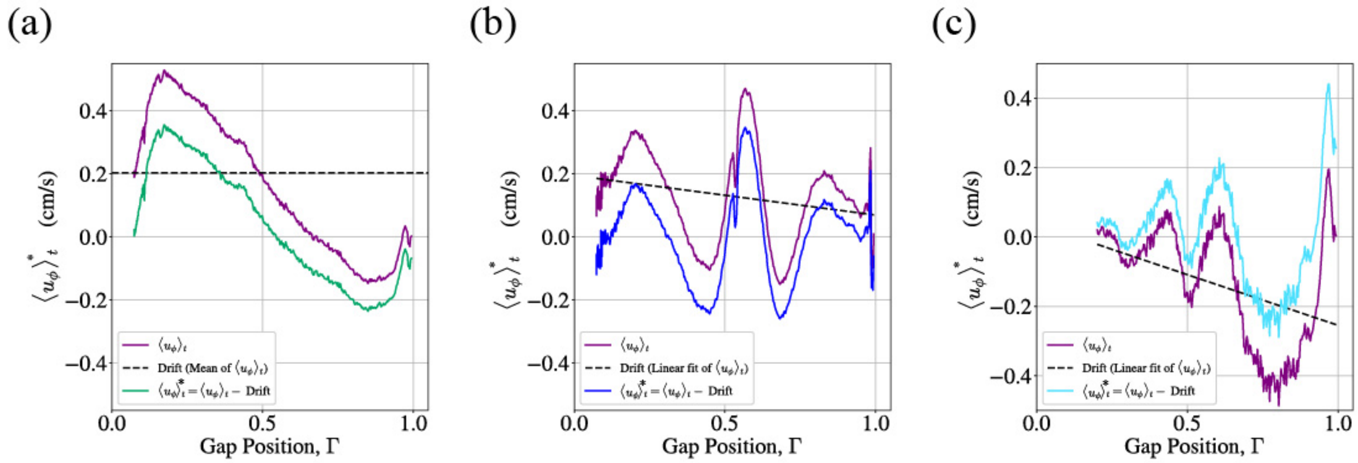

Figure 3.14: Time averaged zonal flow profiles for (a) 35 RPM (b) 50 RPM and (c) 60 RPM. Time averages were carried out for the last ten minutes of data. The black dashed line in each panel shows the velocity that is subtracted from each profile to correct for drift. The green, blue, and cyan lines then show each corrected zonal flow profile.

The process to measure the width of the jets is as follows: first, the net azimuthal drift is subtracted from the zonal flow profiles given by the black solid lines in Fig. 3.12. For the 35 RPM case, this amounts to removing the mean drift speed, whereas the 50 RPM and 60 RPM cases require a subtraction of a linear fit of the velocity profile due to asymmetries in the zonal flow behavior with radius. Fig. 3.14(a,b,c) shows these corrected zonal flows for each case. Next, we find the radial locations at which the corrected zonal flow profiles cross zero, not including noise in the signal near the inner and outer boundaries. Subtracting the jet's start point from the jet's point gives the radial length scale of each measured jet, L_J in terms of the gap width, Γ. We find two jets in the 35 RPM case, five jets in the 50 RPM case, and six jets in the 60 RPM case, all of varying length scales.

The next step of the process is to calculate the theoretical Rhines scale prediction, L_{Rh} using Eq. 3.68 for each jet, given a velocity scale U and a value of β. The jets are most accurately represented by their peak velocity. Thus, we choose the scale $U \sim max(u^*_\phi)$ within each jet. This value is shown as purple solid lines in Fig. 3.15 We also use the value of β

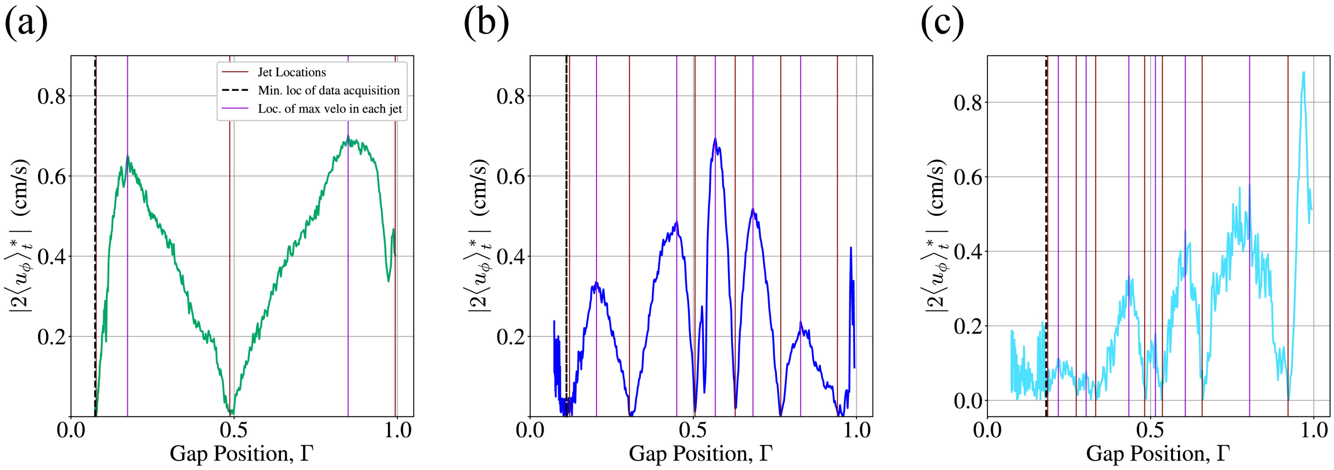

Figure 3.15: The absolute value of the corrected zonal flows for (a) 35 RPM (b) 50 RPM and (c) 60 RPM. The locations of the start and end points of each jet are given in solid maroon lines. The start point is subtracted from the end point to give L_J for each jet. In addition, to calculate L_{Rh}, we use the maximum of the corrected velocity within each jet. This is shown in a purple line.

corresponding to that same location, which are given in Fig. 3.16 with purple solid lines. These two quantities can be used to compute L_{Rh} for each jet.

Fig. 3.17(a,b,c) now give the measured jet width (blue dashed line) and the theoretical Rhines jet width (black dashed line) for the 35, 50, and 60 RPM cases respectively in terms of the gap width. The solid points are shown at the locations of the midpoint of each jet. We can see that $L_J \approx L_{Rh}$, especially for the 50 and 60 RPM cases near mid-shell. Finally, fig. 3.17(d) gives L_J/L_{Rh} for all three cases in green, blue, and cyan. We find good agreement between the measured jet width and the Rhines scale prediction of the jet width, with the best agreement for the 50 RPM case ($\langle L_J/L_{Rh} \rangle = 1.52$). The average ratio for the 35 RPM case is $\langle L_J/L_{Rh} \rangle = 1.81$, and the average ratio for the 60 RPM case is $\langle L_J/L_{Rh} \rangle = 1.93$. The average ratio for all three cases, 1.75, is indicated by the black dashed line. For all cases and radial locations, L_J/L_{Rh} remains fixed near unity, indicating that the jets observed in

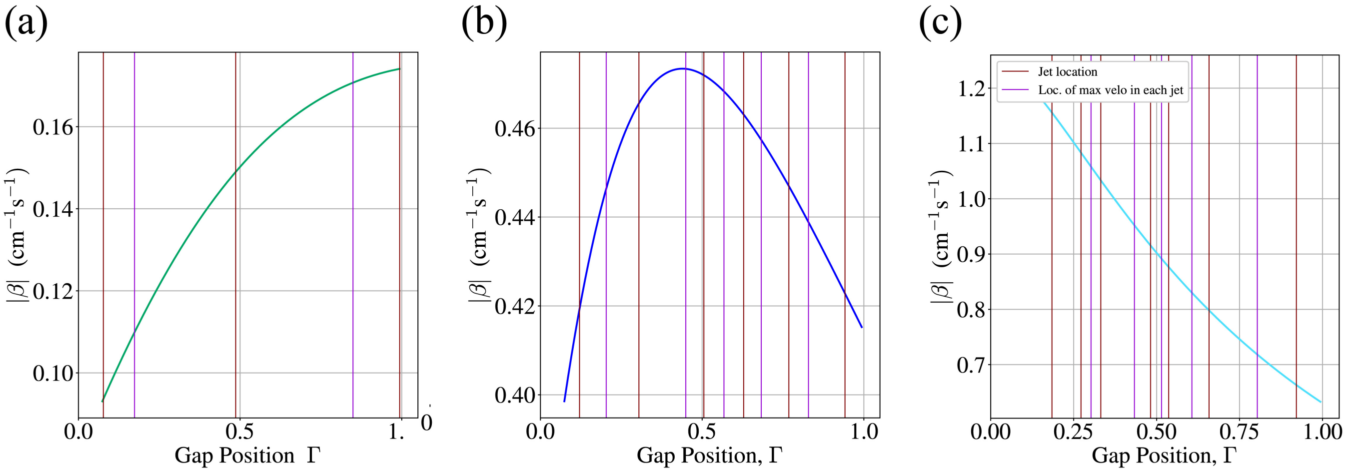

Figure 3.16: The absolute value of topographic-β for (a) 35 RPM (b) 50 RPM and (c) 60 RPM. The locations of the start and end points of each jet are given in solid maroon lines. To calculate L_{Rh}, we use the maximum of the corrected velocity within each jet. This is shown in a purple line. Then, the value of $|\beta|$ used to calculate L_{Rh} is the value at the same location of the maximum of the corrected velocity within each jet.

our system follow the Rhines scale.

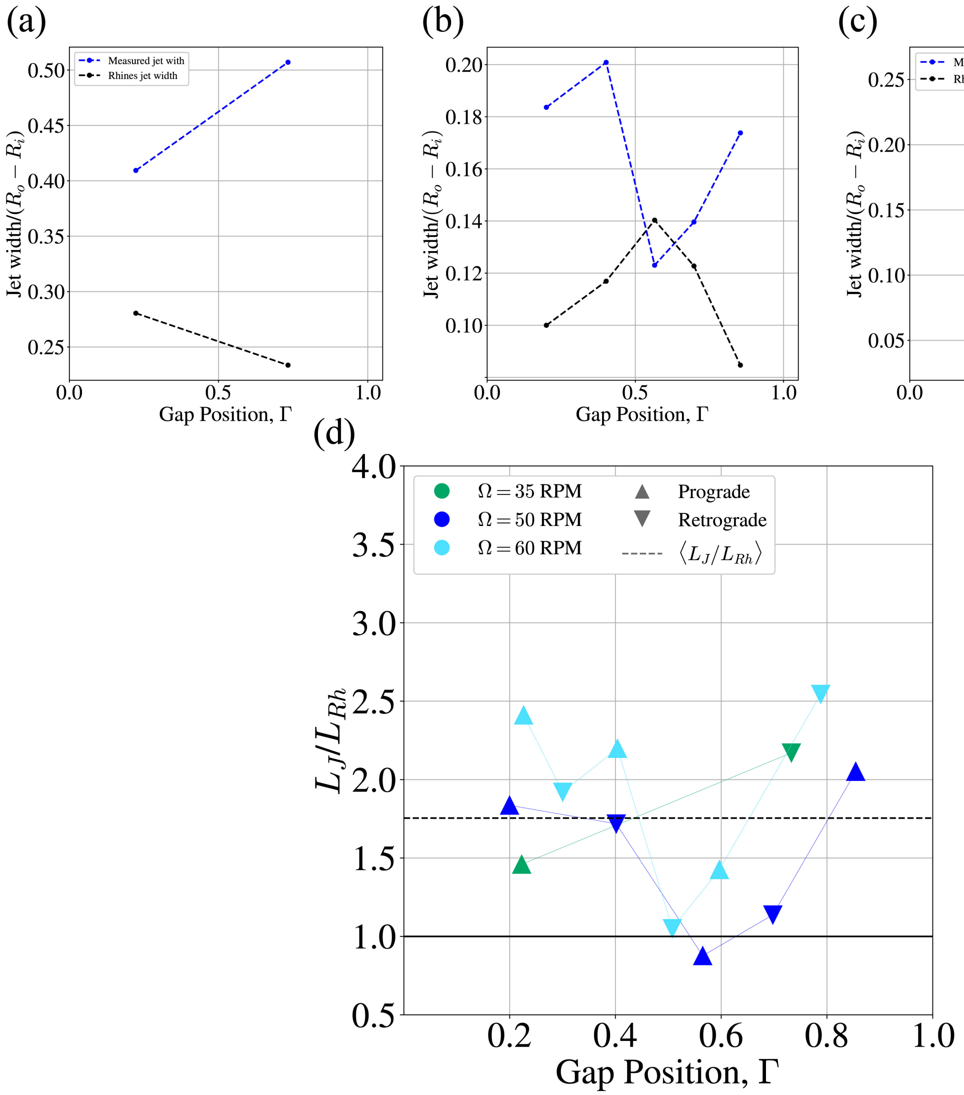

Figure 3.17: Measured jet width, L_J (blue dashed line) versus the theoretical Rhines jet width, L_{Rh} using Eq. 3.68 (black dashed line) for (a) 35 RPM (b) 50 RPM and (c) 60 RPM. The solid points are shown at the locations of the midpoints of each jet. The ratio L_J/L_{Rh} for all three cases is given in (d), where a solid black line shows where the ratios are equal and the black dashed line gives $\langle L_J/L_{Rh} \rangle$ averaged over all jets and for all three cases.

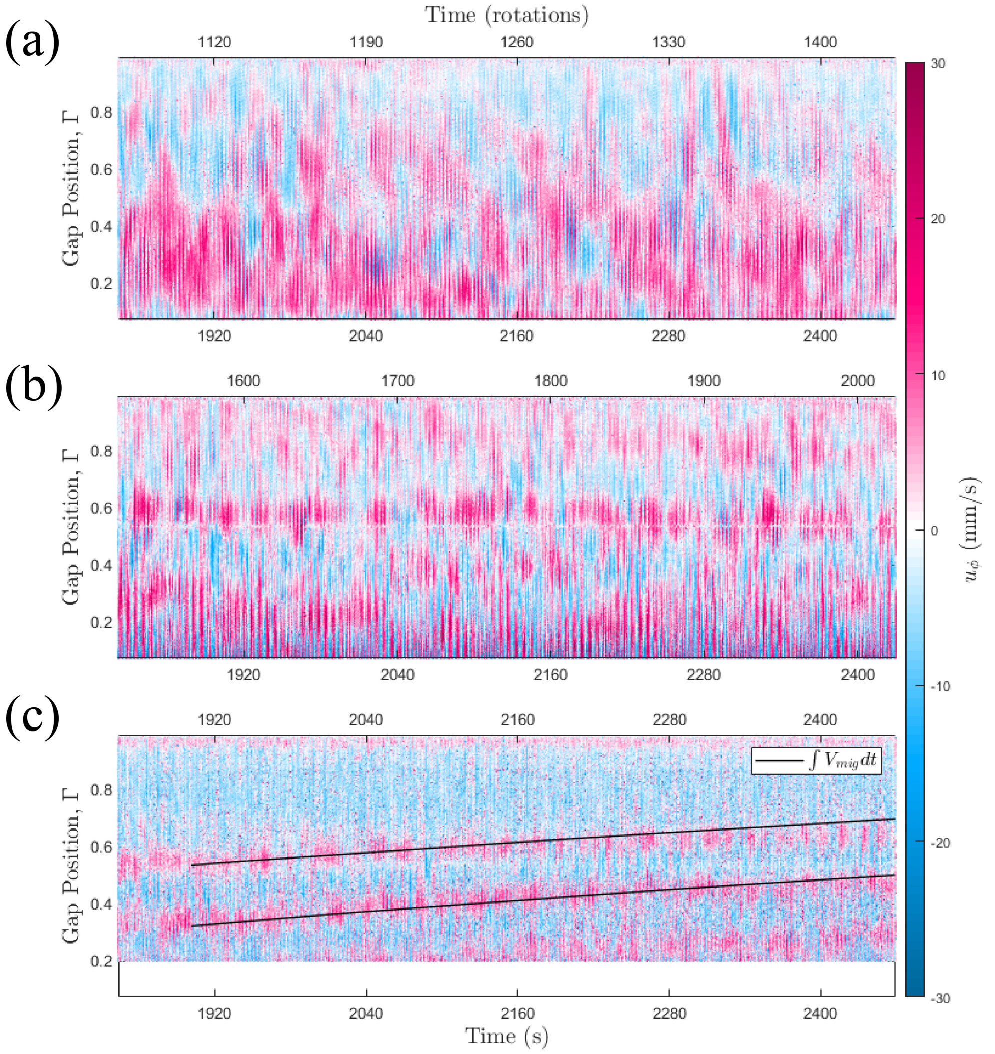

Figure 3.18: Azimuthal UDV velocity data from cases at (a) 35 RPM, (b) 50 RPM, and (c) 60 RPM. Time is presented in both seconds (bottom axis) and rotations periods (top axis) from the beginning of the experiment. Pink represents prograde motion while blue is retrograde motion. In subplot (b), the striping is due to aliasing since the Doppler frequency surpasses the Nyquist limit. This can be resolved in future experiments by adjusting the settings on the UDV. (c) only presents data from 0.2 onwards due to the paraboloidal free surface dipping below the height of the UDV transducers.

3.4.3 Jet Migration

The latitudinal propagation of zonal jets, also known as jet migration, has been observed in a variety of geophysical and astrophysical fluid systems or models of these systems. Examples include Earth's troposphere and ocean, and the Jovian atmosphere (Riehl et al., 1950; Williams, 2003; Chan et al., 2007; Smith et al., 2014; Chemke and Kaspi, 2015; Ashkenazy and Tziperman, 2016). Jet migration has also been observed in our paraboloidal convection system.

Fig. 3.18(a,b,c) shows Hovmöller diagrams of the azimuthal Doppler velocimetry data for the 35, 50, and 60 RPM respectively. In all cases, alternating bands of prograde (pink) and retrograde (blue) jets are observed. However, in the 60 RPM case in particular, several of the jets meander in the positive Γ direction, which we will quantify in this section. The mechanisms responsible for jet migration remain an open question, but some possibilities are eddy momentum flux convergence (Chan et al., 2007; Young et al., 2019), and poleward bias in baroclinicty (Chemke and Kaspi, 2015).

Another concept was proposed by (Cope, 2021), who carried out a series of two dimensional, double periodic computational models on a β-plane to investigate the conditions under which jet migration may occur. Both quasilinear models, in which nonlinear interactions between certain modes are restricted, and fully nonlinear models were run. Jet migration was found to occur in models that included nonlinear interactions between low wavenumber and high wavenumber modes. The underlying dynamical mechanism was proposed to be these nonlinear interactions that force Rossby wave propagation with a background shear in latitude ("zonons"). These zonons were further associated with the meandering of the jets. In the same study, a function for the translation speed of a migration jet, V_{mig} was found through empirical analysis. In the analysis it is assumed that

$$V_{mig} \sim F(\beta, \mu, \epsilon, k_f, k_{jet}) \tag{3.71}$$

where μ is a frictional damping rate, ϵ is an energy dissipation rate, k_f is the forcing wavenumber, and k_{jet} is the wavenumber that gives the number of jets in the domain. This relationship is assumed because variations in flow morphologies can be typically attributed to changes in these parameters. To determine the function, F, that relates measurable parameters with V_{mig}, (Cope, 2021) noted that V_{mig} is related to the jet RMS velocity by $U_{rms} = \sqrt{\epsilon/\mu}$. To find what controls the quantity $\sqrt{\epsilon/\mu}$, the zonostrophy index $\mathcal{R}_\beta$ is used, which measures the strength of the jet solutions. An equation for $\mathcal{R}_\beta$ as previously stated is given by $\mathcal{R}_\beta = L_{Rh}/L_\beta$. where L_β represents the scale above which β-effects impact the energy cascade. If ϵ is the energy dissipation rate, this quantity can be rewritten as $L_\beta = (\epsilon/\beta^3)^{1/5}$ (Cabanes et al., 2017). The zonostrophy index can then be expressed differently as

$$\mathcal{R}_\beta = \frac{\epsilon^{1/20}\beta^{1/10}}{2^{1/2}\mu^{1/4}} \tag{3.72}$$

The value $V_{mig}/\sqrt{\epsilon/\mu}$ was then plotted against the zonostrophy index for a series of simulations with varying numbers of jets, and a ${\mathcal{R}_\beta}^{-5}$ scaling is found. Using this scaling leads to the relationship

$$V_{mig} \sim \frac{\mu^{3/4}\epsilon^{1/4}}{\beta^{1/2}} \sim \mu L_{Rh}. \tag{3.73}$$

In the Coreaboloid system, a sensible value for the damping rate μ is the inverse of the Ekman drag timescale such that

$$\mu = \frac{1}{\tau_{Ek}}, \tag{3.74}$$

which gives the following relationship for the jet migration velocity

$$V_{mig} \sim \frac{L_{Rh}}{\tau_{Ek}}. \tag{3.75}$$

Here, $Ek_l = \nu/(2\Omega h^2)$ is the local Ekman number. In the following section, we employ Eq. 3.75 to predict the radial translation of a jet in time, and compare this prediction to Doppler velocimeter data.

3.4.3.1 Finding Paraboloidal V_{mig} and Comparing to Doppler velocimeter data

Staring with Eq. 3.75, some specifications can be made for our paraboloidal system. First,

$$L_{Rh} \sim \sqrt{\frac{U}{\beta_{para}}} \tag{3.76}$$

where β_{para} is given by Eq. 3.41. Making the substitution leads to an equation for L_{Rh} specific to the paraboloidal geometry

$$L_{Rh} = \sqrt{\frac{Ug(h_0 + \frac{\Omega^2 s^2}{2g})}{2\Omega^2 s}}. \tag{3.77}$$

Furthermore, τ_{Ek} is given by Eq. 3.34. In Ek, we use the local fluid layer height given by Eq. 3.39 such that

$$\tau_{Ek} = (2Ek_l)^{-1/2}\Omega^{-1} = (2^{-1/2})\Big(\frac{\nu}{2\Omega h(s)^2}\Big)^{-1/2}\Omega^{-1} = h(s)(\nu\Omega)^{-1/2}. \tag{3.78}$$

Substituting these quantities into Eq. 3.75 and simplifying yields a relationship for the jet migration velocity

$$V_{mig} = \sqrt{\frac{\nu U g}{2\Omega^2 s\Big(h_0 + \frac{\Omega^2 s^2}{2g}\Big)}}. \tag{3.79}$$

This equation gives a method to find how a jet core's radial position, s varies in time. However, since the right hand side of Eq. 3.79 also depends on s, it is necessary to integrate this equation to find the relationship between s and t. In order to find the equation to integrate, we carry out the following steps. Eq. 3.79 can be rewritten as ds/dt such that

$$\frac{ds}{dt} = V_{mig} = \sqrt{\frac{\nu U g}{2\Omega^2 s\Big(h_0 + \frac{\Omega^2 s^2}{2g}\Big)}}. \tag{3.80}$$

Rearranging Eq. 3.80 gives

$$\int_{s_1}^{s_2} \sqrt{\frac{2\Omega^2 s\Big(h_0 + \frac{\Omega^2 s^2}{2g}\Big)}{\nu U g}} ds = \int_{t_1}^{t_2} dt, \tag{3.81}$$

where s_1, t_1 are the initial radial location and point in time of the jet respectively, and $s_2 - s_1$ is the new radial location after time step $t_2 - t_1$. We can further simplify Eq. 3.81 by allowing $C = (2\Omega^2 h_0)/\nu U g$ and $D = \Omega^4/(\nu U g^2)$ which gives

$$\int_{s_1}^{s_2} \sqrt{Cs + Ds^3} ds = \int_{t_1}^{t_2} dt. \tag{3.82}$$

The left hand side of Eq. 3.82 cannot be expressed analytically with ease and thus calls for numerical integration. Before carrying out the numerical integration, we specify a handful of constants used to calculate C and D. First, we will carry out this integration for two jets in the 60 RPM case that have the clearest radial migration. By observation of Fig. 3.18(c), this is (counting all prograde/retrograde jets from the inner boundary) jet numbers three and number five. We also allow the characteristic velocity, U to be the maximum of the time averaged, corrected zonal flow for each jet, which can be found from the data shown in Fig. 3.14(c). This gives $U = 1.5$ cm/s for jet three, and $U = 2.3$ cm/s for jet five. In addition, h_0 can be calculated through Eq. 3.39, which gives 2.06 cm. Finally, s_1 gives the initial radial location of each jet. We choose to begin the integration at $t_1 = 1900$. By using the data shown in Fig. 3.18(c), we find $s_1 = 0.331\Gamma$ (jet three) and $s_1 = 0.536\Gamma$ (jet five). A

After specifying the values of C and D, we are able to numerically integrate Eq. 3.82. The steps to carry this out are below.

1. Evaluate the left hand side of Eq. 3.82 with integral bounds $s_1 + \Delta s$ where Δs is a small step size. To do this, we chose to use the Python function scipy.integrate.quad, which computes the definite integral with specific bounds using quadrature methods. This gives the time step dt required to advance $s_1 + \Delta s$ in space.

2. Use the equation $ds = V_{mig} dt$ to update the spatial step, Δs.

3. Compute $s_1 = s_1 + \Delta s$, and repeat the process until $s_1 + \Delta s$ is equal to the approximate final location of the jet.

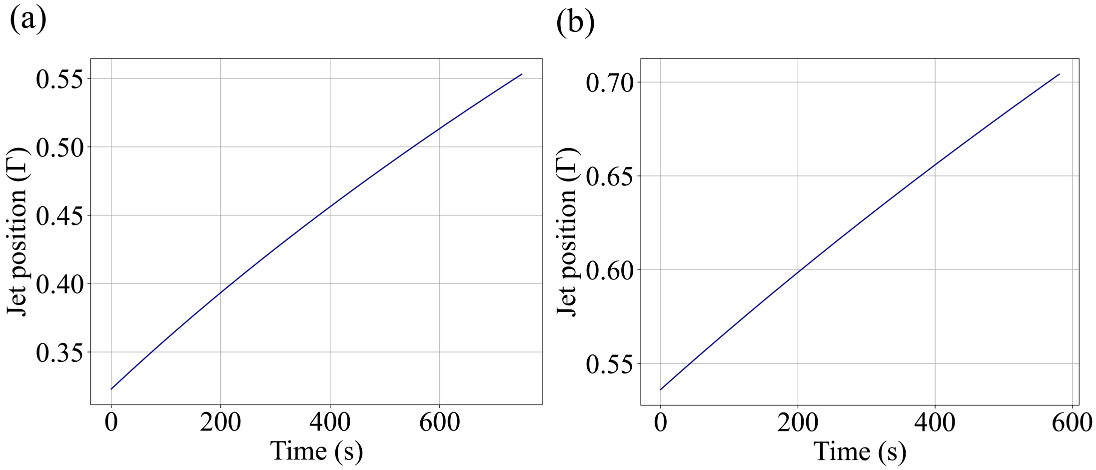

Figure 3.19: Result of integration of the equation derived for jet migration, V_{mig} given by Eq. 3.82 for the 60 RPM case. (a) jet three and (b) jet five (jet numbers are found by counting all prograde and retrograde jets starting at the inner boundary). The functions give the radial movement of the jet core in time, and can be compared to the Doppler velocimetry data.

At each iteration, values of s and t are saved. Fig. 3.19(a,b) give the results of the integration for jet three (left panel) and jet five (right panel). According to these functions, each jet should migrate about $0.15-0.20$ of the gap width in about $600-700$ seconds. These functions are also shown as the black solid lines in Fig. 3.18(c). We observe that the lines closely track the radial movement of the jet core in each case. Appendix D gives the integration script that carries out these steps for jet three in the 60 RPM case.

This shows that the jet migration is well captured by Eq. 3.79, which is based on a key physical assumption. Following (Cope, 2021), through which Eq. 3.79 was found, this migration may be attributed to internal dynamics through nonlinear eddy interactions, rather than an external symmetry breaking mechanism as previously proposed (such as geometrical effects due to sphericity or localization of baroclinicity). In addition, upon observation of Eq. 3.79, we note several other interesting features. First, the speed of the migration increases as $U^{1/2}$ implying that stronger jets likely migrate at a faster speed. In addition,

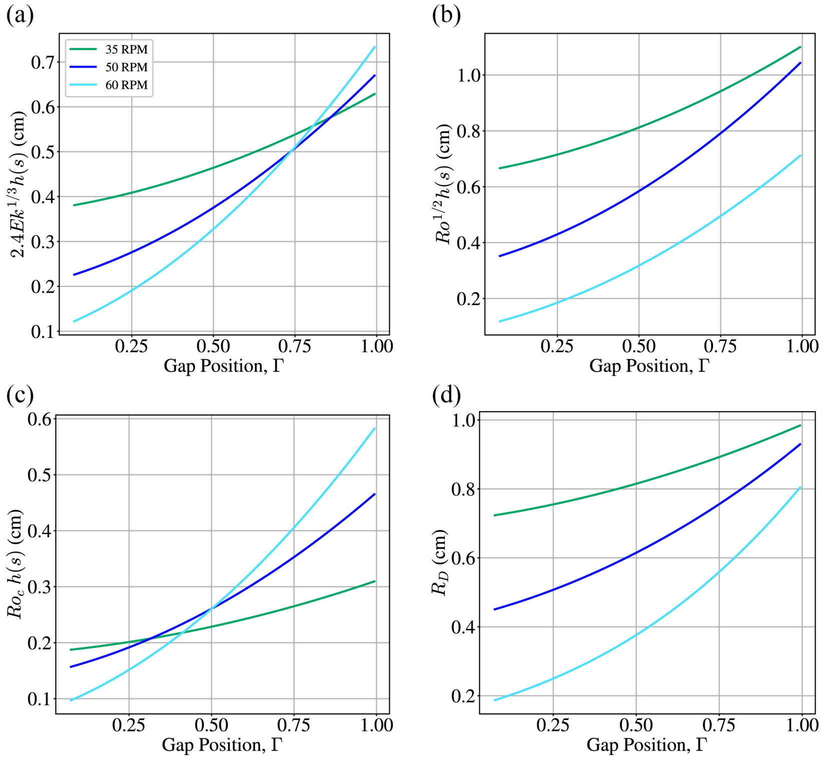

Figure 3.20: Testing predicted length scales for comparison with the measured l_ϕ. In each panel, the green line corresponds to the 35 RPM case, the blue line corresponds to the 50 RPM case, and the cyan line corresponds to the 60 RPM case. (a) $2.4Ek^{1/3}h(s)$, (b) $Ro^{1/2}h(s)$, (c)$Ro_c h(s)$ and (d) R_D.

the jet migration velocity is inversely proportional to the rotation rate Ω which suggests that rotation dampens such lateral motions. Finally, the geometry of the system does play a crucial rose in the migration speed which is inversely related to the fluid layer depth. In a system where $dh/ds > 0$, such as the paraboloidal geometry studied here, we may expect slower migration velocities near the outer boundary.

3.4.4 Length Scale Analysis

The connection between length scales observed in the geomagnetic field and the length scales of core flow remains an open question (Cardin and Olson, 1994; Aurnou et al., 2015;

Aubert et al., 2017; Guervilly et al., 2019). Comparing the characteristic length scales of flows found in this study to those found theoretically by leading order force balances could elucidate which forces and scales are dominant in Earth's core at low latitudes. As stated, geophysical flows are often strongly constrained by rotation. By examination of Eq. 3.7, a dominance of the Coriolis term leads to a balance between pressure and Coriolis,

$$2\Omega\hat{\boldsymbol{z}} \times \boldsymbol{u} = -\frac{1}{\rho_0}\nabla P. \tag{3.83}$$

also known as geostrophic balance. Taking the curl of 3.83 we find,

$$\frac{\partial \boldsymbol{u}}{\partial z} = 0, \tag{3.84}$$

which is known as the Proudman-Taylor theorem. According to Eq. 3.84, we expect that Coriolis dominated flows will be invariant along the axis of rotation and extend across the fluid layer in the axial direction. Therefore, we are mainly interested in length scales perpendicular to the axial direction, which we call "horizontal."

Flows that depart from geostrophic balance are often called quasigeostrophic (QG), and different forces in Eq. 3.7 are able to balance Coriolis depending on the system. In this section, we compare the scale l_ϕ calculated through the thermal IR data in Sec. 3.4.1 to several different theoretical horizontal length scales, and discuss these implications for core flow.

3.4.4.1 Coriolis balanced with viscosity

In this section, we consider the case where viscosity is at leading order, along with Coriolis. In order to find the length scale at which viscosity balance can balance the Coriolis term in the horizontal direction, we can take the curl of geostrophic balance, Eq. 3.83 with the addition of the viscous term. This leads to

$$2\Omega\frac{\partial \boldsymbol{u}}{\partial z} \sim \nu\nabla^2\omega. \tag{3.85}$$

where $\omega = \boldsymbol{\nabla} \times \boldsymbol{u}$ is the vorticity. Then, the component of Eq. 3.85 in the $\hat{\boldsymbol{z}}$-hat direction is

$$\frac{\partial u_z}{\partial z} \sim \frac{\nu}{2\Omega} \nabla^2 \omega_z \tag{3.86}$$

where u_h denotes a typical horizontal velocity and l_h denotes a typical horizontal length scale. Scaling and solving for l_h gives

$$l_h \sim Ek^{-1/3} \mathcal{L}, \tag{3.87}$$

where $\mathcal{L}$ is a characteristic scale. Eq. 3.87 gives a viscous, QG length scale, and has been shown to be the predicted characteristic length scale of rotating convection at the onset of convection, where convection first manifests as elongated, columnar structures (Chandrasekhar, 1961).

Furthermore, in the rapidly rotating limit where $Ek \rightarrow 0$, linear stability analysis shows that

$$l_h = 2.4 Ek^{1/3} \mathcal{L}, \tag{3.88}$$

for plane layer geometries (Chandrasekhar, 1961; Julien and Knobloch, 1998). Similar scalings have been observed in a number of studies of rotating convection in various geometries, including spherical systems (Busse, 1976; Zhang and Schubert, 2000; Dormy et al., 2004).

Fig. 3.20(a) shows this scaling, $2.4Ek^{1/3}h(s)$ where we use the height of the fluid layer as the characteristic length scale, $\mathcal{L}$ for the 35, 50, and 60 RPM cases (green, blue, cyan). We find that the greatest percentage in increase of predicted horizontal length scale, l_h, occurs for the 60 RPM case. The third column of Table 3.3 then gives $2.4Ek^{1/3}h(s)|_{\Gamma=0.5}$. We choose $\Gamma = 0.5$ because l_ϕ was measured at that radial location. When comparing l_ϕ to $2.4Ek^{1/3}h(s)|_{\Gamma=0.5}$, we find that the theoretical prediction according to this balance between viscosity and Coriolis yields a predicted scale about a factor of ten smaller than the measured value. Thus, the thermal structures are likely not controlled by viscosity and we continue to seek additional scaling that may explain the measured horizontal length scales.

3.4.4.2 Coriolis balanced with inertia

Instead if it is inertia that balances Coriolis we find

$$2\Omega\frac{\partial \boldsymbol{u}}{\partial z} \sim \boldsymbol{u}\cdot\boldsymbol{\nabla}\boldsymbol{\omega}. \tag{3.89}$$

Eq. 3.89 can be scaled to give

$$\frac{2\Omega U}{\mathcal{L}} \sim \frac{U^2}{l_h^2}, \tag{3.90}$$

which can be rearranged to give,

$$\frac{l_h}{\mathcal{L}} \sim \left(\frac{U}{2\Omega\mathcal{L}}\right)^{1/2} \sim Ro^{1/2}. \tag{3.91}$$

Solving for l_h gives

$$l_h \sim Ro^{1/2}\mathcal{L}. \tag{3.92}$$

Note that this scaling depends on an output parameter, the velocity scale U. We can formulate the velocity scale U in terms of control parameters by using the free fall velocity that arises from balancing inertia with centrifugal buoyancy (given in Eq 3.9). Using this in the Rossby number gives a parameter known as the convective Rossby number

$$Ro_c = \frac{\sqrt{\alpha\Delta T_{\perp}\Omega^2(R_o-R_i)^2}}{2\Omega(R_o-R_i)} = \frac{\sqrt{\alpha\Delta T_{\perp}}}{2}. \tag{3.93}$$

In the rapidly rotating limit (Guervilly et al., 2019; Aurnou et al., 2020)

$$Ro^{1/2} \sim Ro_c. \tag{3.94}$$

Therefore we will also calculate

$$l_h \sim Ro_c\mathcal{L}, \tag{3.95}$$

to characterize the length scale that comes from a balance between Coriolis and inertia.

Fig. 3.20(b) shows Eq. 3.92 where we use the height of the fluid layer as the characteristic length scale, $\mathcal{L}$ and the maximum value of u_ϕ for each case as the characteristic velocity scale. These values are given in Table . Similar to Fig. 3.20(a), the predicted length scale increases with radial position, though the curves for the various rotation rates do not intersect. The fourth column of Table 3.3 then gives $Ro^{1/2}h(s)|_{\Gamma=0.5}$. Comparing l_ϕ to $Ro^{1/2}h(s)|_{\Gamma=0.5}$ shows that the theoretical prediction according to this balance between inertia and Coriolis again gives a predicted scale about a factor of ten smaller than the measured value. We can also test the length scales predicted by Eq. 3.95.

Fig. 3.20(c) shows Eq. 3.95, where we use the height of the fluid layer as the characteristic length scale, $\mathcal{L}$. The predicted length scales for the three cases are nearly equivalent and cross near the mid shell. This is verified through Table 3.3, where $Ro_c h(s)|_{\Gamma=0.5}$ varies between 0.217 and 0.233 cm. These values are also an order of magnitude less than l_ϕ. We also observe that l_ϕ decreases with increasing rotation rate, which is not reflected in $Ro_c h(s)|_{\Gamma=0.5}$. Thus, the thermal structures are likely not controlled by inertia. We continue to seek additional scaling that may explain the measured horizontal length scales.

3.4.4.3 The Rossby Deformation Radius

The flows in this system are baroclinic, and may be governed by BCI as discussed in Sec. 3.1.2. Therefore, the dominant horizontal length scale that manifests may not be those discussed previously in this section, but rather the Rossby deformation radius, R_D (Chelton et al., 1998; Smith et al., 2014; Nurser and Bacon, 2014). To calculate the R_D, we use Eq. 3.31 with $\mathcal{L} = h$ and note that the Brunt-Väisälä frequency, N, has contributions form both lab gravitational acceleration and centrifugal acceleration where,

$$N = N_{lab} + N_{cent}. \tag{3.96}$$

We can express the lab gravitational acceleration as

$$N_{lab} = \sqrt{-\frac{g}{\rho_0}\frac{\partial p}{\partial z}}. \tag{3.97}$$

where p is the dynamic pressure. To simplify Eq. 3.99, we apply the Boussinesq approximation where $\rho = \rho_0(1 - \alpha\Delta T_{\|})$ where ρ_0 is the background density. We also assume hydrostatic balance, and dynamic pressure gradients are then related to the temperature by

$$\frac{\partial p}{\partial z} = \alpha \Delta T_{\parallel} g. \tag{3.98}$$

Substituting Eq. 3.98 into Eq. 3.99 gives

$$N_{lab} = \sqrt{\frac{\alpha g \Delta T_{\parallel}}{h}}. \tag{3.99}$$

where the vertical gradient has been scaled by h. The same can be carried out for the centrifugal acceleration,

$$N_{cent} = \sqrt{-\frac{\Omega^2 s}{\rho_0}\frac{\partial p}{\partial s}}, \tag{3.100}$$

where the dynamic pressure is related to the temperature by

$$\frac{\partial p}{\partial s} = \rho_0 \alpha \Delta T_{\perp} \Omega^2 s. \tag{3.101}$$

After substitution of Eq. 3.101 into Eq. 3.102, we find

$$N_{cent} = \sqrt{\frac{\alpha \Omega^2 s \Delta T_{\perp}}{(R_o - R_i)}}, \tag{3.102}$$

where the radial gradient has been scaled by $R_o - R_i$. Finally, inserting Eq. 3.99 and Eq. 3.102 into Eq. 3.96 gives

$$R_D = \frac{(N_{lab} + N_{cent})h}{2\Omega} = \sqrt{\frac{\alpha h^2}{4\Omega^2}\Big(\frac{g\Delta T_{\parallel}}{h} + \frac{\Omega^2 s \Delta T_{\perp}}{(R_o - R_i)}\Big)}. \tag{3.103}$$

Eq. 3.103 gives the Rossby deformation radius for a system with both lab and centrifugal acceleration. Fig. 3.20(d) shows the $R_D l$ as a function of fluid layer height, h for each case. At a given radial location, the Rossby deformation radius decreases with rotation rate. Column six of Table 3.3 gives $\langle R_D \rangle_s$, and when comparing to l_ϕ, we again predict that structures should be about an order of magnitude finer in scale.

Thus far, it is unclear which physical mechanisms sets the horizontal scale of the structures. Future iterations of this project will improve length scale measurements and explore additional avenues to explain the trends observed in the data.

Table 3.3: Comparing the measured horizontal length scale, l_ϕ, to theoretical predictions. All length scales are in centimeters.

Ω (RPM)	l_ϕ	$l = 2.4Ek^{1/3}h(s)\|_{\Gamma=0.5}$	$l = Ro^{1/2}h(s)\|_{\Gamma=0.5}$	$l = Ro_c h(s)\|_{\Gamma=0.5}$	$\langle R_D \rangle_s$
35	5.32	0.464	0.813	0.217	0.81
50	3.70	0.375	0.585	0.233	0.61
60	2.13	0.328	0.318	0.217	0.38

3.4.4.4 Stewartson Boundary Layers

Fluid systems often include boundary layers, which are relatively sharp hydrodynamic, thermal, or magnetic gradients that exist to satisfy a given set of boundary conditions. For example, no-slip conditions due to a solid surface top and bottom surfaces generally result in steep gradients in the velocity field whose thickness scales as

$$\delta_\nu \sim Re^{-1/2}\mathcal{L}, \tag{3.104}$$

where δ_ν is known as the viscous boundary layer. As the strength of inertia grows relative to viscosity, the thickness of the viscous boundary layer decreases. For turbulent flows, the narrow width of viscous boundary layers can be challenging to resolve both numerically and in the laboratory.

In our system, we are able to capture a different type of boundary layer, known Stewartson boundary layers which arise in rotating flows with rigid sidewalls (Stewartson, 1957; Friedlander, 1980; Kunnen et al., 2013; Vogt et al., 2021). The thickness of one of these layers is given by

$$\lambda_s = Ek^{1/4}\mathcal{L}. \tag{3.105}$$

Within this shear layer, there is a secondary circulation unique from the bulk in which there is a change in angular velocity. In our device, we are able to resolve the Stewartson layers near the outer boundary by measuring the azimuthal velocity with the Doppler velocimeter.

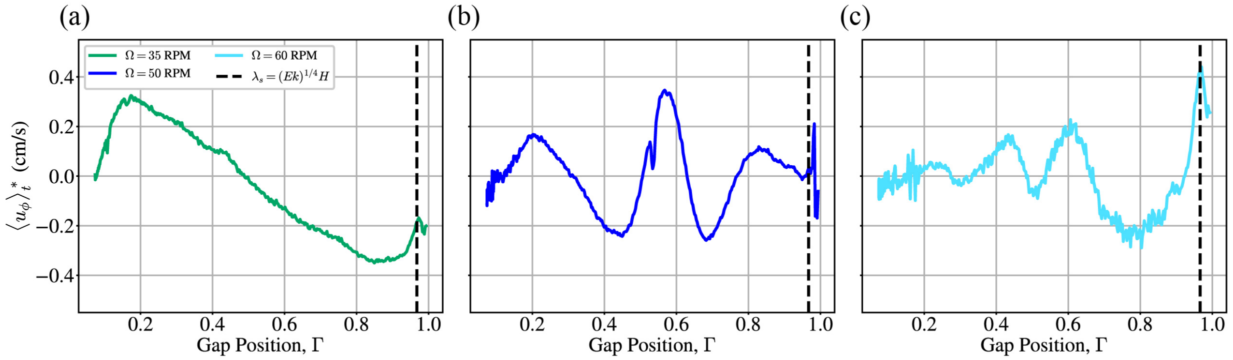

Figure 3.21: Time averaged zonal flow profiles, where the black dashed line corresponds to the location of the Stewartson boundary layer given the relationship $\lambda_s = (Ek)^{1/4}H$, where H is the fluid layer height at the outer boundary. The panels correspond to the rotation rates where (a) 35 RPM, (b) 50 RPM, and (c) 60 RPM.

Fig. 3.21(a,b,c) give the time averaged zonal flow profiles for the 35, 50, and 60 RPM cases respectively. We choose the fluid layer height at the outer boundary, H, as the characteristic length scale because we are measuring the Stewartson layer thickness at this outer wall. The black dashed line in each panel demarcates this value $\lambda_s = Ek^{1/4}H$. Fig. 3.21(a) (35 RPM) shows an increase in the zonal flow at λ_s relative to the retrograde jet. Fig. 3.21(b) (50 RPM) shows a peak in the zonal flow after the last prograde jet at λ_s. And Fig. 3.21(c) (60 RPM) also shows a peak in the zonal flow at λ_s after the last retrograde jet. Thus, in all cases we find a distinct shift in the zonal flow velocity at the predicted Stewartson boundary layer thickness demonstrating good qualitative agreement with this theoretical value.

3.4.5 Groundwork for Future Computational Models

Concurrence between experiments and direct numerical simulations (DNS) can offer a broad understanding of the dynamics that may not be realized with one method independent of the other. Fully three-dimensional DNS calculations of core flow are computationally expensive, owing to the range of length scales needed to resolve the thin Ekman boundary layers up to domain-scale structures. To this end, we began developing a quasi-geostrophic (QG), paraboloidal thermal convection model based on the spherical shell models of Calkins et al. (2012b) and Calkins et al. (2012a). This section serves to lay the groundwork for possible future paraboloidal, QG models.

3.4.5.1 Overview of Spherical Shell Quasigeostrophic Convection Models

QG theory is formally derived as an asymptotic limit of the governing equations where the Rossby number approaches zero (Vallis, 2006; McWilliams, 2006). In this limit, the Coriolis force is leading order and balanced only by pressure gradients, giving vertically constrained (columnar) flow. Following this, the physical idea of the QG convection model in a deep fluid layer with sloping boundaries is to account for stretching and compression of columns as they move radially, inducing local vorticity and generating topographic Rossby waves (see Sec. 3.4.1). It is therefore only rigorously valid when β is small (Busse, 1970).

Fig. 3.22, adapted from Aubert et al. (2003) gives a schematic of a QG spherical shell convection model, where the fluid motions are solved only in the equatorial plane (yellow) while accounting for the interactions of convection columns with the sloping boundaries of the domain (blue). And despite limitations to the strength of buoyancy relative to rotation in this framework, comparison between QG DNS and laboratory experiments of convection in a spherical shell have shown good agreement (Aubert et al., 2003; Dormy et al., 2004; Gillet et al., 2007). Furthermore, QG models are limited in that they cannot fully capture heat flow within a spherical shell. To this end, Busse (1970) and Glatzmaier and Olson (1993) have demonstrated that the cylindrical component of buoyancy is the dominant driver of convection in the region outside of the tangent cylinder parallel to the equatorial plane. Therefore, the QG model is a valuable tool that can be used to simulate convection in Earth's core, while being computationally tractable.

Next, we discuss the governing equations and numerical methods of the spherical shell quasigeostrophic convection by Calkins et al. (2012b), which we will adapt for a paraboloidal

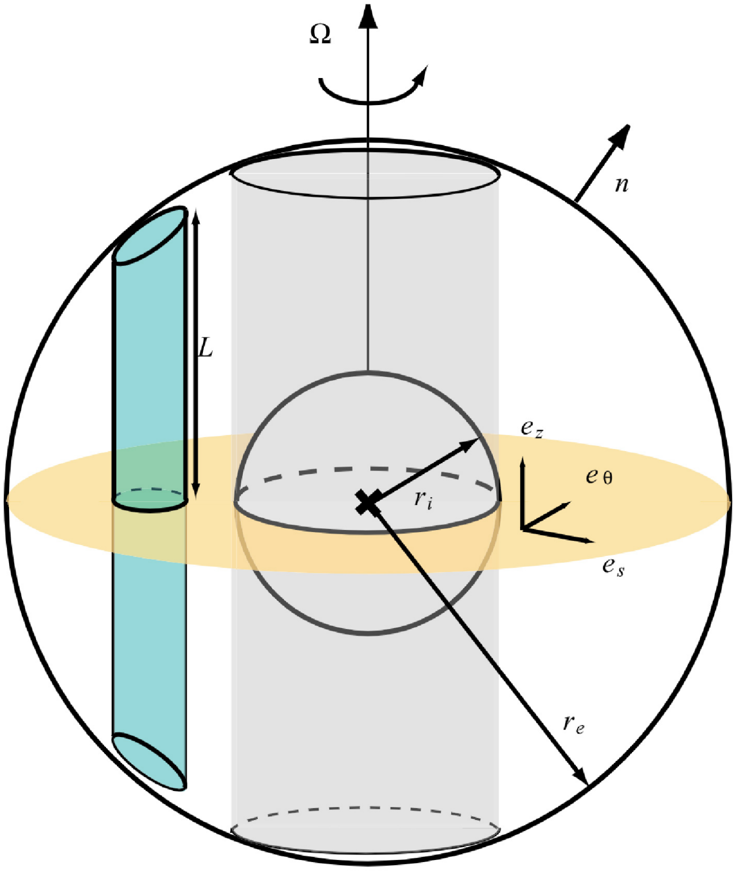

Figure 3.22: Figure adapted from (Aubert et al., 2003). Schematic depicting the spherical shell quasi-geostrophic convection model, which uses a cylinder coordinate system. In this model, the fluid motions are solved in the equatorial plane (yellow), but account for the stretching and compression of axial convection columns (blue). The model does not solve for motion inside the tangent cylinder (grey).

geometry. This model employs a vorticity-streamfunction method to capture the fluid behaviour in a slice parallel to the equatorial plane. Gravity is linearly dependent on the cylindrical radius $\boldsymbol{g} = -g\hat{\boldsymbol{s}}$, and the conductive temperature profile is given by $T_c = ln(s/s_o)/ln(R_i/s_o)$ where s_o is the nondimensional outermost (cylindrical) radius, R_i is the radius of the inner boundary, and R_o is the radius of the outer (spherical) boundary. The nondimensional scales are, a length scale of $d = R_o - R_i$ and thermal diffusion time scale of $\tau_\kappa = d^2/\kappa$. The QG Boussinesq governing equations for vorticity (ω), the streamfunction (ψ), velocity (u_s, u_ϕ, u_z), and thermal energy are (Calkins et al., 2012b; Schaeffer and Cardin, 2005)

$$\frac{1}{Pr}\Big(\frac{\partial\omega}{\partial t} + u_s\frac{\partial\omega}{\partial s} + \frac{u_\phi}{s}\frac{\partial\omega}{\partial\phi}\Big) = \frac{2}{Ek}\frac{\partial u_z}{\partial z} - Ra\frac{\partial T}{\partial\phi} + \nabla^2\omega, \tag{3.106}$$

$$\nabla^2\psi = -\omega, \tag{3.107}$$

$$u_s = \frac{1}{s}\frac{\partial\psi}{\partial\phi}, u_\phi = \frac{-\partial\psi}{\partial s}, \tag{3.108}$$

and

$$\Big(\frac{\partial T}{\partial t} + u_s\frac{\partial T}{\partial s} + \frac{u_\phi}{s}\frac{\partial T}{\partial\phi}\Big) = -u_s\frac{\partial T}{\partial\phi} + \nabla^2 T. \tag{3.109}$$

The control parameters are the Rayleigh number (Ra), the Prandtl number (Pr), and the Ekman number (Ek) as previously defined. The boundary conditions are no slip at $s = R_i$ and $s = R_o$, leading to

$$\frac{\partial\psi}{\partial s}(R_i,\phi) = \frac{\partial\psi}{\partial s}(s_o,\phi) = 0. \tag{3.110}$$

Equation 3.110 can be reformulated in terms of Dirichlet boundary conditions by considering the volumetric flow rate per axial depth (Calkins et al., 2012b; Peyret, 2002)

$$\psi(R_i,\phi) - \psi(s_o,\phi) = -\int_{R_i}^{s_o}\langle u_\phi\rangle ds, \tag{3.111}$$

where $\langle\rangle$ denotes an azimuthal average. For simplicity, we set $\psi(R_i,\phi) = 0$ and have

$$\psi(s_o,\phi) = \int_{R_i}^{s_o}\langle u_\phi\rangle ds, \tag{3.112}$$

as a boundary condition on the streamfunction. To calculate $\langle u_\phi \rangle$, we take the ϕ component of the momentum equation and average over ϕ, obtaining (Calkins et al., 2012b; Peyret, 2002)

$$\left(\frac{1}{Pr}\right)\left(\frac{\partial \langle u_\phi \rangle}{\partial t} + u_s \frac{\partial \langle u_\phi \rangle}{\partial s} + \left\langle \frac{u_\phi u_s}{s} \right\rangle\right) = -\frac{2}{Ek}\langle u_s \rangle + \nabla^2 \langle u_\phi \rangle - \frac{\langle u_\phi \rangle}{s^2}. \tag{3.113}$$

We begin the numerical portion of this study by validating the QG spherical shell thermal convection code originally developed by M. Calkins. To do this, we perform four fully nonlinear simulations, and compare to Calkins et al. (2012b). We calculate the time-averaged Nusselt number, time-averaged convective Reynolds number, and time-averaged zonal Reynolds number. For all of the cases, Pr is fixed at 0.025. Table 3.4 gives the results of the comparison.

Ek	Ra/Ra_c	$\overline{Nu}_{AA}$	$\overline{Nu}_{MC}$	$\overline{Re}_{c(AA)}$	$\overline{Re}_{c(MC)}$	$\overline{Re}_{z(AA)}$	$\overline{Re}_{z(MC)}$
10^{-5}	2	1.04	1.04	252	253	187	183
10^{-5}	4	1.93	1.96	2140	2200	2850	2900
10^{-5}	8	2.10	2.20	2600	2710	2715	2710
10^{-6}	2	1.09	1.09	709	722	622	635

Table 3.4: Results from the QG spherical shell thermal convection model used in this study (AA), and those from M. Calkins (MC) (Calkins et al., 2012b), where we give Ekman number (Ek), the Rayleigh number relative to the critical Rayleigh number (Ra/Ra_c), the time-averaged Nusselt number ($\overline{Nu}$), time-averaged convective Reynolds number ($\overline{Re_c}$), and time-averaged zonal Reynolds number ($\overline{Re_z}$). The maximum percent error for any given parameter was $\approx 3\%$.

3.4.5.2 Paraboloidal Modifications

Here we give the essential modifications required to modify the QG spherical shell system to that of a QG paraboloid. This system has yet to be benchmarked, has not yet been peer-reviewed, and only serves as a theoretical guide for future studies.

In the QG system, u_s and u_ϕ are independent of z, implying that u_z is linear in z. We can integrate u_z with respect to z, leading to

$$\frac{\partial u_z}{\partial z} = \frac{u_{z,T} - u_{z,B}}{h}. \tag{3.114}$$

The flat, solid bottom boundary has a no-slip condition, requiring that $u_{z,b} = 0$. It remains to find $u_{z,T}$. The first contribution to this velocity is from the non-penetration boundary condition at the top curved outer boundary, quantified by the topographic-β effect (Schaeffer and Cardin, 2005). The second contribution comes from 'Ekman pumping,' which is a secondary circulation owing to viscous coupling between the fluid and rotating solid bottom boundary. A geometry-independent, asymptotic expression in the limit of $Ek \to 0$ exists for Ekman pumping (Greenspan, 1968). Thus, a general form of the stretching of axial vorticity becomes, (Schaeffer and Cardin, 2005).

$$\frac{\partial u_z}{\partial z} = Ek^{1/2} P(u_s, u_\phi, r) + \beta u_s, \tag{3.115}$$

where $P(u_s, u_\phi, r)$ comes from Ekman pumping, and the second term on the right hand side is a result of the no-penetration condition. We start by deriving β for the paraboloid. The free-surface height of the fluid layer in dimensional form is given by

$$h(s) = h_0 + \frac{\Omega^2 s^2}{2g}. \tag{3.116}$$

We nondimensionalize Eq. 3.118 by radial gap width $R = R_o - R_i$

$$\frac{h(s)}{(R_o - R_i)} = \frac{h_0}{(R_o - R_i)} + \frac{\Omega^2 s^2}{2g(R_o - R_i)}. \tag{3.117}$$

Noting that $s = (R_o - R_i)s^*$ and substituting, we have

$$\frac{h(s)}{(R_o - R_i)} = \frac{h_0}{(R_o - R_i)} + \frac{\Omega^2 s^{*2} (R_o - R_i)^2}{2g(R_o - R_i)}, \tag{3.118}$$

yielding the nondimensional form

$$h^*(s) = h_0^* + \frac{\Omega^2 s^{*2} (R_o - R_i)}{2g}, \tag{3.119}$$

where $h_0^* = h_0/(R_o - R_i)$ is the nondimensional height of the fluid at $s = 0$ and is controlled by the volume of fluid in a given tank. Recalling the Froude number,

$$Fr = \frac{\Omega^2(R_o - R_i)}{g}, \tag{3.120}$$

we can rewrite Eq. 3.119 as

$$h^*(s) = h_0^* + \frac{Fr\ s^{*2}}{2}. \tag{3.121}$$

Thus the nondimensional topographic-β effect becomes

$$\frac{dh^*}{ds^*} = s^*(Fr). \tag{3.122}$$

Thus, the stretching of vorticity term can be written as

$$\frac{\partial u_z}{\partial z} = Ek^{1/2}P(u_s, u_\phi, r) + \left(\frac{Fr}{h_0^* + \frac{(Fr)s^{*2}}{2}}\right)s^* u_s. \tag{3.123}$$

Next, we find the Ekman pumping term for our geometry, which is simpler than the spherical shell. This is because the top boundary, a free-surface, will not contribute to the Ekman pumping. However, the flat solid bottom boundary will, and the stretching of vorticity is then described by (dropping the asteriks that denote nondimensional quantities) (Greenspan, 1968; Schaeffer and Cardin, 2005):

$$\frac{\partial u_z}{\partial z} = -\frac{E^{1/2}}{2h}(\omega) + \left(\frac{Fr}{h_0 + \frac{(Fr)s^2}{2}}\right)s\ u_s. \tag{3.124}$$

Eq. 3.113 includes an additional contribution: the azimuthally averaged radial velocity, a consequence of topographic curvature and circulation in the Ekman layer (Calkins et al., 2012b). This term, proportional to $\langle u_s \rangle$ is geometry-dependent and we can derive it by invoking azimuthally averaged mass conservation

$$\frac{1}{s}\Big(\frac{\partial\langle su_s\rangle}{\partial s}\Big) = -\Big(\frac{\partial\langle u_z\rangle}{\partial z}\Big), \tag{3.125}$$

We can calculate the right hand side of Eq. 3.125 by azimuthally averaging Eq. 3.124 (dropping the asterisks (*) that denote nondimensional numbers)

$$\frac{1}{s}\Big(\frac{\partial\langle su_s\rangle}{\partial s}\Big) = -s(Fr)\left(\frac{1}{h(s)}\right)\langle u_s\rangle + \frac{E^{1/2}}{2h(s)}(\langle\omega\rangle). \tag{3.126}$$

Noting that

$$\langle \omega \rangle = \frac{1}{s}\frac{\partial}{\partial s}\Big(s\langle u_\phi \rangle\Big), \tag{3.127}$$

we can rewrite Eq. 3.126 as

$$\frac{1}{s}\Big(\frac{\partial \langle s u_s \rangle}{\partial s}\Big) = -s(Fr)\left(\frac{1}{h(s)}\right)\langle u_s \rangle + \frac{E^{1/2}}{2h(s)}\Big(\frac{1}{s}\frac{\partial}{\partial s}(s\langle u_\phi \rangle)\Big). \tag{3.128}$$

Applying the product rule to expand the only term on the left hand side the and the second term on the right hand side of Eq. 3.128 gives

$$\frac{\partial \langle u_s \rangle}{\partial s} + \frac{\langle u_s \rangle}{s} = -s(Fr)\left(\frac{1}{h(s)}\right)\langle u_s \rangle + \frac{E^{1/2}}{2h(s)}\Big(\Big(\frac{\partial \langle u_\phi \rangle}{\partial s}\Big) + \frac{\langle u_\phi \rangle}{s}\Big). \tag{3.129}$$

Grouping terms together,

$$\frac{\partial \langle u_s \rangle}{\partial s} = \Big(\frac{-s(Fr)}{h(s)} - \frac{1}{s}\Big)\langle u_s \rangle + \frac{E^{1/2}}{2h(s)}\Big(\Big(\frac{\partial \langle u_\phi \rangle}{\partial s}\Big) + \frac{\langle u_\phi \rangle}{s}\Big), \tag{3.130}$$

where the first term on the right hand side represents the radial velocity induced by the topographic-β effect, and the remainder constitute those effects from the Ekman layer at the bottom boundary. Eq. 3.124 and Eq. 3.130 summarize the modifications made to simulate convection in a QG paraboloidal free-surface with a flat bottom boundary, rather than spherical shell.

Possibilities for future work include benchmarking the steps laid out here by comparing to linear theory, and using the QG paraboloid in conjunction with the Coreaboloid to learn more about low latitude core dynamics.

3.5 Discussion

Earth's magnetic field is generated and sustained by fluid motions in the liquid iron outer core, in a process known as dynamo action. Modeling the fluid motions underlying the geodynamo is challenging both computationally and experimentally owing to the separation of scales required to resolve core-style convective turbulence. To this end, we have developed a novel laboratory device with a curved paraboloidal free surface and laterally driven convection to understand the hydrodynamic base flow responsible for the geodynamo. The laboratory device, which we call "the Coreaboloid" (Core + Paraboloid) uses rotation and a radial temperature gradient induced by a cold source at the inner boundary to drive centrifugal buoyancy and baroclinic instability, which could both be drivers of turbulence. We collect UDV velocity profiles, novel surface thermography, and basal thermometry for diagnostics.

A particularly important feature of this device is the curved paraboloidal free surface, quantified by the topographic β-effect. We show that the topographic β-effect from our paraboloidal geometry is a useful proxy to model the curved boundary of a spherical shell. In addition, we demonstrate that the heat flux decay through the paraboloidal system is also similar to that of a spherical shell. These two comparisons allow us to extrapolate our paraboloidal findings to understand core flow at first order.

We use our novel Coreaboloid device with a curved paraboloidal free surface and laterally driven convection and baroclinic instability to obtain several interesting flow features by running three cases at 35, 50, and 60 RPM. First, an analysis of thermal anomalies in azimuth over time for the 50 and 60 RPM cases yields a phase speed similar to the theoretical Rossby wave propagation speed, demonstrating that Rossby waves from the β-effect are generated in this system. This analysis also shows that the novel thermal imaging system used in this study can be used to describe the flow field.

Second, in all cases we find a series of alternating prograde-retrograde jets after averaging the UDV azimuthal velocity over ten minutes of data. The width of the jets closely follows the Rhines scaling prediction. This shows that we likely have an inverse cascade of energy halted by the β-effect. Moreover, in the 60 RPM case, we find a migration of the jets that can be predicted by a theoretical migration speed. The theoretical migration speed is parameterized based on the results of (Cope, 2021) using the Ekman drag timescale and the Rhines scale jet width. This leads to a differential equation that can be integrated for the radial position of a jet core as a function of radius and time. We numerically integrate this function, and show that the jet core trajectory closely matches the migration of jet cores in the 60 RPM case. Jet migration has been shown to result from nonlinear eddy interactions (Cope, 2021), which likely contributes to the phenomena observed here.

Furthermore, we carry out a broader analysis of the azimuthal length scales measured in each case by comparing these values to various, theoretical predicted scales such as the Rossby deformation radius. Though we do not find good agreement between the scales measured here and those predicted by theory, this remains an open question for future studies. We do however find that anomalies in the measured jet profiles near the outer boundary occur at a radial location that matches a theoretical boundary layer thickness known as the Stewartson layer.

Finally, we are currently edited a model of QG thermal convection in a spherical shell to include a paraboloidal free-surface geometry. First results indicate convective structures that are sheared in the retrograde direction, and a zonal flow profile that is qualitatively similar to previous spherical shell results. However, more work must be done to benchmark the QG paraboloid before comparisons to the Coreaboloid are made, though the derivations made here lay the theoretical groundwork for future QG paraboloid models. This device is unique in its ability to generate a large β-effect and in its use of lateral convection to drive turbulence. Given the dependence of the topographic β-effect on rotation rate, the system is also flexible, capable of testing wide ranges of β without modifications. Additionally, the use of an infrared thermographic camera to map temperature fields to flow fields has not been done previously, to our knowledge.

The device could be further improved by introducing active heating and cooling elements at the inner and outer boundaries, allowing for steadier forcing and longer experiment times. Additionally, introducing a transparent lid above the paraboloidal surface would reduce the impacts of air drag and outside temperature variations. Finally, developing a computational system that can map the thermal field quantitatively to a velocity field would allow us to study the dynamics of the system through an analysis of the surface temperature field.

Appendix C

Fitting Jet Migration Data

As discussed in Section 3.4.3, the jets in the 60 RPM case meander in Γ, also known as jet migration. Though we are able to closely model the jet migration speed V_{mig} using the theoretical relationship derived from (Cope, 2021), we carry out additional methods to analyze this behavior. One such method involves carrying out a linear fit to the azimuthal Doppler velocity data in time. To do this, first isolate the azimuthal velocity data of a particular jet by masking out data not within that jet. The analysis here is for jet three in the 60 RPM case (see Fig. 3.18(c)). We also neglect data where $t < 1900$s, as the jet signature is anomalous before this range. Then, we track the location of the "jet core" in time and radius. We define the location of the jet core as the location of the maximum azimuthal velocity where

$$s_{core} = s|_{u_\phi = max(u_\phi)}. \tag{C.1}$$

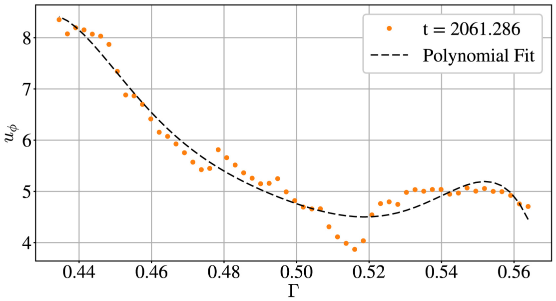

Figure C.1: A sixth order polynomial fit to the azimuthal Doppler velocity data at $t = 2061.286$s used to track the radial location of the jet core in time.

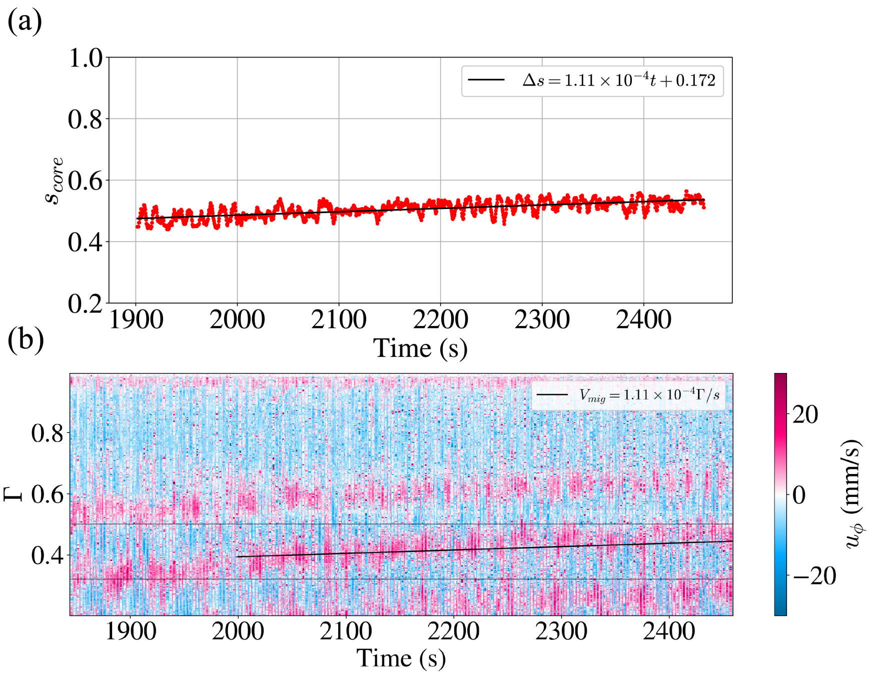

Figure C.2: (a) Location of s_{core} versus time, calculated by finding the location of maximum of the sixth-order polynomial fit using u_ϕ. We use a linear fit on $s_{core}(t)$, and the slope is V_{mig}. (b) V_{mig} overlaid on the Hovmöller for the 60 RPM case.

Due to noise in the Doppler data, we find that tracking $max(u_\phi)$ yield anomalies in the location of the jet core. To mitigate this, we carry out a sixth-order polynomial fit of u_ϕ versus Γ at each point in time. Fig. C.1 shows an example of this polynomial fit at $t = 2061.286$s. We take the maximum of the best fit to this function, which minimizes the risk of using noise in the data as the maximum of the velocity signal, and thus the location of the jet core. Fig. C.2(a) shows s_{core} as a result of this method versus time. We carry out a linear fit of $s_{core}(t)$, and obtain a jet migration speed V_{mig}.

Fig. C.2(b) shows $V_{mig} = 1.11 \times 10^{-4}\Gamma/\text{s}$ overlaid on the Hovmöller for the 60 RPM case. The value calculated from this process slightly underestimates that jet migration speed, and could be improved by refining the methods used to remove noise in the data.

CHAPTER 4

Conclusion

Zonal flows or “jets” are important features found in an array of geophysical and astrophysical fluid layers. They are the most visually dominant structures observed at the surfaces of the Gas Giant planets, Jupiter and Saturn. They are also responsible for mechanisms such as the transportation of warm and cool air in atmospheres, which can drive complex weather patterns. In addition, they could play an important role in the generation of Earth’s magnetic field through the Ω-effect, in which zonal flows provide large-scale shears to convert components of poloidal fields into toroidal fields. I have carried out a series of numerical simulations and theoretical analyses to contribute to our understanding of zonal flows in these systems. Broadly, my results give important insight into the damping and formation of jets. First, we find that the inertia of the jets dictates the strength of an external magnetic field required to damp them. In addition, nonlinear interactions through the inertial term can result in an inverse transfer of energy upscale and manifest as a series of alternating prograde-retrograde jets, some of which migrate laterally. Furthermore, a change in axial fluid layer height with depth can generate Rossby waves and set the observed length scale of these jets.

Specifically, in Chapter 2 we investigate the fundamental process of magnetic damping on convectively driven large-scale jets using a reduced, quasi two dimensional numerical model with an imposed vertical magnetic field. We use this reduced model as a proxy to gain insight into how the jets observed at the surface of Jupiter and Saturn may be slowed with electromagnetic braking as their electrical conductivity increases radially with depth. Thus, we explore how the increasing importance of magnetohydrodynamic processes with depth may damp the hydrodynamic zonal winds observed at the surface. We begin by demonstrating how strong planetary rotation relative to other forces suggests that the flow may be approximately invariant along the axis of rotation. This allows us to use a massively simplified quasi two-dimensional Cartesian box to model a slice of the Jovian atmosphere parallel to the equatorial plane. We then present the general framework for understanding MHD flows under the presence of a strong, uniform magnetic field, which includes a demonstration of the equivalence of the potential and induction formulations to simplify the Lorentz force.

After introducing the governing equations and numerical method for our quasi two dimensional magnetoconvection system, we briefly discuss marginal stability analysis and its implications for the critical Rayleigh number Ra_c and the critical length scale l_c. We use this system to carry out a suite of about 60 numerical simulations in a parameter space where Ra and Ch are both varied by several orders of magnitude. In this parameter space, we quantitively define five different regimes that are similar to those found in various studies of magnetoconvection (Yan et al., 2019; Zürner, 2020) and rotating convection (Nieves et al., 2014; Stellmach et al., 2014; Horn and Aurnou, 2018; Kunnen, 2021; Madonia et al., 2021). These regimes are (i) steady convection rolls, (ii) steady magneto-columns, (iii) unsteady to turbulent magneto-plumes, (iv) horizontally drifting magneto-plumes, and (v) jets with intermittent turbulent convective bursts. We discuss the momentum and heat transport properties of each regime, before measuring their characteristic length scales and velocity scales. We then use the length and velocity scalings found in each regime to construct three different interaction parameter-based regime transition lines that can be used to distinguish one regime from the next.

It is the transition to the jet dominated regime has the most immediate applications to the magnetic damping of Jovian jet flows. We find that the separation between jets and a magnetically constrained system occurs at a jet-based interaction parameter value

$N_J \approx 1$. To apply our results to a Jovian system, we estimate two different interaction parameters based on the magneto-thermal wind equation, which is simplified by noting that radially increasing electrical conductivity has a leading order impact on the dynamics. One interaction parameter N is given by the ratio of the advection of vorticity term to the Lorentz torque. The next, N_Ω is given by the ratio of the Coriolis term to the Lorentz torque. After calculating N, N_Ω we find that the Lorentz torque can only overcome the inertial terms at a truncation depth of $d_T \approx 6000$ km. This is deeper than recent gravity harmonics data from the Juno mission suggests. Based on our quasi two dimensional results, we conclude that the Lorentz force alone likely cannot brake the jets on Jupiter, and additional mechanisms, such as a stably stratified density layer, are needed to fully truncate them Liu et al. (2008); Heimpel and Aurnou (2012); Cao and Stevenson (2017); Christensen et al. (2020); Gastine and Wicht (2021).

The code used to carry out the project in Chapter 2 was written as a portion of this thesis work primarily following Glatzmaier (2014). In the remaining portion of Chapter 2, I discuss further details of the code including the spatial and temporal discretization schemes. At each step of the development process, the solver was benchmarked to known results including RBC and MC linear theory, and fully nonlinear RBC and MC studies. Finally, Appendix E gives an abbreviated version of the Fortran code in which we present the main time integration loop.

In Chapter 3, we focus on an alternative open question regarding jets in planetary fluid systems: the processes that control their generation and sets their length scale. In particular, we use a novel laboratory-numerical set up that includes both strong buoyancy forces to drive inertial flows, and strong boundary curvature to explore the formation jets flow. Our system is a proxy to understand the process through which Earth's magnetic field is generated through fluid motions in the liquid outer core at low latitudes. Turbulence in the laboratory device is driven through centrifugal buoyancy and baroclinic instability, both of which manifest in structures with different characteristic length scales. Further, the turbulence here is constrained by the device's strong background rotation. Rotationally constrained turbulence has been shown to mimic two-dimensional turbulence. However, deviations from geostrophy occur in nearly all geophysical systems. One such phenomenon that anistropizes the nearly axially invariant flow and thus halts the inverse energy cascade is the topographic-β effect. For a deep spherical shell, such as the outer core, $\beta \rightarrow \infty$ at the equator, and thus likely has leading order effects on the dynamics.

Next, we discuss the experimental set up, which features a paraboloidal free surface and cylindrically radial temperature gradient. The device was built and the cases were run by previous UCLA student Taylor Lonner, without whom this project would not be possible. Diagnostics are collected through UDV velocity profiles, novel surface thermography, and basal thermometry. We demonstrate that this novel paraboloidal set-up approximates the topographic β and heat flux profiles in a sphere, thus provides a meaningful proxy to study low-latitude core convection.

We present three rotating convection cases in the paraboloidal device at 35, 50, and 60 RPM where UDV velocity profiles, surface thermography, and basal thermometry are collected. Given the combination of and a topographic β-effect, we expect to see several jets in the system following the characteristic Rhines scale wavenumber where the inverse cascade of energy is halted through Rossby wave propagation. We find that Rossby waves are excited in our system by analyzing the surface thermal anomaly data in ϕ, t at gap location $\Gamma = 0.5$. The azimuthal wavenumber, k, is first measured by taking an FFT of the thermal anomaly, and used along with $\beta|_{\Gamma=0.5}$ in the dispersion relationship to predict the Rossby wave speed. The Rossby wave speed is compared to the slope of the thermal structures in ϕ, t. We find good agreement between the theoretical speed and those measured in the device.

The Rossby waves excited here likely drive the alternating prograde-retrograde jets observed in each case at 35, 50, and 60 RPM. We analyze the jet width of these structures and compare them to the predicted Rhines scale, which is controlled by the β-effect. The process to measure the width of the jets is as follows: first, the net azimuthal drift is subtracted from the zonal flow profiles. For the 35 RPM case, this amounts to removing the mean drift speed, whereas the 50 RPM and 60 RPM cases require a subtraction of a linear fit of the velocity profile due to asymmetries in the zonal flow behavior with radius. Next, we find the radial locations at which the corrected zonal flow profiles cross zero. The measured jet width is given by the difference in radius of these zero crossings. This jet width is compared to the Rhines scale prediction, and for all cases and radial locations the ratio remains fixed near unity, indicating that the jets observed in our system indeed follow the Rhines scale.

In the 60 RPM case, several of the jets meander in Γ, which is known as jet migration. Jet migration has been found to occur typically in models that included the full nonlinear interactions between small scale eddies. We build upon the work of Cope (2021) who found a theoretical jet migration speed, V_{mig}, that depends on the Rhines scale and a drag timescale. We use this relationship to derive an paraboloidal estimate for V_{mig}, and integrate the resulting equation numerically to find the radial translation of the jet core in time. Overlaying this curve on plots of $u_\phi(\Gamma, t)$ demonstrates good agreement between our relationship for V_{mig} and the observed migration speed. This shows that the jet migration may be driven by nonlinear interactions between small scale eddies, and is controlled by the Rhines scale and the Ekman drag timescale.

Next, we seek to find the mechanism that controls the horizontal (relative to the axial direction) scale of the flow, l_ϕ. We derive several theoretical relationships for this scale based on leading order force balances. We also consider the Rossby deformation scale, which is the size of the structures resulting from baroclinic instability. After comparing these theoretical scales to l_ϕ measured through the FFT of the thermal anomaly data, it is remains unclear which physical mechanism may be setting the length scale of the observed structures. Thus, this is still an open question.

Finally we discuss the numerical portion of this study, in which we modify the quasi geostrophic (QG) spherical shell model developed by Calkins et al. (2012b) to include a paraboloidal geometry. The first step of this process is to re-run the spherical shell model and benchmark the results to previous QG spherical shell studies. After doing this, we present the analytical framework for modifying the Ekman pumping and vortex stretching terms for a paraboloidal system. We carry out a test case of paraboloidal QG code, and find convective structures sheared in the retrograde direction, we is expected for a system in which $dh/ds > 0$. We find one strong prograde jet near the inner boundary, and a weaker jet near the outer boundary. However, further steps to benchmark the paraboloidal QG code to ensure its efficacy were not carried out, and these steps should be taken in the future before additional analysis is done. This part of our study lays the groundwork for future paraboloidal QG models.

The work presented in this thesis advances our understanding of how zonal flows in planetary fluid systems form, evolve, and decay. Future work could include accounting for a spatially varying electrical conductivity and characterizing its impact of the electromagnetic damping discussed in Chapter 2. Or, more complex paraboloidal models could be coupled to the laboratory device discussed in Chapter 3. There are many open questions that remain about planetary scale zonal flows.

Appendix D

Jet Migration Integration Script

This section gives the code used to find the jet migration velocity discussed in Sec. 3.4.3.

```
#!/usr/bin/env python3
# -*- coding: utf-8 -*-
"""
Created on Thu Jan 13 10:46:57 2022
@author: ashnaaggarwal
"""


import matplotlib
import matplotlib.pyplot as plt
import numpy as np
import scipy.integrate as integrate
import scipy.special as special
from scipy.integrate import quad


plt.rcParams.update({'font.size': 30})
cbformat = matplotlib.ticker.ScalarFormatter()   # create the formatter
cbformat.set_powerlimits((-2,2))
plt.rcParams["font.family"] = "Times New Roman"


matplotlib.rcParams['mathtext.fontset'] = 'cm'
matplotlib.rcParams['mathtext.rm'] = 'cm'
```

```
matplotlib.rcParams['mathtext.it'] = 'cm:italic'
matplotlib.rcParams['mathtext.bf'] = 'cm:bold'
plt.rcParams['axes.axisbelow'] = True

#goal is to integrate jet migration function

#defining constants
nu = 1e-2; #cm^2/s
omega = 6.3 #rad/s
h0 = 2.06 #cm
g = 981 #cm/s^2
U = 0.15 #cm/s
DeltaR = (37.25 - 10) #gap width, cm
r0 = 10.16; #cm
s2 = 14.5+r0; #cm
s1 = 8.80+r0; #cm

A = (2*omega**2*h0)/(nu*U*g)
B = (omega**4)/(nu*U*g**2)


def integrand(s, A, B):
    return np.sqrt(A*s + B*s**3)          #the function to integrate
#goal is to start integration at s = s1 (initial point of jet core)
#and integrate equation above to find location at s + \delta s
n = 1000
ds = (s2-s1)/n
s_total = []          #will have each point in s
t_total = []
```

```
s_total.append(s1)
t_total.append(0)

print(ds, 'integration␣step␣in␣cm')

for i in range(1, n):
    I = quad(integrand, s1, s1 + ds, args=(A,B))  #evaluating integral to find dt
    dt = I[0]   #pulling only the value that we need
    ds = np.sqrt((nu*U*g)/
    (2*omega**2*s1*(h0+(omega**2*s1**2)/(2*g))))*dt #ds = vm*dt
    s1 = s1 + ds #advancing s
    s_total.append(s1) #saving s
    t_total.append(t_total[i-1] + dt) #saving t

plt.figure(figsize=(9,7))
plt.grid()
plt.plot(t_total, np.array(s_total)*10, linestyle='solid', color='darkviolet')
plt.xlabel('Time␣(s)')
plt.ylabel('Jet␣position␣(mm)')
plt.tight_layout()
plt.savefig('Vmig_Ujet_60RPMJet3.png', dpi=200)
plt.show()

plt.figure(figsize=(9,7))
plt.grid()
plt.plot(t_total, (np.array(s_total)-r0)/DeltaR,
         linestyle='solid', color='darkblue')
plt.xlabel('Time␣(s)')
plt.ylabel('Jet␣position␣($\Gamma$)')
```

```
plt.tight_layout()
plt.savefig('Vmig_Gamma_Ujet_60RPMJet3.eps')
plt.show()

Gammaloc = (np.array(s_total)-r0)/DeltaR
print(Gammaloc[-1]-Gammaloc[0], 'total␣gamma')
print(t_total[-1]-t_total[0])

t_array = np.array(t_total)
Gamma_array = (np.array(s_total)-r0)/DeltaR
np.savetxt('Gamma_t_60RPMJet3.txt', list(zip(t_array, Gamma_array)),
        header = 't(s)␣␣␣␣␣␣␣␣␣␣␣␣␣␣␣␣␣␣␣␣␣␣Loc␣(\Gamma)')
```

Appendix E

Main Solver of 2D Magnetoconvection Code

Here we give an abbreviated version of the code developed for the thesis work in this Chapter 2. It includes the main routine in which the variables of interest (temperature, vorticity, streamfunction, and velocity) are integrated in time and saved in external files. The code snippet does not include input files, subroutines, or the initialization of variables and arrays.

```

!Start time loop ~~!


call cpu_time(starttime)


do nt=nt_start, nsteps
call communicate(tem,ierr, my_rank, size, kstart, kfinal,nn)
!communicating between ranks before calculation
call communicate(omg,ierr, my_rank, size, kstart, kfinal,nn)
call communicate(psi,ierr, my_rank, size, kstart, kfinal,nn)


!Step 1: calculate dtempdt (derivative of temperature)
!and domgdt (derivative of vorticity) based on linear/nonlinear terms


do kaux =kstart, kfinal
kreal = my_rank*nz_aux + kaux
do n=0,nc
```

```
dtempdt(kaux,n,2) = sqrt(1.d0/(Ra*Pr))*(tem(kaux+1,n) - tem(kaux-1,n))
*oodq2_1(kaux)+
sqrt(1.d0/(Ra*Pr))*((tem(kaux+1,n) - 2.d0*tem(kaux,n) + tem(kaux-1,n))
*oodq2_2(kaux)- &
((real(n,8)*2.d0*pi/a)**2*tem(kaux,n)))
!Finite difference to update derivative of temperature

domgdt(kaux,n,2) = (2.d0*real(n,8)*pi/a)*j*tem(kaux,n) + &
sqrt(Pr/Ra)*((omg(kaux+1,n) - omg(kaux-1,n))*oodq2_1(kaux)+&
(omg(kaux+1,n) - 2.d0*omg(kaux,n) + omg(kaux-1,n))*oodq2_2(kaux)  &
- ((real(n,8)*2.d0*pi/a)**2)*omg(kaux,n))+&
(Ch*sqrt(Pr/Ra))*((psi(kaux+1,n) - psi(kaux-1,n))*oodq2_1(kaux)+&
(psi(kaux+1,n) - 2.d0*psi(kaux,n) + psi(kaux-1,n))*oodq2_2(kaux))
 !finite difference to update derivative of vorticity
end do
end do

do kaux = kstart-1, kfinal+1
!Spectral transform to calculate nonlinear terms
!Deliase higher modes
tem(kaux,nc+1:nn) = 0.d0
omg(kaux,nc+1:nn) = 0.d0
psi(kaux,nc+1:nn) = 0.d0
!End deliase

!Transforming tem, omg, psi @ current step to physical space
input_spec(kaux,:) = tem(kaux,:)
call dfftw_execute_dft_c2r(planb,input_spec(kaux,:),output_phys(kaux,:))
tem_phys_st(kaux,:) = output_phys(kaux,:)
```

```
input_spec(kaux,:) = omg(kaux,:)
call dfftw_execute_dft_c2r(planb,input_spec(kaux,:),output_phys(kaux,:))
omg_phys_st(kaux,:) = output_phys(kaux,:)

input_spec(kaux,:) = psi(kaux,:)
call dfftw_execute_dft_c2r(planb,input_spec(kaux,:),output_phys(kaux,:))
psi_phys_st(kaux,:) = output_phys(kaux,:)

!End transformation to physical space
end do

!Looping over grid points in z
do kaux = kstart, kfinal
domgdt_phys(kaux,0)= ((psi_phys_st(kaux, 1)) - (psi_phys_st(kaux, nx)))&
*dx2 *((omg_phys_st(kaux+1, 0)) - (omg_phys_st(kaux-1,0)))&
*dq2(kaux) - ((psi_phys_st(kaux+1,0)) - (psi_phys_st(kaux-1,0)))&
*dq2(kaux) *((omg_phys_st(kaux, 1)) - (omg_phys_st(kaux, nx)))*dx2

dtempdt_phys(kaux,0)=((psi_phys_st(kaux, 1)) - (psi_phys_st(kaux, nx)))&
*dx2 *((tem_phys_st(kaux+1, 0)) - (tem_phys_st(kaux-1, 0)))*dq2(kaux)&
 - ((psi_phys_st(kaux+1, 0)) - (psi_phys_st(kaux-1, 0)))*dq2(kaux) &
*((tem_phys_st(kaux, 1)) - (tem_phys_st(kaux, nx)))*dx2

do i=1, nx-1
domgdt_phys(kaux,i)=((psi_phys_st(kaux, i+1))-(psi_phys_st(kaux, i-1)))&
*dx2*((omg_phys_st(kaux+1, i)) - (omg_phys_st(kaux-1,i)))*dq2(kaux) &-
((psi_phys_st(kaux+1,i)) - (psi_phys_st(kaux-1,i)))*dq2(kaux) &
*((omg_phys_st(kaux, i+1)) - (omg_phys_st(kaux, i-1)))*dx2
```

```
dtempdt_phys(kaux,i)=((psi_phys_st(kaux, i+1))-(psi_phys_st(kaux, i-1)))&
*dx2*((tem_phys_st(kaux+1, i)) - (tem_phys_st(kaux-1, i)))*dq2(kaux)- &
((psi_phys_st(kaux+1, i)) - (psi_phys_st(kaux-1, i)))*dq2(kaux) &
*((tem_phys_st(kaux, i+1)) - (tem_phys_st(kaux, i-1)))*dx2

end do

domgdt_phys(kaux,nx) = domgdt_phys(kaux,0)
!Periodic BC, values at nx=0 should match endpoint at nx
dtempdt_phys(kaux,nx) = dtempdt_phys(kaux,0)
!Periodic BC, values at nx=0 should match endpoint at nx

input_phys(kaux,:) = dtempdt_phys(kaux,:)
!Transforming nonlinear terms back to spectral space (tem)
call dfftw_execute_dft_r2c(planf,input_phys(kaux,:),output_spec(kaux,:))
tem_nl(kaux,:) = output_spec(kaux,:)

input_phys(kaux,:) = domgdt_phys(kaux,:)
!Transforming nonlinear terms back to spectral space (omg)
call dfftw_execute_dft_r2c(planf,input_phys(kaux,:),output_spec(kaux,:))
omg_nl(kaux,:) = output_spec(kaux,:)
!Dealiasing yet again
tem_nl(kaux,nc+1:nn) = 0.d0
omg_nl(kaux,nc+1:nn) = 0.d0

tem_nl(kaux,:) = (tem_nl(kaux,:))/(nx)
!normalize the FFTW
omg_nl(kaux,:) = (omg_nl(kaux,:))/(nx)
```

```
!normalize the FFTW

do n=0,nc
dtempdt(kaux,n,2) = dtempdt(kaux,n,2) + tem_nl(kaux,n)
!adding nonlinear tem modes to derivative
domgdt(kaux,n,2) = domgdt(kaux,n,2) + omg_nl(kaux,n)
!adding nonlinear omg modes to derivative
end do
end do

!Step 2: Use dtempdt and domgdt to update tem and omg

do kaux = kstart, kfinal
do n =0, nc
tem(kaux,n) = tem(kaux,n) + (dt/2.d0)*(3.d0*dtempdt(kaux,n,2)&
- dtempdt(kaux,n,1))
!AB2 time integration scheme to update temperature based on derivatives
omg(kaux,n) = omg(kaux,n) + (dt/2.d0)*(3.d0*domgdt(kaux,n,2) &
- domgdt(kaux,n,1))
!AB2 time integration scheme to update vorticity based on derivatives
end do
end do

call communicate(tem,ierr, my_rank, size, kstart, kfinal,nn)
!communicating updated values of tem with other ranks
call communicate(omg,ierr, my_rank, size, kstart, kfinal,nn)
!communicating updated values of omg with other ranks

!Step 3: Solve poisson equation for streamfunction
```

```
!Grid cannot be parallel in z, swap direction to x using MPI_ALLTOALL

call MPI_ALLTOALL(omg(1:nz_aux,:), nz_aux*nn_aux, &
MPI_DOUBLE_COMPLEX, omg_flat(:), nz_aux*nn_aux, &
MPI_DOUBLE_COMPLEX, MPI_COMM_WORLD, status, ierr)
!First step is to switch direction of vorticity parallelizaiton
!all to all by default flattens array to 1D
do rankloop=0, size-1
!Loop to organize flattened omg array to 2D array
!with dimensions (nz, nn_aux)
do kaux=1,nz_aux
do n_aux=0,nn_aux-1
omg_trans(kaux+rankloop*nz_aux, n_aux) = &
omg_flat(rankloop*nz_aux*nn_aux + kaux + nz_aux*n_aux)
end do
end do
end do

omg_trans(1,:) = 0.d0
!Enforcing BC on vorticity for all modes at nz=1

do n_aux=0,nn_aux-1
!Each processors loops over nn/nproc number of modes
nreal = my_rank*nn_aux + n_aux
!Keeping track of the (nonparallel) mode number
do k=2,nz-1
!Looping over grid points in z
dia_full(k) = (2.d0*real(nreal,8)*pi/a)**2 + 2.d0*oodq2_2_full(k)
!Diagonal values of array based on location in z and mode
```

```
end do
dia_full(1) = 1.d0
!Boundary condition of diagonal
dia_full(nz) = 1.d0
!Boundary condition of diagonal
call tridi(nz, omg_trans(:,n_aux), &
psi_trans(:,n_aux), sub_full(:), dia_full(:),&
sup_full(:), wk1_full(:), wk2_full(:))
!calling tridiagonal solver to update streamfunction
end do

psi_trans2(0:nn_aux-1,1:nz) = &
TRANSPOSE(psi_trans(1:nz, 0:nn_aux-1))
!must transpose psi output of tridiag solver

call MPI_ALLTOALL(psi_trans2(0:nn_aux-1,:), &
nz_aux*nn_aux, MPI_DOUBLE_COMPLEX, &
psi_flat(:), nz_aux*nn_aux, MPI_DOUBLE_COMPLEX, &
MPI_COMM_WORLD, ierr)
!all to all by default flattens array to 1D

do rankloop=0, size-1
!Loop to organize flattened psi_trans array to 2D array
do n_aux=0,nn_aux-1
!Loop to organize flattened psi_trans array to 2D array
do kaux=1,nz_aux
psi(kaux, n_aux+rankloop*nn_aux) = &
psi_flat((rankloop*nn_aux*nz_aux + n_aux + nn_aux*(kaux-1))+1)
end do
```

```
end do
end do

if (my_rank .eq. 0) then
psi(kstart -1,:) = 0.d0
!Enforcing BC for the streamfunciton
end if
call communicate(psi, ierr, my_rank, size, kstart, kfinal,nn)

!Step 4: Use updated streamfunction, vorticity, and temperature
!to calculate output quantities including velocities and heat transfer

!Transform temperature, streamfunction
!and vorticity from Fourier to physical space
do kaux=kstart -1, kfinal+1
input_spec(kaux,:) = tem(kaux,:)
call dfftw_execute_dft_c2r(planb,input_spec(kaux,:),output_phys(kaux,:))
tem_phys(kaux,:) = output_phys(kaux,:)

input_spec(kaux,:) = omg(kaux,:)
call dfftw_execute_dft_c2r(planb,input_spec(kaux,:),output_phys(kaux,:))
omg_phys(kaux,:) = output_phys(kaux,:)

input_spec(kaux,:) = psi(kaux,:)
call dfftw_execute_dft_c2r(planb,input_spec(kaux,:),output_phys(kaux,:))
psi_phys(kaux,:) = output_phys(kaux,:)
end do

!Calculate output parameters. Not needed every time step
```

```
do i=0, nx
do kaux=kstart,kfinal
vx_phys(kaux,i) = (psi_phys(kaux+1,i) - psi_phys(kaux-1,i))*dq2(kaux)
!velocity in x-direction based on der. of streamfunciton in z
end do
if (my_rank .eq. size-1) then
vx_phys(kfinal+1, i) = vx_phys(kfinal,i)
end if
if (my_rank .eq. 0) then
vx_phys(kstart-1, i) = vx_phys(kstart, i)
end if
end do
do kaux=kstart-1, kfinal+1
do i =1, nx-1
vz_phys(kaux,i) = -(psi_phys(kaux,i+1) - psi_phys(kaux,i-1))*dx2
end do
vz_phys(kaux,0) = -(psi_phys(kaux, 1) - psi_phys(kaux, nx))*dx2
vz_phys(kaux,nx) = -(psi_phys(kaux, 0) - psi_phys(kaux, nx-1))*dx2
end do

call communicate_r(vx_phys,ierr, my_rank, size, kstart, kfinal,nx)
!communicatng real data between ranks
call communicate_r(vz_phys,ierr, my_rank, size, kstart, kfinal,nx)
call communicate_r(tem_phys,ierr, my_rank, size, kstart, kfinal,nx)

!Nusselt top and bottom (or through any surface)
do kaux=kstart,kfinal
do i=0,nx
dtempdz_phys(kaux,i) = &
```

```
1.d0*(tem_phys(kaux-1,i)- tem_phys(kaux+1,i))*dq2(kaux) +&
vz_phys(kaux,i)*tem_phys(kaux,i)
end do
end do
do kaux=kstart,kfinal
dtempdz_zonal(kaux) = SUM(dtempdz_phys(kaux,:))*dx/(a)
end do

if (my_rank .eq. 0) then
Nu_bot =  dtempdz_zonal(kstart+1)
end if

if (my_rank .eq. size-1) then
Nu_top =  dtempdz_zonal(kfinal-1)
call mpi_ssend(Nu_top, 1, &
MPI_DOUBLE, 0, 1, MPI_COMM_WORLD, ierr)
end if

if (my_rank .eq. 0) then
call mpi_recv(Nu_top, 1, &
MPI_DOUBLE, (size-1), 1, MPI_COMM_WORLD, status, ierr)
end if

!Nusselt (volume averaged)
do i=0, nx
do kaux=kstart, kfinal
vT_phys(kaux,i) = vz_phys(kaux,i)*tem_phys(kaux,i)
end do
end do
```

```
if (my_rank .eq. 0) then
do i=0, nx
vT_phys_full(1:nz_aux,i) = vT_phys(kstart-1:kfinal,i)
end do
end if
do i=0, nx
if (my_rank > 0) then
call mpi_ssend(vT_phys(kstart:kfinal,i), nz_aux+1, &
MPI_DOUBLE, 0, 1, MPI_COMM_WORLD, ierr)
!Other processors will send convective flux data to Rank 0
else if (my_rank .eq. 0) then
do rankloop=1,size-1
call mpi_recv(vT_phys_full(rankloop*nz_aux + 1 : &
(rankloop+1)*nz_aux,i),nz_aux+1, MPI_DOUBLE,&
rankloop, 1, MPI_COMM_WORLD, status, ierr)
end do
end if
end do

if (my_rank .eq. 0) then
vT_total = 0.d0
do i=0, nx
do k=2, nz-1
vT_total = vT_total + (vT_phys_full(k,i))*dz_full(k)*dx
end do
end do

vT_total = vT_total/(a) !volume averaged
```

```
Nu_vol = 1.d0 + vT_total*(sqrt(Ra*Pr))
end if


call MPI_Bcast(Nu_vol, 1, MPI_DOUBLE, 0, &
MPI_COMM_WORLD, status, ierr)


!Nu visc. diss.
ev_total = 0.d0
Nu_visc = 0.d0
do kaux=kstart, kfinal
kreal = my_rank*nz_aux + kaux
do i=1, nx-1
ev_phys(kaux,i) = ((vx_phys(kaux,i+1)- &
vx_phys(kaux,i-1))*dx2)**2.d0 + &
((vz_phys(kaux+1,i)-vz_phys(kaux-1,i))*dq2(kaux))**2.d0 + &
((vx_phys(kaux+1,i)-vx_phys(kaux-1,i))*dq2(kaux))**2.d0 + &
((vz_phys(kaux,i+1)-vz_phys(kaux,i-1))*dx2)**2.d0
end do


ev_phys(kaux,0) = ((vx_phys(kaux,1)-&
vx_phys(kaux,nx))*dx2)**2.d0 + &
((vz_phys(kaux+1,0)-vz_phys(kaux-1,0))*dq2(kaux))**2.d0 + &
!periodic boundary conditions (wrapping the derivative around for i=0)
((vx_phys(kaux+1,0)-vx_phys(kaux-1,0))*dq2(kaux))**2.d0 + &
((vz_phys(kaux,1)-vz_phys(kaux,nx))*dx2)**2.d0


ev_phys(kaux,nx) = ((vx_phys(kaux,0)-&
vx_phys(kaux,nx-1))*dx2)**2.d0 + &
((vz_phys(kaux+1,nx)-vz_phys(kaux-1,nx))*dq2(kaux))**2.d0 + &
```

```
!periodic boundary conditions (wrapping the derivative around for i=nx)
((vx_phys(kaux+1,nx)-vx_phys(kaux-1,nx))*dq2(kaux))**2.d0 + &
((vz_phys(kaux,0)-vz_phys(kaux,nx-1))*dx2)**2.d0
end do
do i=1,nx-1
ev_phys(kstart-1,i) = ((vx_phys(kstart-1,i+1)-&
vx_phys(kstart-1,i-1))*dx2)**2.d0 + &
((vz_phys(kstart+1,i)-vz_phys(kstart-1,i))*dq2(kstart))**2.d0 + &
((vz_phys(kstart-1,i+1)-vz_phys(kstart-1,i-1))*dx2)**2.d0 + &
((vx_phys(kstart+1,i)-vx_phys(kstart-1,i))*dq2(kstart))**2.d0

ev_phys(kfinal+1,i) = ((vx_phys(kfinal+1,i+1)-&
vx_phys(kfinal+1,i-1))*dx2)**2.d0 + &
((vz_phys(kfinal+1,i)-vz_phys(kfinal-1,i))*dq2(kfinal))**2.d0 + &
((vz_phys(kfinal+1,i+1)-vz_phys(kfinal+1,i-1))*dx2)**2.d0 + &
((vx_phys(kfinal+1,i)-vx_phys(kfinal-1,i))*dq2(kfinal))**2.d0
end do

!Communicatng real data between ranks
call communicate_r(ev_phys,ierr, my_rank, size, kstart, kfinal,nx)

do i=0, nx
do kaux=kstart,kfinal
ev_total = ev_total + ev_phys(kaux,i)*dx*dz(kaux)
end do
end do

do i=1,nx-1
if (my_rank .eq. 0) then
```

```
ev_total = ev_total + ev_phys(kstart -1,i)*dx*dz(kstart)
elseif (my_rank .eq. size -1) then
ev_total = ev_total + ev_phys(kfinal+1,i)*dx*dz(kfinal)
end if
end do
ev_total = (ev_total)/a

call MPI_REDUCE(ev_total, Nu_visc, 1, &
MPI_DOUBLE, MPI_SUM, 0, MPI_COMM_WORLD, ierr)
!sum of individual Nu_visc for total
Nu_viscsum = 1.d0 +  (Nu_visc) !*(sqrt(Ra/Pr)) !
final step, see Goluskin et al. 2014 page 380 for def.
!End Nusselt viscous diss.

!volume averaged zonal flow
vx_total = 0.d0
do i=0, nx
do kaux=kstart,kfinal
vx_total = vx_total + vx_phys(kaux,i)*&
vx_phys(kaux,i)*dx*dz(kaux) !integrating
end do
end do

do i=1,nx-1
if (my_rank .eq. 0) then
vx_total = vx_total + vx_phys(kstart -1,i)*&
vx_phys(kstart -1,i)*dx*dz(kstart)
elseif (my_rank .eq. size -1) then
vx_total = vx_total + vx_phys(kfinal+1,i)*&
```

```
vx_phys(kfinal+1,i)*dx*dz(kfinal)
end if
end do
vx_total = (vx_total)/a

call MPI_REDUCE(vx_total, vx_total_sum, 1, &
MPI_DOUBLE, MPI_SUM, 0, MPI_COMM_WORLD, ierr)

!volume averaged convective flow
vz_total = 0.d0
do i=0, nx
do kaux=kstart,kfinal
vz_total = vz_total + vz_phys(kaux,i)*vz_phys(kaux,i)*dx*dz(kaux)
end do
end do

do i=1,nx-1
if (my_rank .eq. 0) then
vz_total= vz_total+vz_phys(kstart-1,i)*vz_phys(kstart-1,i)*dx*dz(kstart)
elseif (my_rank .eq. size-1) then
vz_total= vz_total+vz_phys(kfinal+1,i)*vz_phys(kstart-1,i)*dx*dz(kfinal)
end if
end do
vz_total = (vz_total)/a

call MPI_REDUCE(vz_total, vz_total_sum, 1, &
MPI_DOUBLE, MPI_SUM, 0, MPI_COMM_WORLD, ierr)
```

```
!Calculating the CFL constraint based on max velocities
call MPI_REDUCE(vx_phys, maxvx, 1, MPI_DOUBLE, &
MPI_MAX, 0, MPI_COMM_WORLD, ierr) !max vx
call MPI_REDUCE(vz_phys, maxvz, 1, MPI_DOUBLE, &
MPI_MAX, 0, MPI_COMM_WORLD, ierr)
cfl_dt = dx/(abs(maxvx))
!End calculating the CFL constraint based on max velocities



!Running time average for several output quantities
!(vx, vz, vx*vz, T, ev, ek, omg, vzT, vxT, vx*vx,
!vx**3, vx**4, vz*vz, vz**3, vz**4, T*T, T**3, T**4

vx_tavg(:, :) = (vx_tavg(:,:)*(iter-1) + vx_phys(:,:))/(iter)
vz_tavg(:, :) = (vz_tavg(:,:)*(iter-1) + vz_phys(:,:))/(iter)
vxz_tavg(:, :)=(vxz_tavg(:,:)*(iter-1)&
+vx_phys(:,:)*vz_phys(:,:))/(iter)
T_tavg(:,:) = (T_tavg(:,:)*(iter-1) + tem_phys(:,:))/(iter)
ev_tavg(:,:) = (ev_tavg(:,:)*(iter-1) + ev_phys(:,:))/(iter)
ek_tavg(:,:) = (ek_tavg(:,:)*(iter-1) + ek_phys(:,:))/(iter)
omg_tavg(:,:) = (omg_tavg(:,:)*(iter-1) &
+ omg_phys(:,:))/(iter)
vzT_tavg(:,:)=(vzT_tavg(:,:)*(iter-1) $
+ tem_phys(:,:)*vz_phys(:,:))/(iter)
vxT_tavg(:,:)=(vxT_tavg(:,:)*(iter-1) &
+ tem_phys(:,:)*vx_phys(:,:))/(iter)
vxsq_tavg(:, :) = (vxsq_tavg(:, :)*(iter-1) + vx_phys(:,:)**2.d0)/(iter)
vxcb_tavg(:, :) = (vxcb_tavg(:, :)*(iter-1) + vx_phys(:,:)**3.d0)/(iter)
vxqr_tavg(:, :) = (vxqr_tavg(:, :)*(iter-1) + vx_phys(:,:)**4.d0)/(iter)
```

```
vzsq_tavg(:, :) = (vzsq_tavg(:, :)*(iter-1) + vz_phys(:,:)**2.d0)/(iter)
vzcb_tavg(:, :) = (vzcb_tavg(:, :)*(iter-1) + vz_phys(:,:)**3.d0)/(iter)
vzqr_tavg(:, :) = (vzqr_tavg(:, :)*(iter-1) + vz_phys(:,:)**4.d0)/(iter)
Tsq_tavg(:,:) = (Tsq_tavg(:, :)*(iter-1) + tem_phys(:,:)**2.d0)/(iter)
Tcb_tavg(:,:) = (Tcb_tavg(:, :)*(iter-1) + tem_phys(:,:)**3.d0)/(iter)
Tqr_tavg(:,:) = (Tqr_tavg(:, :)*(iter-1) + tem_phys(:,:)**4.d0)/(iter)

!Running time average of Nusselt (volume averaged)
if (my_rank .eq. 0) then
Nuvol_tavg = (Nuvol_tavg*(iter-1) + Nu_vol)/(iter)
Nuvol_tavgsave = Nuvol_tavg
end if

avg_freq_sum = avg_freq_sum + avg_freq

!Step 5: Data I/O
!Writing out the running time average of data into netcdf file
call MPI_Bcast(Nuvol_tavgsave, 1, &
MPI_DOUBLE, 0, MPI_COMM_WORLD, status, ierr)
!Only write out the data every outputfreq steps
IF ( (outputfreq /= 0) .AND. (MOD(iter,outputfreq) == 0) ) THEN
call output_2D_hdf5_stat("STAT" // FILE_STRING,kstart-1,kfinal+1,&
transpose(vx_tavg(:,:)), transpose(vz_tavg(:,:)),&
 transpose(vxz_tavg(:,:)),&
transpose(T_tavg(:,:)), transpose(ev_tavg(:,:)), &
transpose(ek_tavg(:,:)),  &
transpose(omg_tavg(:,:)), transpose(vxT_tavg(:,:)), &
transpose(vzT_tavg(:,:)),&
transpose(vxsq_tavg(:,:)), transpose(vzsq_tavg(:,:)), &
```

```
transpose(vxcb_tavg(:,:)), &
transpose(vzcb_tavg(:,:)), transpose(vxqr_tavg(:,:)),&
 transpose(vzqr_tavg(:,:)), &
transpose(Tsq_tavg(:,:)), transpose(Tcb_tavg(:,:)), &
transpose(Tqr_tavg(:,:)),&
my_rank, nz, nz_aux, nx)
!End writing out running time average into netcdf file



!Writing out time series data (Nusselt, vx, vz, probes)
!Only write out times series data every avg_freq steps
IF ( (avg_freq /= 0) .AND. (MOD(iter,avg_freq) == 0) ) THEN
if (my_rank.eq.0) then
write(100,FMT= '(6((10000es16.9),␣2x))') time, abs(Nu_bot), &
abs(Nu_top), abs(Nu_vol), abs(Nu_thermsum), abs(Nu_viscsum)
write(200,FMT= '(6((10000es16.9),␣2x))') time, abs(vx_total_sum), &
abs(vz_total_sum), abs(maxvx), abs(maxvz), cfl_dt
call flush()
end if
!point probes, will be in an if statement
if (point_probe .eqv. .true.) then
if (my_rank .eq. rankprobe1) then
write(400,FMT= '(13((10000es17.9),␣2x))') &
time, tem_phys(kauxprobe1, iprobe1),&
tem_phys(kauxprobe1, iprobe2), tem_phys(kauxprobe1, iprobe3),&
vx_phys(kauxprobe1, iprobe1), vx_phys(kauxprobe1, iprobe2), &
vx_phys(kauxprobe1, iprobe3),&
vz_phys(kauxprobe1, iprobe1), vz_phys(kauxprobe1, iprobe2), &
vz_phys(kauxprobe1, iprobe3),&
```

```
omg_phys(kauxprobe1, iprobe1), &
omg_phys(kauxprobe1, iprobe2), omg_phys(kauxprobe1, iprobe3)
call flush()
end if
end if
END IF
END IF
!Write out certain values for a restart case at outputfreq

IF ( (outputfreq /= 0) .AND. (MOD(itersnap,outputfreq) == 0) ) THEN
write(restart_filename, '(i10.10)') int(itersnap/outputfreq)
!allocates 10 digits with leading zeroes, edits from SH
call output_restart(FILE_STRING // "Restart", Ra, &
Pr, Ch, a, nn, nc, nz, nx, time, dt, nt, &
intt, itersnap, Nuvol_tavgsave, real(tem(:,:)), &
real(omg(:,:)), real(psi(:,:)), aimag(tem(:,:)), &
aimag(omg(:,:)), aimag(psi(:,:)), &
real(dtempdt(:,:,1)), real(domgdt(:,:,1)),&
aimag(dtempdt(:,:,1)), aimag(domgdt(:,:,1)),  &
kstart-1,kfinal+1,size,my_rank, nz_aux)
intt = int(time*outputfreq)
end if

!Step 6: Set the new time step
!(third dimension of dt arrays) to the previous time step
dtempdt(:,:,1) = dtempdt(:,:,2)
domgdt(:,:,1) = domgdt(:,:,2)
time = nt*dt !update time
ITER = ITER + 1
```

```
itersnap = itersnap + 1
end do


!End time loop!!!!!!!
```

Bibliography

Ashkenazy, Y. and Tziperman, E. (2016). Variability, instabilities, and eddies in a snowball ocean. *Journal of Climate*, 29(2):869–888.

Atkinson, D. H., Pollack, J. B., and Seiff, A. (1996). Galileo doppler measurements of the deep zonal winds at Jupiter. *Science*, 272(5263):842–843.

Aubert, J., Aurnou, J., and Wicht, J. (2008). The magnetic structure of convection-driven numerical dynamos. *Geophysical Journal International*, 172(3):945–956.

Aubert, J., Brito, D., Nataf, H. C., Cardin, P., and Masson, J. P. (2001). A Systematic experimental study of rapidly rotating spherical convection in water and liquid gallium. *Physics of the Earth and Planetary Interiors*, 128(1-4):51–74.

Aubert, J., Gastine, T., and Fournier, A. (2017). Spherical convective dynamos in the rapidly rotating asymptotic regime. *Journal of Fluid Mechanics*, 813:558–593.

Aubert, J., Gillet, N., and Cardin, P. (2003). Quasigeostrophic models of convection in rotating spherical shells. *Geochemistry, Geophysics, Geosystems*, 4(7).

Aurnou, J., Calkins, M., Cheng, J., Julien, K., King, E., Nieves, D., Soderlund, K., and Stellmach, S. (2015). Rotating convective turbulence in Earth and planetary cores. *Physics of the Earth and Planetary Interiors*, 246:52–71.

Aurnou, J. M., Andreadis, S., Zhu, L., and Olson, P. L. (2003). Experiments on convection in Earth's core tangent cylinder. *Earth and Planetary Science Letters*, 212(1):119–134.

Aurnou, J. M., Horn, S., and Julien, K. (2020). Connections between nonrotating, slowly rotating, and rapidly rotating turbulent convection transport scalings. *Phys. Rev. Research*, 2:043115.

Aurnou, J. M. and King, E. M. (2017). The cross-over to magnetostrophic convection in planetary dynamo systems. *Proceedings of the National Academy of Sciences*, 473(112):990–994.

Aurnou, J. M. and Olson, P. L. (2001). Experiments on Rayleigh–Bénard convection, magnetoconvection and rotating magnetoconvection in liquid gallium. *Journal of Fluid Mechanics*, 430:283–307.

Bloxham, J. and Gubbins, D. (1985). The secular variation of Earth's magnetic field. *Nature*, 317(31):771–781.

Burns, K. J., Vasil, G. M., Oishi, J. S., Lecoanet, D., and Brown, B. P. (2020). Dedalus: A flexible framework for numerical simulations with spectral methods. *Physical Review Research*, 2(2):023068.

Busse, F. H. (1970). Thermal instabilities in rapidly rotating systems. *Journal of Fluid Mechanics*, 44(3):441–460.

Busse, F. H. (1976). A simple model of convection in the Jovian atmosphere. *Icarus*, 29(2):255–260.

Busse, F. H. (1994). Convection driven zonal flows and vortices in the major planets. *Chaos*, 4(2):123–134.

Busse, F. H. (2002). Convective flows in rapidly rotating spheres and their dynamo action. *Physics of Fluids*, 14(4):1301–1314.

Busse, F. H. (2004). On thermal convection in slowly rotating systems. *Chaos: An Interdisciplinary Journal of Nonlinear Science*, 14(3):803–808.

Busse, F. H. and Carrigan, C. R. (1974). Convection induced by centrifugal buoyancy. *Journal of Fluid Mechanics*, 62(3):579–592.

Busse, F. H. and Hood, L. L. (1982). Differential Rotation Driven by Convection in a Rapidly Rotating Annulus. *Geophysical and Astrophysical Fluid Dynamics*, 21(1-2):59–74.

Busse, F. H. and Or, A. (1986). Convection in a rotating cylindrical annulus: thermal Rossby waves. *Journal of Fluid Mechanics*, 166:173–187.

Cabanes, S., Aurnou, J. M., Favier, B., and Le Bars, M. (2017). A laboratory model for deep-seated jets on the gas giants. *Nature Physics*, 13(4):387–390.

Cagney, N., Newsome, W. H., Lithgow-Bertelloni, C., Cotel, A., Hart, S. R., and Whitehead, J. A. (2015). Temperature and velocity measurements of a rising thermal plume. *Geochemistry, Geophysics, Geosystems*, 16(3):579–599.

Calkins, M. A., Aurnou, J. M., Eldredge, J. D., and Julien, K. (2012a). The influence of fluid properties on the morphology of core turbulence and the geomagnetic field. *Earth and Planetary Science Letters*, 359-360:55–60.

Calkins, M. A., Julien, K., Tobias, S. M., and Aurnou, J. M. (2015). A multiscale dynamo model driven by quasi-geostrophic convection. *Journal of Fluid Mechanics*, 780:143–166.

Calkins, M. A., Noir, J., Eldredge, J. D., and Aurnou, J. M. (2012b). The effects of boundary topography on convection in Earth's core. *Geophysical Journal International*, 189(2):799–814.

Cameron, R., Dikpati, M., and Brandenburg, A. (2017). The global solar dynamo. *Space Science Reviews*, 210(1):367–395.

Cao, H. and Stevenson, D. J. (2017). Zonal flow magnetic field interaction in the semi-conducting region of giant planets. *Icarus*.

Cardin, P. and Olson, P. (1994). Chaotic thermal convection in a rapidly rotating spherical shell: consequences for flow in the outer core. *Physics of the earth and planetary interiors*, 82(3-4):235–259.

Chakraborty, S. (2008). On scaling laws in turbulent magnetohydrodynamic Rayleigh–Benard convection. *Physica D: Nonlinear Phenomena*, 237(24):3233–3236.

Chan, C. J., Plumb, R. A., and Cerovecki, I. (2007). Annular modes in a multiple migrating zonal jet regime. *Journal of the atmospheric sciences*, 64(11):4053–4068.

Chandrasekhar, S. (1961). *Hydrodynamic and hydromagnetic stability.* Oxford University Press.

Chelton, D. B., DeSzoeke, R. A., Schlax, M. G., El Naggar, K., and Siwertz, N. (1998). Geographical variability of the first baroclinic rossby radius of deformation. *Journal of Physical Oceanography*, 28(3):433–460.

Chemke, R. and Kaspi, Y. (2015). Poleward migration of eddy-driven jets. *Journal of Advances in Modeling Earth Systems*, 7(3):1457–1471.

Cheng, J. S., Madonia, M., Aguirre Guzmán, A. J., and Kunnen, R. P. J. (2020). Laboratory exploration of heat transfer regimes in rapidly rotating turbulent convection. *Phys. Rev. Fluids*, 5:113501.

Cheng, J. S., Stellmach, S., Ribeiro, A., Grannan, A., King, E. M., and Aurnou, J. M. (2015). Laboratory-numerical models of rapidly rotating convection in planetary cores. *Geophysical Journal International*, 201(1):1–17.

Christensen, U., Olson, P., and Glatzmaier, G. A. (1999). Numerical modelling of the geodynamo: A systematic parameter study. *Geophysical Journal International*, 138(2):393–409.

Christensen, U. R. (2001). Zonal flow driven by deep convection in the major planets. *Geophysical Research Letters*, 28(13):2553–2556.

Christensen, U. R., Wicht, J., and Dietrich, W. (2020). Mechanisms for limiting the depth of zonal winds in the gas giant planets. *The Astrophysical Journal*, 890(1):61.

Cioni, S., Chaumat, S., and Sommeria, J. (2000). Effect of a vertical magnetic field on turbulent Rayleigh-Bénard convection. *Physical Review E*, 62(4):R4520.

Connerney, J. E. P., Kotsiaros, S., Oliversen, R. J., Espley, J. R., Joergensen, J. L., Joergensen, P. S., Merayo, J. M. G., Herceg, M., Bloxham, J., Moore, K. M., Bolton, S. J., and Levin, S. M. (2018). A new model of Jupiter's magnetic field from juno's first nine orbits. *Geophysical Research Letters*, 45(6):2590–2596.

Constantinou, N. C. and Parker, J. B. (2018). Magnetic suppression of zonal flows on a beta plane. *The Astrophysical Journal*, 863(1):46.

Cope, L. (2021). The dynamics of geophysical and astrophysical turbulence.

Cushman-Roisin, B. and Beckers, J.-M. (2011). *Introduction to geophysical fluid dynamics: physical and numerical aspects*. Academic press.

Danilov, S. D. and Gurarie, D. (2008). Quasi-two-dimensional turbulence. *Uspekhi Fizicheskih Nauk*, 170(9):921.

Davidson, P. (2001). *An Introduction to Magnetohydrodynamics*. Cambridge University Press, Cambridge.

Dietrich, W. and Jones, C. (2018). Anelastic spherical dynamos with radially variable electrical conductivity. *Icarus*, 305:15–32.

Dormy, E., Soward, A. M., Jones, C. A., Jault, D., and Cardin, P. (2004). The onset of thermal convection in rotating spherical shells. *Journal of Fluid Mechanics*, 501:43–70.

Duarte, L. D. V., Gastine, T., and Wicht, J. (2013). Anelastic dynamo models with variable electrical conductivity: An application to gas giants. *Physics of the Earth and Planetary Interiors*, 222:22–34.

Ecke, R. E. and Niemela, J. J. (2014). Heat transport in the geostrophic regime of rotating Rayleigh-Bénard convection. *Phys. Rev. Lett.*, 113:114301.

Favier, B., Silvers, L., and Proctor, M. (2014). Inverse cascade and symmetry breaking in rapidly rotating Boussinesq convection. *Physics of Fluids*, 26(9):096605.

Flannery, B. P., Teukolsky, S. A., Vetterling, W. T., Squyres, S. W., Reynolds, R. T., Cassen, P. M., Peale, S. J., Emery, J. P., Burr, D. M., Cruikshank, D. P., Brown, R. H., Dalton, J. B., Boone, S., Nicol, M. F., Crovisier, J., Mumma, M. J., Weaver, H. A., Festou, M. C., Keller, H. U., and Weaver, H. A. (2006). Cassini at enceladus. *Science*, 311(March):1422–1426.

French, M., Becker, A., Lorenzen, W., Nettelmann, N., Bethkenhagen, M., Wicht, J., and Redmer, R. (2012). Ab Initio Simulations for Material Properties Along the Jupiter Adiabat. *The Astrophysical Journal Supplement Series*, 202(1):5.

Friedlander, S. (1980). *An introduction to the mathematical theory of geophysical fluid dynamics*. Elsevier.

Galperin, B., Young, R. M., Sukoriansky, S., Dikovskaya, N., Read, P. L., Lancaster, A. J., and Armstrong, D. (2014). Cassini observations reveal a regime of zonostrophic macroturbulence on Jupiter. *Icarus*, 229:295–320.

Garaud, P., Gallet, B., and Bischoff, T. (2015). The stability of stratified spatially periodic shear flows at low péclet number. *Physics of Fluids*, 27(8):084104.

Gastine, T. (2019). pizza: an open-source pseudo-spectral code for spherical quasi-geostrophic convection. *Geophysical Journal International*, 217(3):1558–1576.

Gastine, T., Duarte, L. D. V., and Wicht, J. (2012). Dipolar versus multipolar dynamos: the influence of the background density stratification. *Astronomy & Astrophysics*, 546:A19.

Gastine, T. and Wicht, J. (2012). Effects of compressibility on driving zonal flow in gas giants. *Icarus*, 219(1):428 – 442.

Gastine, T. and Wicht, J. (2021). Stable stratification promotes multiple zonal jets in a turbulent Jovian dynamo model. *Icarus*, 368:114514.

Gillet, N., Brito, D., Jault, D., and Nataf, H. C. (2007). Experimental and numerical studies of convection in a rapidly rotating spherical shell. *Journal of Fluid Mechanics*, 580:83–121.

Gillet, N. and Jones, C. A. (2006). The quasi-geostrophic model for rapidly rotating spherical convection outside the tangent cylinder. *Journal of Fluid Mechanics*, 554:343–369.

Glatzmaier, G. (2014). *Introduction to Modeling Convection in Planets and Stars: Magnetic Field, Density Stratification, Rotation*. Princeton University Press.

Glatzmaier, G. A. (2008). A note on "Constraints on deep-seated zonal winds inside Jupiter and Saturn". *Icarus*, 196(2):665 – 666. Mars Polar Science IV.

Glatzmaier, G. A. and Olson, P. (1993). Highly supercritical thermal convection in a rotating spherical shell: centrifugal vs. radial gravity. *Geophysical & Astrophysical Fluid Dynamics*, 70(1-4):113–136.

Glatzmaier, G. A. and Roberts, P. H. (1995). A three-dimensional convective dynamo solution with rotating and finitely conducting inner core and mantle. *Physics of the Earth and Planetary Interiors*, 91(1):63–75. Study of the Earth's Deep Interior.

Goluskin, D., Johnston, H., Flierl, G. R., and Spiegel, E. A. (2014). Convectively driven shear and decreased heat flux. *Journal of Fluid Mechanics*, 759(6):360–385.

Gómez-Pérez, N., Heimpel, M., and Wicht, J. (2010). Effects of a radially varying electrical conductivity on 3D numerical dynamos. *Physics of the Earth and Planetary Interiors*, 181(1-2):42–53.

Greenspan, H. P. (1968). *The Theory of Rotating Fluids*. Cambridge University Press, London.

Greenspan, H. P. and Howard, L. N. (1963). On a time-dependent motion of a rotating fluid. *Journal of Fluid Mechanics*, 17(3):385–404.

Grossmann, S. and Lohse, D. (2000). Scaling in thermal convection: a unifying theory. *Journal of Fluid Mechanics*, 407:27–56.

Guervilly, C. and Cardin, P. (2016). Subcritical convection of liquid metals in a rotating sphere using a quasi-geostrophic model. *Journal of Fluid Mechanics*, 808:61–89.

Guervilly, C., Cardin, P., and Schaeffer, N. (2019). Turbulent convective length scale in planetary cores. *Nature*, 570:368–371.

Guervilly, C. and Hughes, D. W. (2017). Jets and large-scale vortices in rotating Rayleigh-Bénard convection. *Physical Review Fluids*, 2(11):1–21.

Hansen, U., Yuen, D. A., and Kroening, S. E. (1990). Transition to hard turbulence in thermal convection at infinite Prandtl number. *Physics of Fluids A: Fluid Dynamics*, 2(12):2157–2163.

Heimpel, M. and Aurnou, J. (2007). Turbulent convection in rapidly rotating spherical shells: A model for equatorial and high latitude jets on Jupiter and Saturn. *Icarus*, 187(2):540–557.

Heimpel, M., Aurnou, J., and Wicht, J. (2005). Simulation of equatorial and high-latitude jets on Jupiter in a deep convection model. *Nature*, 438(7065):193–196.

Heimpel, M. and Aurnou, J. M. (2012). Convective bursts and the coupling of Saturn's equatorial storms and interior rotation. *The Astrophysical Journal*, 746(1):51.

Heimpel, M. and Gómez Pérez, N. (2011). On the relationship between zonal jets and dynamo action in giant planets. *Geophysical Research Letters*, 38(14):2005–2010.

Horn, S. and Aurnou, J. M. (2018). Regimes of Coriolis-Centrifugal Convection. *Physical Review Letters*, 120(20):204502.

Horn, S., Shishkina, O., and Wagner, C. (2013). On non-Oberbeck–Boussinesq effects in three-dimensional Rayleigh-Bénard convection in glycerol. *Journal of Fluid Mechanics*, 724:175–202.

Ingersoll, A. P. (1990). Atmospheric dynamics of the outer planets. *Science*, 248(4953):308–315.

Jones, C. A. (2000). Convection–driven geodynamo models. *Philosophical Transactions of the Royal Society of London. Series A: Mathematical, Physical and Engineering Sciences*, 358(1768):873–897.

Jones, C. A. (2014). A dynamo model of Jupiter's magnetic field. *Icarus*, 241:148–159.

Jones, C. A. and Roberts, P. H. (2000). Convection-driven dynamos in a rotating plane layer. *Journal of Fluid Mechanics*, 404:311–343.

Julien, K. and Knobloch, E. (1998). Strongly nonlinear convection cells in a rapidly rotating fluid layer: the tilted f-plane. *Journal of Fluid Mechanics*, 360:141–178.

Julien, K., Knobloch, E., and Plumley, M. (2018a). Impact of domain anisotropy on the inverse cascade in geostrophic turbulent convection. *Journal of Fluid Mechanics*, 837:R41–R413.

Julien, K., Knobloch, E., and Plumley, M. (2018b). Impact of domain anisotropy on the inverse cascade in geostrophic turbulent convection. *Journal of Fluid Mechanics*, 837:R4.

Kaspi, Y., Galanti, E., Hubbard, W. B., Stevenson, D. J., Bolton, S. J., Iess, L., Guillot, T., Bloxham, J., Connerney, J. E. P., Cao, H., Durante, D., Folkner, W. M., Helled, R., Ingersoll, A. P., Levin, S. M., Lunine, J. I., Miguel, Y., Militzer, B., Parisi, M., and Wahl, S. M. (2018). Jupiter's atmospheric jet streams extend thousands of kilometres deep. *Nature*, 555:223.

Kaspi, Y., Galanti, E., Showman, A. P., Stevenson, D. J., Guillot, T., Iess, L., and Bolton, S. J. (2020). Comparison of the Deep Atmospheric Dynamics of Jupiter and Saturn in Light of the Juno and Cassini Gravity Measurements. *Space Science Reviews*, 216(5):84.

King, E. M. and Aurnou, J. M. (2015). Magnetostrophic balance as the optimal state for turbulent magnetoconvection. *Proceedings of the National Academy of Sciences*, 112(4):990–994.

King, E. M., Stellmach, S., Noir, J., Hansen, U., and Aurnou, J. M. (2009). Boundary layer control of rotating convection systems. *Nature*, 457(7227):301–304.

Kirk, R. L. and Stevenson, D. J. (1987). Hydromagnetic constraints on deep zonal flow in the giant planets. *Astrophysical Journal*, 316(1):836–846.

Kivelson, M. G., Khurana, K. K., Russell, C. T., Walker, R. J., Warnecke, J., Coroniti, F. V., Polanskey, C., Southwood, D. J., and Schubert, G. (1996). Discovery of Ganymede's magnetic field by the Galileo spacecraft. *Nature*, 384:537–541.

Knaepen, B., Kassinos, S., and Carati, D. (2004). Magnetohydrodynamic Turbulence at Moderate Magnetic Reynolds Number. *Journal of Fluid Mechanics*, 513:199–220.

Knaepen, B. and Moreau, R. (2008). Magnetohydrodynamic Turbulence at Low Magnetic Reynolds Number. *Annual Review of Fluid Mechanics*, 40:25–45.

Kong, D., Zhang, K., and Schubert, G. (2017). On the gravitational signature of zonal flows in Jupiter-like planets: An analytical solution and its numerical validation. *Physics of the Earth and Planetary Interiors*, 263:1–6.

Kong, D., Zhang, K., Schubert, G., and Anderson, J. D. (2018). Origin of Jupiter's cloud-level zonal winds remains a puzzle even after juno. *Proceedings of the National Academy of Sciences*, 115(34):8499–8504.

Kraichnan, R. H. (1967). Inertial ranges in two-dimensional turbulence. *Physics of Fluids*, 10(7):1417–1423.

Kunnen, R., Clercx, H., and Van Heijst, G. (2013). The structure of sidewall boundary layers in confined rotating Rayleigh–Bénard convection. *Journal of fluid mechanics*, 727:509–532.

Kunnen, R. P. J. (2021). The geostrophic regime of rapidly rotating turbulent convection. *Journal of Turbulence*, 22(4-5):267–296.

Lemasquerier, D., Favier, B., and Le Bars, M. (2021). Zonal jets at the laboratory scale: hysteresis and Rossby waves resonance. *Journal of Fluid Mechanics*, 910:A18.

Lister, J. R. and Buffett, B. A. (1995). The strength and efficiency of thermal and compositional convection in the geodynamo. *Physics of the Earth and Planetary Interiors*, 91(1-3):17–30.

Liu, J., Goldreich, P. M., and Stevenson, D. J. (2008). Constraints on deep-seated zonal winds inside Jupiter and Saturn. *Icarus*, 196(2):653 – 664. Mars Polar Science IV.

Liu, J., Schneider, T., and Kaspi, Y. (2013). Predictions of thermal and gravitational signals of Jupiter's deep zonal winds. *Icarus*, 224(1):114–125.

Madonia, M., Guzmán, A. J. A., Clercx, H. J., and Kunnen, R. P. (2021). Velocimetry in rapidly rotating convection: Spatial correlations, flow structures and length scales. *Europhysics Letters*, 135(5):54002.

Maffei, S., Calkins, M. A., Julien, K., and Marti, P. (2019). Magnetic quenching of the inverse cascade in rapidly rotating convective turbulence. *Phys. Rev. Fluids*, 4:041801.

Manga, M. and Weeraratne, D. (1999). Experimental study of non-Boussinesq Rayleigh–Bénard convection at high Rayleigh and Prandtl numbers. *Physics of Fluids*, 11(10):2969–2976.

Matthews, P. (1999). Asymptotic solutions for nonlinear magnetoconvection. *Journal of Fluid Mechanics*, 387:397–409.

Matulka, A. M., Zhang, Y., and Afanasyev, Y. D. (2016). Complex environmental β-plane turbulence: laboratory experiments with altimetric imaging velocimetry. *Nonlinear Processes in Geophysics*, 23(1):21–29.

Maximenko, N. A., Bang, B., and Sasaki, H. (2005). Observational evidence of alternating zonal jets in the world ocean. *Geophysical Research Letters*, 32(12):1–4.

McWilliams, J. C. (2006). *Fundamentals of Geophysical Fluid Dynamics*. Cambridge University Press, Cambridge.

Moore, K. M., Yadav, R. K., Kulowski, L., Cao, H., Bloxham, J., Connerney, J. E., Kotsiaros, S., Jørgensen, J. L., Merayo, J. M., Stevenson, D. J., Bolton, S. J., and Levin, S. M. (2018). A complex dynamo inferred from the hemispheric dichotomy of Jupiter's magnetic field. *Nature*, 561(7721):76–78.

Mound, J., Davies, C. J., Rost, S., and Aurnou, J. M. (2019). Regional stratification at the top of Earth's core due to core–mantle boundary heat flux variations. *Nature Geoscience*, page (accepted).

Nakagawa, Y. (1955). An experiment on the inhibition of thermal convection by a magnetic field. *Nature*, 175(4453):417–419.

Nieves, D., Rubio, A. M., and Julien, K. (2014). Statistical classification of flow morphology in rapidly rotating Rayleigh-Bénard convection. *Physics of Fluids*, 26(8):086602.

Nurser, A. and Bacon, S. (2014). The Rossby radius in the arctic ocean. *Ocean Science*, 10(6):967–975.

Orvedahl, R. J., Featherstone, N. A., and Calkins, M. A. (2021). Large-scale magnetic field saturation and the Elsasser number in rotating spherical dynamo models. *Monthly Notices of the Royal Astronomical Society: Letters*, 507(1):L67–L71.

Peyret, J. (2002). *Spectral Methods for Incompressible Viscous Flows.* Springer-Verlag New York Inc., New York.

Phillips, N. A. (1963). Geostrophic motion. *Reviews of Geophysics*, 1(2):123–176.

Pierrehumbert, R. (1984). Local and global baroclinic instability of zonally varying flow. *Journal of Atmospheric Sciences*, 41(14):2141–2162.

Porco, C. C., West, R. A., Mcewen, A., Genio, A. D., Andrew, P., Thomas, P.and Squyres, S., Dones, L.and Murray, C. D., Johnson, T. V., Burns, J. A., Brahic, A., Neukum, G., Veverka, J., Barbara, J. M., Evans, M., Ferrier, J. J., Geissler, P., Helfenstein, P., and Roatsch, T. (20003). Cassini Imaging of Jupiter's Atmosphere, Satellites and Rings. *Science*, 299(5612):1–14.

Pothérat, A. and Klein, R. (2017). Do magnetic fields enhance turbulence at low magnetic Reynolds number? *Physical Review Fluids*, 2(6):063702.

Pothérat, A., Sommeria, J., and Moreau, R. (2000). An effective two-dimensional model for MHD flows with transverse magnetic field. *Journal of Fluid Mechanics*, 424:75–100.

Pothérat, A. and Klein, R. (2014). Why, how and when mhd turbulence at low *Rm* becomes three-dimensional. *Journal of Fluid Mechanics*, 761:168–205.

Proctor, M. and Weiss, N. (1982). Magnetoconvection. *Reports on Progress in Physics*, 45(11):1317.

Rhines, P. B. (1975). Waves and turbulence on a beta-plane. *Journal of Fluid Mechanics*, 69(3):417–443.

Ridley, V. A. and Holme, R. (2016). Modeling the Jovian magnetic field and its secular variation using all available magnetic field observations. *Journal of Geophysical Research: Planets*, 121(3):309–337.

Riehl, H., Yeh, T., and La Seur, N. (1950). A study of variations of the general circulation. *Journal of Atmospheric Sciences*, 7(3):181–194.

Roberts, P. (2015). *Treatise on Geophysics, chapter Theory of the Geodynamo.* Elsevier,.

Roberts, P. H. (1967). *Introduction to Magnetohydrodynamics.* Longmans, Green and Co.

Salmon, R. (1980). Baroclinic instability and geostrophic turbulence. *Geophysical & Astrophysical Fluid Dynamics*, 15(1):167–211.

Schaeffer, N. and Cardin, P. (2005). Quasigeostrophic model of the instabilities of the Stewartson layer in flat and depth-varying containers. *Physics of Fluids*, 17(10).

Schneider, T. (2006). The General Circulation of the Atmosphere. *Annual Review of Earth and Planetary Sciences*, 34:655–688.

Schneider, T. and Liu, J. (2009). Formation of jets and equatorial superrotation on Jupiter. *Journal of the Atmospheric Sciences*, 66(3):579–601.

Schöttler, M. and Redmer, R. (2018). Ab initio calculation of the miscibility diagram for hydrogen-helium mixtures. *Phys. Rev. Lett.*, 120:115703.

Schumann, U. (1976). Numerical simulation of the transition from three-to two-dimensional turbulence under a uniform magnetic field. *Journal of fluid mechanics*, 74(1):31–58.

Scott, R. K. and Dritschel, D. G. (2012a). The structure of zonal jets in geostrophic turbulence. *Journal of Fluid Mechanics*, 711:576–598.

Scott, R. K. and Dritschel, D. G. (2012b). The structure of zonal jets in geostrophic turbulence. *Journal of Fluid Mechanics*, 711:576–598.

Sheyko, A., Finlay, C., Favre, J., and Jackson, A. (2018). Scale separated low viscosity dynamos and dissipation within the earth's core. *Scientific reports*, 8(1):1–7.

Shishkina, O., Emran, M. S., Grossmann, S., and Lohse, D. (2017). Scaling relations in large-Prandtl-number natural thermal convection. *Phys. Rev. Fluids*, 2:103502.

Showman, A. P., Gierasch, P. J., and Lian, Y. (2006). Deep zonal winds can result from shallow driving in a giant-planet atmosphere. *Icarus*, 182(2):513–526. Results from the Mars Express ASPERA-3 Investigation.

Showman, A. P., Kaspi, Y., and Flierl, G. R. (2011). Scaling laws for convection and jet speeds in the giant planets. *Icarus*, 211(2):1258–1273.

Simitev, R. and Busse, F. H. (2005). Prandtl-number dependence of convection-driven dynamos in rotating spherical fluid shells. *Journal of Fluid Mechanics*, 532:365–388.

Sinha, B. and Richards, K. (1999). Jet structure and scaling in Southern Ocean models. *Journal of Physical Oceanography*, 29(6):1143–1155.

Smith, C. A., Speer, K. G., and Griffiths, R. W. (2014). Multiple zonal jets in a differentially heated rotating annulus. *Journal of Physical Oceanography*, 44(9):2273–2291.

Soderlund, K. M., Heimpel, M. H., King, E. M., and Aurnou, J. M. (2013). Turbulent models of ice giant internal dynamics: Dynamos, heat transfer, and zonal flows. *Icarus*, 224(1):97–113.

Soderlund, K. M., King, E. M., and Aurnou, J. M. (2012). The influence of magnetic fields in planetary dynamo models. *Earth and Planetary Science Letters*, 333-334:9–20.

Soderlund, K. M., Sheyko, A., King, E. M., and Aurnou, J. M. (2015). The competition between Lorentz and Coriolis forces in planetary dynamos. *Progress in Earth and Planetary Science*, 2(1):1–10.

Sommeria, J. and Moreau, R. (1982). Why, how, and when, MHD turbulence becomes two-dimensional. *Journal of Fluid Mechanics*, 118:507–518.

Sreenivasan, B. and Alboussière, T. (2002). Experimental study of a vortex in a magnetic field. *Journal of Fluid Mechanics*, 464:287–309.

Sreenivasan, B. and Jones, C. A. (2005). Structure and dynamics of the polar vortex in the Earth's core. *Geophysical Research Letters*, 32(20).

Stanley, S. and Glatzmaier, G. A. (2010). Dynamo Models for Planets Other Than Earth. *Space Science Reviews*, 152(1):617–649.

Stellmach, S., Lischper, M., Julien, K., Vasil, G., Cheng, J. S., Ribeiro, A., King, E. M., and Aurnou, J. M. (2014). Approaching the asymptotic regime of rapidly rotating convection: Boundary layers versus interior dynamics. *Phys. Rev. Lett.*, 113:254501.

Stewartson, K. (1957). On almost rigid rotations. *Journal of Fluid Mechanics*, 3(1):17–26.

Stix, M. (1976). Differential rotation and the solar dynamo. *Astronomy and Astrophysics*, 47:243–254.

Terry, P. (2000). Suppression of turbulence and transport by sheared flow. *Reviews of Modern Physics*, 72(1):109.

Tobias, S. M., Dagon, K., and Marston, J. B. (2011). Astrophysical fluid dynamics via direct statistical simulation. *The Astrophysical Journal*, 727(2):127.

Tobias, S. M., Diamond, P. H., and Hughes, D. W. (2007). β-plane magnetohydrodynamic turbulence in the solar tachocline. *The Astrophysical Journal*, 667(1):L113–L116.

Tollefson, J., Wong, M. H., de Pater, I., Simon, A. A., Orton, G. S., Rogers, J. H., Atreya, S. K., Cosentino, R. G., Januszewski, W., Morales-Juberías, R., and Marcus, P. S. (2017). Changes in Jupiter's zonal wind profile preceding and during the juno mission. *Icarus*, 296:163–178.

Vallis, G. (2006). *Atmospheric and Oceanic Fluid Dynamics: Fundamentals and Large-Scale Circulation*. Cambridge University Press, London.

Vasavada, A. R. and Showman, A. P. (2005). Jovian atmospheric dynamics: an update after Galileo and Cassini. *Reports on Progress in Physics*, 68(8):1935–1996.

Vogt, T., Yang, J.-C., Schindler, F., and Eckert, S. (2021). Free-fall velocities and heat transport enhancement in liquid metal magneto-convection. *Journal of Fluid Mechanics*, 915.

Wagner, F. (2007). A quarter-century of h-mode studies. *Plasma Physics and Controlled Fusion*, 49(12B):B1.

Wang, Q., Chong, K. L., Stevens, R. J. A. M., Verzicco, R., and Lohse, D. (2020). From zonal flow to convection rolls in Rayleigh-Bénard convection with free-slip plates. *Journal of Fluid Mechanics*, 905:A21.

Warn-Varnas, A., Fowlis, W. W., Piacsek, S., and Lee, S. M. (1978). Numerical solutions and laser-doppler measurements of spin-up. *Journal of Fluid Mechanics*, 85(4):609–639.

Weiss, N. O. and Proctor, M. (2014). *Magnetoconvection*. Cambridge University Press.

Wesson, J. (2011). *Tokamaks*. Oxford University Press.

Wicht, J. (2002). Inner-core conductivity in numerical dynamo simulations. *Physics of the Earth and Planetary Interiors*, 132(4):281–302.

Williams, G. (2003). Jovian dynamics. part iii: Multiple, migrating, and equatorial jets. *Journal of the atmospheric sciences*, 60(10):1270–1296.

Xu, Y., Horn, S., and Aurnou, J. M. (2022). Thermoelectric precession in turbulent magnetoconvection. *Journal of Fluid Mechanics*, 930.

Yadav, R. K., Gastine, T., Christensen, U. R., Wolk, S. J., and Poppenhaeger, K. (2016). Approaching a realistic force balance in geodynamo simulations. *Proceedings of the National Academy of Sciences*, 113(43):12065–12070.

Yan, M., Calkins, M. A., Maffei, S., Julien, K., Tobias, S. M., and Marti, P. (2019). Heat transfer and flow regimes in quasi-static magnetoconvection with a vertical magnetic field. *Journal of Fluid Mechanics*, 877:1186–1206.

Young, R. M., Read, P. L., and Wang, Y. (2019). Simulating Jupiter's weather layer. part i: Jet spin-up in a dry atmosphere. *Icarus*, 326:225–252.

Yu, Z., Leinweber, H., and Russell, C. (2010). Galileo constraints on the secular variation of the Jovian magnetic field. *Journal of Geophysical Research: Planets*, 115(E3).

Zhang, K., Kong, D., and Schubert, G. (2015). Thermal-gravitational wind equation for the wind-induced gravitational signature of giant gaseous planets: Mathematical derivation, numerical method, and illustrative solutions. *Astrophysical Journal*, 806(2).

Zhang, K. and Schubert, G. (2000). Magnetohydrodynamics in rapidly rotating spherical systems. *Annual review of fluid mechanics*, 32(1):409–443.

Zikanov, O., Belyaev, I., Listratov, Y., Frick, P., Razuvanov, N., and Sviridov, V. (2021). Mixed Convection in Pipe and Duct Flows With Strong Magnetic Fields. *Applied Mechanics Reviews*, 73(1).

Zürner, T. (2020). Refined mean field model of heat and momentum transfer in magnetoconvection. *Physics of Fluids*, 32(10):107101.

Zürner, T., Liu, W., Krasnov, D., and Schumacher, J. (2016). Heat and momentum transfer for magnetoconvection in a vertical external magnetic field. *Phys. Rev. E*, 94:043108.